



HAL
open science

High performance, low cost and low consumption Radio over fiber Systems for diversified communications applications.

Jacopo Nanni

► **To cite this version:**

Jacopo Nanni. High performance, low cost and low consumption Radio over fiber Systems for diversified communications applications.. Optics [physics.optics]. Université Paris-Est; Università degli studi (Bologne, Italie), 2018. English. NNT : 2018PESC1162 . tel-02366138

HAL Id: tel-02366138

<https://theses.hal.science/tel-02366138>

Submitted on 15 Nov 2019

HAL is a multi-disciplinary open access archive for the deposit and dissemination of scientific research documents, whether they are published or not. The documents may come from teaching and research institutions in France or abroad, or from public or private research centers.

L'archive ouverte pluridisciplinaire **HAL**, est destinée au dépôt et à la diffusion de documents scientifiques de niveau recherche, publiés ou non, émanant des établissements d'enseignement et de recherche français ou étrangers, des laboratoires publics ou privés.



École Doctorale MSTIC
Mathématiques, Sciences et Technologies de l' Information et de la Communication

Ph.D. Thesis

In order to obtain the title of Doctor of Science
Specialty: Electronics, optoelectronics and systems

Defended by
Jacopo Nanni

High Performance, Low Cost and Low Consumption Radio-over-Fiber Systems for Diversified Communications Applications

Supervised by

Prof. Catherine Algani, Prof. Giovanni Tartarini and Prof. Jean-Luc Polleux.

Prepared at ESIEE, ESYCOM Laboratory

and at Optics laboratory of the Department of Electrical, Electronic and Information Engineering
“Guglielmo Marconi” at University of Bologna (Italy)

Defended on December 14th 2018 in Bologna (Italy)

Jury

Reviewers:	Prof. Pierluigi DeBernardi	CNR, IEIIT di Torino (Italy)
	Prof. Marco Romanelli	Université de Rennes (France)
Advisors:	Prof. Catherine Algani	ESYCOM - Université Paris-Est (France)
	Prof. Giovanni Tartarini	Università di Bologna (Italy)
	Prof. Jean-Luc Polleux	ESYCOM - Université Paris-Est (France)
Examinators:	Prof. Pierpaolo Boffi	Politecnico di Milano (Italy)
	Prof. Gaetano Bellanca	Università di Ferrara (Italy)
	Prof. Jean-Marc Lauherte	Université Paris-Est (France)

Copyright © 2018 by Jacopo Nanni

All rights reserved. No part of this publication may be reproduced, stored in a retrieval system, or transmitted in any form or by any means without the prior written consent of the author.

Typeset using L^AT_EX.

Acknowledgments

My acknowledgement goes to the people which have contributed both directly and indirectly to this work.

First of all, I would like to thank Prof. Giovanni Tartarini, Prof. Catherine Algani and Prof. Jean-Luc Polleux which gave me the opportunity of pursuing the “cotutelle” Ph.D. program. Thank you for the helpful and stimulating discussions, and for teaching me everyday how to be a better researcher.

Then I would like to thank Dr. Pierluigi Debernardi and Prof. Marco Romanelli for accepting to be reviewers of this manuscript helping me with important comments and suggestions to improve the quality of the contents. My sincere gratitude also to Prof. Jean-Marc Laheurte, Prof. Pierpaolo Boffi and Prof. Gaetano Bellanca whom accepted to be examiners of this work.

A special thank goes then to my colleagues, mates and friends in Bologna and Paris, with whom I had always interesting discussions and talks.

Last but not least, I would like to thank the people which contribute indirectly to this work: my family and friends, which always helped me in difficult moments supporting and encouraging me.

Abstract

This dissertation aims to analyze the possibility of improving in terms of cost and consumption the future Radio-over-Fiber (RoF) systems in different telecommunication scenarios, such as current and next generation of cellular networks and in other applications such as Radio Astronomy. The RoF system studied is hence composed of a Vertical Cavity Surface Emitting Laser (VCSEL) operating at 850 nm, standard single mode fiber (SSMF) and SiGe Heterojunction Phototransistor (HPT), adopting the technique called Intensity Modulation–Direct Detection which is nowadays the cheapest and simplest architecture for RoF. This dissertation describes in detail the multimode propagation within the SSMF (designed to have single mode behavior only at 1310 nm and 1550 nm) which is present at 850 nm. Through a developed mathematical model, the two-modes propagation is described and the main phenomena involved are analyzed. In particular, the model focus on intermodal dispersion and modal noise which are considered the two main contributions of performance detrimental. The model developed is able to identify the main parameters which contribute to enhance the detrimental effects produced by intermodal dispersion and modal noise both in frequency and time domain. Starting from the model, possible techniques to improve the performances are then proposed. In particular, a pre-filtering technique is realized in order to avoid the excitation of the second order mode, allowing a quasi-single-mode propagation within the SSMF. The technique is theoretically and experimentally validated both for single radio frequency sinusoidal transmission and for bandpass signal transmission centered in radio frequency band. In particular it is demonstrated experimentally the possibility of increasing the modulation bandwidth of the RoF system, reducing at the same time the fluctuations of power and gain. Furthermore, the technique is validated in a real LTE transmission system, making the RoF technology proposed able to transmit 256-QAM LTE signal of 20 MHz bandwidth, confirming the possibility of using this technology to decrease the overall cost and consumption of the network. Further work has been done on the mathematical model. In particular the two modes propagation is exploited in order to characterize the chirp parameter of the VCSEL employed. Finally, the problem of coupling between fiber and opto-electronic devices is also discussed and investigated, in order to improve the efficiency while keeping low the cost. The possibility of utilizing a collective and passive polymer-based structure for coupling the optical fiber with small area photodetectors and VCSEL is presented, showing important improvements on coupling efficiency and tolerance to misalignment.

Keywords: Optical communications, Radio-over-Fiber, VCSEL, HPT, G.652 Fiber.

Resumé

Cette thèse vise à analyser en détails la possibilité d'améliorer les futurs systèmes Radio-sur-Fibre (RoF) dans différents scénarios de télécommunication, tels que les réseaux cellulaires actuels et de la prochaine génération, ainsi que dans d'autres applications telles que la radioastronomie. Le système RoF étudié est donc composé d'un laser à cavité verticale (VCSEL) fonctionnant à 850 nm, d'une fibre standard monomode (SSMF) et d'un phototransistor à hétérojonction SiGe (HPT), adoptant la technique appelée détection directe par modulation d'intensité qui est aujourd'hui l'architecture à moindre coût et la plus simple pour la RoF. Cette thèse décrit en détail la propagation non naturelle dans le SSMF (conçue pour fonctionner uniquement à 1310 nm et 1550 nm) à 850 nm. A travers un modèle mathématique développé, la propagation à deux modes est décrite et les principaux phénomènes impliqués sont analysés. En particulier, le modèle se concentre sur la dispersion intermodale et le bruit modal, considérés comme les deux principales contributions de performance nuisible. Le modèle mis au point permet d'identifier les principaux paramètres qui contribuent à renforcer les effets néfastes de la dispersion intermodale et du bruit modal, à la fois en fréquence et dans le temps. A partir du modèle, des techniques possibles pour améliorer les performances sont alors proposées. En fait, une technique de pré-filtrage est réalisée afin d'éviter l'excitation du mode du second ordre, permettant une propagation quasi-monomode au sein du SSMF. La technique est validée théoriquement et expérimentalement soit pour une transmission sinusoïdale à radiofréquence unique, soit pour une transmission de signal passe-bande centrée sur une bande de radiofréquence. Il est démontré expérimentalement la possibilité d'augmenter la bande passante de modulation du système RoF, tout en réduisant les fluctuations de puissance et de gain. De plus, la technique est validée dans un véritable système de transmission LTE, ce qui permet à la technologie RoF de transmettre un signal LTE 256-QAM de 20 MHz, confirmant la possibilité d'utiliser cette technologie pour réduire le coût global et la consommation du réseau. Des travaux supplémentaires ont été réalisés sur le modèle mathématique. En fait, la propagation des deux modes est exploitée en sens inverse pour caractériser le chirp du VCSEL utilisé. Enfin, le problème du couplage entre les fibres et les dispositifs optoélectroniques est discuté et étudié afin de améliorer les performances tout en gardant un faible coût. La possibilité d'utiliser une structure collective et passive pour coupler la fibre optique avec des photodétecteurs à petite surface et VCSEL est présentée, montrant des améliorations importantes sur l'efficacité du couplage et la tolérance au désalignement.

Mot clé: communication optique, Radio-sur-Fibre, VCSEL, HPT, fibre G.652.

Contents

Acknowledgments	i
Abstract	iii
Resumé	v
Contents	vi
List of acronyms	ix
Introduction	1
1 Description of the RoF technology and components utilized	5
1.1 RoF architectures	5
1.2 RoF applications	11
1.3 Low cost optical components	15
1.3.1 Silica-based optical fiber	15
1.3.2 Short wavelength VCSEL technology	23
1.3.3 SiGe HPT technology	29
1.4 Summary and Discussion	34
2 850nm propagation in standard G.652 fiber	35
2.1 Direct modulation of a semiconductor laser	35
2.2 Electrical field propagation	38
2.3 Investigation of possible solutions to mitigate modal noise and intermodal dispersion	48
2.4 Exploitation of modal noise for the computation of the frequency chirp factor of 850 nm VCSEL	56
2.5 Interferometry-Based (IB) technique for measuring the chirp factor of DFB lasers	67
2.6 Summary and Discussion	76

3	VCSEL-SSMF-based IM-DD A-RoF for LTE applications	77
3.1	Performance evaluation of VCSEL-SSMF IM-DD A-RoF system for LTE applications	77
3.2	Performance of the A-RoF system adopting the pre-filtering technique	84
3.3	Use of SiGe HPT in VCSEL-SSMF-based RoF link	90
3.4	Summary and Discussion	106
4	Experimental study of polymer structure for collective and passive optical coupling	107
4.1	State of the art and description of the passive coupling structure	107
4.2	Case at 1550 nm SSMF-to-PD	110
4.3	Case at 850 nm SSMF-to-PD	113
4.4	VCSEL-to-fiber case	116
4.5	Summary and Discussion	119
	Conclusions	121
	References	125
	List of publications	137

List of acronyms

- 3G** Third Generation
- 4G** Fourth Generation
- 5G** Fifth Generation
- ADC** Analog-to-Digital Converter
- APD** Avalanche Photo-Detector
- A-RoF** Analog Radio over Fiber
- ASKAP** Australian Square Kilometer Array Pathfinder
- B2B** Back-to-Back
- BBU** BaseBand Unit
- BW** bandwidth
- CPRI** Common Public Radio Interface
- DAC** digital-to-analog converter
- DAS** Distributed Antenna System
- DBR** Distributed Bragg Reflectors
- DC** Direct Current
- DFB** Distributed Feed-Back
- DFT** Discrete Fourier Transform
- D-RoF** Digital Radio over Fiber
- DSF** Dispersion-Shifted Fiber
- DU** Digital Unit

EAM Electro-Absorption Modulator

EEL Edge Emitting Laser

EVM Error Vector Magnitude

FDD Frequency Division Duplexing

FH Front-Haul

FP Fabry-Perot

FSL Free-Space Loss

FTTH Fiber-To-The-Home

FWHM Full Width Half Maximum

GI Graded-Index

GOF Glass Optical Fiber

HAN Home Area Network

HBT Hetero-junction Bipolar Transistor

HPT Hetero-junction bipolar Photo-Transistor

IF Intermediate Frequency

IM-DD Intensity Modulation – Direct Detection

ISM Industrial, Scientific and Medical

IVD Inside Vapour Deposition

LAN Local Area Network

LED Light Emitting Diode

LNA Low Noise Amplifier

LoS Line of Sight

LTE Long Term Evolution

MBE Molecular Beam Epitaxy

MFH Mobile Front-Haul

MMF Multi-Mode Fiber

MOCVD Metal-Organic Chemical Vapor Deposition

MQWs Multi-Quantum Wells

MTM Multi-Transverse-Mode

MZM Mach-Zehnder Modulator

NA Numerical Aperture

NFV Network Function Virtualization

NSD Noise Spectral Density

OBSAI Open Base Station Architecture Initiative

OFL OverFilled Launch

OMI Optical Modulation Index

OVD Outside Vapour Deposition

PAF Planar Array Feed

PAPR Peak-to-Average Power Ratio

PD Photo-Diode

PDSCH Physical Downlink Shared CHannel

PIN P-doped-Intrinsic-N-doped

PMMA Poly(methyl methacrylate)

POF Plastic Optical Fiber

QAM Quadrature Amplitude Modulation

QPSK quadrature phase shift keying

QW Quantum Well

RAN Radio Access Network

RAP Radio Access Point

RAU Remote Access/Antenna Unit

RCFM Rigorously Computed Fiber Modes

RD Radio Dot

RF Radio Frequency

RIN Relative Intensity Noise

RoF	Radio over Fiber
RRH	Remote Radio Head
RRU	Remote Radio Unit
RTD	Resistor Temperature Detector
SDN	Software Defined Network
SEM	Scanning Electron Microscopic
SKA	Square Kilometer Array
SM	Single-Mode
SMF	Single-Mode Fiber
SNOM	Scanning Near-field Optical Mapping
SNR	Signal-to-Noise Ratio
SSMF	Standard Single-Mode Fiber
SWDM	Shortwave Wavelength Division Multiplexing
UV	Ultraviolet
VAD	Vapour Axial Deposition
VCSEL	Vertical Cavity Surface Emitting Laser
VLBI	Very Long Baseline Interferometry
VDS	Vapour Deposited Silica
VDN	Very Dense Network
VGC	Vertical Grating Coupler
VNA	Vector Network Analyzer
VSA	Vector Signal Analyzer
VSG	Vector Signal Generator
WAN	Wide Area Network
WLAN	Wireless Local Area Network
WiFi	Wireless Fidelity
WDM	Wavelength Division Multiplexing

Introduction

Context of the work

Since the last few years, wireless communications and services have increasingly taken part to people's lives day after day. The continuous society demand of having multi-tasking system platforms in which everyone can be connected and exchange information in any place and any time has increased exponentially and it is far to be stopped. The advent of social network platforms, big data cloud storage, high quality 4k video and in general broadband data communications, led the operators make a big effort in evolving more and more the infrastructures.

In particular, to provide access to the highest number of users with the maximum possible data-rate the biggest effort must be done in the access part of the network, increasing its capacity.

In mobile networks of third (3G), fourth (4G) generation, the access infrastructure (also known as Front-Haul (FH)) is mostly composed of many wireless transceivers (Radio Access Points (RAPs)), which send/receive the signal to/from the user devices (tablet, TV, smartphone, PC, etc...) connected each other with transmission cables which connect the transceiver with a central unit which control and handle the communications at higher level.

The transmission cable typically used is the optical fiber adopting the technology called Radio over Fiber (RoF). The advantages of optical fiber cables include high capacity for short and long distances, low attenuation, interference immunity and low fabrication cost due to its material composition (polymer or SiO_2).

The fiber typology typically employed nowadays is the SiO_2 Standard Single-Mode Fiber (SSMF) which, thanks to its single mode behavior, guarantees the highest possible channel capacity. For this reason it is considered more future-proof than the other fiber typology and the limitations in terms of noise and bandwidth are mostly given by electro-optical and opto-electrical devices.

The scenarios which include this type of access architectures are many and not only related to mobile networks. In fact, the fiber optic based infrastructure can be used in Wireless Local Area Network (WLAN) or in Home Area Network (HAN) to distribute the broadband internet connection through new generations of Wireless Fidelity (WiFi) standard in houses and offices.

Within all those scenarios, cost and consumption are considered as key points for the design and implementation because of the higher density of RAPs to be installed and the higher spreading of the network which is necessary to increase the overall network capacity.

Therefore the objective of my Ph.D. work consisted in investigating the possibility of improving the Radio over Fiber systems based on Standard Single-Mode Fiber exploiting the integration of low cost devices such as Vertical Cavity Surface Emitting Laser (VCSEL) and SiGe microwave phototransistor.

The target applications are the aforementioned access networks of WLANs, HANs and the FH of 4G and future fifth (5G) generation of telecommunication networks.

Moreover another application of interest regards radio astronomic plants which nowadays take advantages of interference immunity and low attenuation to transport the signal received from the antenna to the processing room or to feed antenna arrays. In particular the possible down-link of Very Long Baseline Interferometry (VLBI) parabola antennas and in general the distribution of the received radio signals in radio-astronomic plants is considered as possible application.

Main contributions

The main contributions of my Ph.D. work are listed hereafter:

- Study of the feasibility of low cost and low consumption SSMF-based RoF link using 850 nm VCSEL as optical source.
 - Study of the behavior of SSMF under 850 nm propagating wavelength and of compensation techniques to face the major problems [P.4, P.10].
 - Demonstration of possible 256-QAM LTE transmission RoF link based on VCSEL and SSMF [P.2, P.7].
- Investigation on the possible use of SiGe Hetero-junction bipolar Photo-Transistor (HPT) as photo-receiver for SSMF-based RoF links.
 - Characterization of the HPT properties in case of light injected by the SSMF.
 - Demonstration of possible LTE transmission of RoF link based on Single-Mode (SM) VCSEL, SSMF and SiGe HPT [P.6].
- Analysis of the improvement through a novel 3D thin film polymer optical coupling layer on fiber-to-PD and VCSEL-to-fiber.
 - Evaluation of the impact of fiber-to-PD coupling structure, realized by ICON photonics[®], on small area photodetector coupled with SSMF at 1550 nm [P.5].
 - Evaluation of the impact fiber-to-PD ICON photonics[®] coupling structure on power fluctuations related to modal noise in RoF links based on 850 nm VCSEL and SSMF.

- Experimental characterization of 850 nm VCSEL-to-fiber ICON photonics[®] coupling structure to couple VCSEL and multi-mode fiber.
- Exploitation of multimode side effects in SSMF operating at 850 nm for measuring the chirp parameters of semiconductor devices.
 - Exploitation of intermodal dispersion and modal noise in SSMF for measuring chirp parameters of an 850 nm source [P.1].
 - Extension of the method to a Distributed Feed-Back (DFB) source through an interferometry-based method [P.3].

Dissertation Outline

The thesis dissertation is organized in 4 chapters.

Chapter 1 gives an overview on Radio over Fiber (RoF) technology for current and next generation of telecommunication networks and other scenarios such as the Radio Astronomy, reporting the technology basic principles and state of the art. Then, current design challenges, such as costs and consumption reduction, are briefly discussed and many techniques are presented and compared.

The focus will be then on the employment of low cost devices such as 850 nm VCSEL and SiGe HPT in SSMF-based RoF with Intensity Modulation – Direct Detection (IM-DD) transmission technique, which represents to the main part of my Ph.D. work. A detailed description of those two technologies will be given, in order to better understand advantages and disadvantages in using such technologies, comparing each of them with possible contenders.

Chapter 2 gives a detailed mathematical model which describes analytically the propagation at 850 nm within SSMF representing the case of VCSEL excitation. The problematic and issues of this type of link will be pointed out and a solution to mitigate them will be theoretically and experimentally presented.

Furthermore, it will be shown that the multimode side effects of such propagation can be usefully exploited for the possible characterization of intrinsic parameters of the laser source.

Chapter 3 focuses on the application-oriented experimental work. The performances of the employed devices and the links considered will be shown and theoretical aspects highlighted in previous chapter will be further validated.

The transmission of Long Term Evolution (LTE) frames has been utilized for the evaluation of the performances of the overall low cost RoF link.

The Chapter is also dedicated to the characterization of VCSELs and SiGe HPT in order to relate the performance obtained with the characteristics of the devices.

Chapter 4 is dedicated to a specific challenge typically present in fiber optic link for telecom-

munications. This challenge regards the optical coupling between optical devices and optical fiber. In particular, this chapter analyzes the VCSEL-to-fiber and fiber-to-Photo-Diode (PD) coupling. Indeed, the coupling efficiency in these two situations has an important impact on the link performances. It is then necessary to study this problem in order to be able to improve the design. In particular, structures realized by ICON Photonics[®] technologies are tested and simulated in order to show their benefit.

Finally, the achieved results are summarized in the **Conclusions** section introducing possible future perspectives of my work.

The work presented in this thesis is the outcome of the joint (co-tutelle) Ph.D. research activity performed at the “Dipartimento di Ingegneria dell’Energia Elettrica e dell’Informazione *Guglielmo Marconi*” (DEI) of the University of Bologna, Italy and the “Electronique, SYstèmes de COmmunications et Microsystemes” (ESYCOM) laboratory of “École Supérieure d’Ingénieurs en Électrotechnique et Électronique” (ESIEE) Paris, Université Paris-Est (UPE) located at Noisy-le-Grand (Paris), France.

Description of the RoF technology and components utilized

In this chapter the technology known as RoF is introduced in his main technical aspects. Then, the most recent issues and requirements by telecommunication applications are presented explaining the state of the art of the possible techniques to increase the performances. Successively, the two main potentially low cost technologies for optical transmission and reception which have been studied are presented. In detail:

Section 1.1 focuses on the fundamentals of RoF, explaining different type of techniques that can be implemented for the realization of the desired system.

Section 1.2 describes the possible applications in which RoF technology can be utilized showing the requirements of each application while presenting the versatility of such type of technology.

Section 1.3 introduces the technologies studied in this work with the aim of exploiting their advantages in RoF systems to decrease cost and consumption. In particular the components considered are the SSMF as optical medium, VCSEL as optical transmitter and SiGe HPT as optical receiver.

Finally in Section 1.4 discussion and summary of the Chapter are given.

1.1 RoF architectures

Analog Radio-over-Fiber with Intensity Modulation and Direct Detection

The main objective of RoF consists in transporting a generic passband signal, having finite bandwidth and centered on the Radio Frequency (RF) carrier, through an optical fiber, connecting in this way two or more points of a generic network. The basic and most simple technique to realize this link is represented schematically in Figure 1.1. The input passband RF electrical signal is up-converted to the optical domain through an electro-optic converter (e.g. Light Emitting Diode (LED) or Laser), then the optical signal generated, which contains the desired information, propagates within an optical fiber for a certain length. Once arrived at

destination, the optical signal is down-converted to the electrical domain by an opto-electronic device (e.g. P-doped-Intrinsic-N-doped (PIN) PD) giving back the desired bandpass signal.

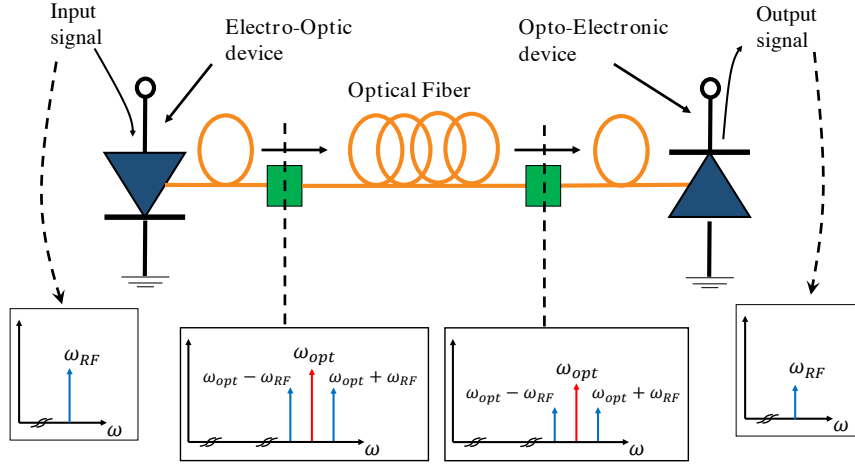


Figure 1.1: Typical RoF link schematic. The frequency spectrum at different stage of the optical link is also presented considering as input signal the generic carrier at ω_{RF} .

The simple link just explained is called in literature Intensity Modulation – Direct Detection (IM-DD) Analog Radio over Fiber (A-RoF). In particular, the intensity of optical power produced by the laser is directly modulated by the useful RF signal, while the output RF current of the photo-detector is produced by the optical power which is directly absorbed by the PD. Moreover, the transmission is performed in the analog domain, or rather, without the usage of any Analog-to-Digital Converter (ADC) to convert the RF signal in the digital domain.

The optical power emitted $P_{out,IM-DD}$ by the laser in such condition is expressed as follows

$$P_{out,IM-DD}(t) = P_{opt,0}(1 + x(t)) \quad (1.1)$$

in which $P_{opt,0}$ is a fixed value of optical power emitted at the optical frequency resulting by the bias current of the laser, while $x(t)$ is the normalized signal. Since it requires only the basic components of any opto-electronic system, IM-DD A-RoF is considered as the most basic architecture of transmission and therefore has the advantages to be low cost and simple to deploy.

However, some drawbacks are present. In fact, modulating directly the laser can lead to undesired phenomena such as high Relative Intensity Noise (RIN) value, limitation of the 3dB modulation response, broadening of the frequency spectrum and presence of spurious frequency modulations (frequency chirping) [1]. All these effects are physically produced by changes of the active region properties in presence of direct modulation of the carriers, which contribute to limit the performances of the laser.

Therefore, in order to increase the capacity of RoF systems, more sophisticated and complex techniques have been developed with the main objective of overcoming the problems related to direct modulation in IM-DD A-RoF architecture shown in Figure 1.1.

Externally modulated RoF

An effective way to overcome the problems related to IM-DD A-RoF architecture is to use an external opto-electronic modulator. The external modulation indeed, allows to bypass completely the direct modulation of the laser, with the idea of modulating the light after its generation (right after the laser).

Two main types of modulator currently exist: Electro-Absorption Modulator (EAM) and Mach-Zehnder Modulator (MZM). The first one is based on the Franz-Keldysh effect [2], which is the property of a material of changing the absorption coefficient if an external electrical field is applied. The second one, instead, is based on the properties of a material of changing its refractive index in presence of an electrical field producing the so called electro-optic effect also known as Pockels effect.

The schematic representation is shown in Figure 1.2 in which the case of MZM is considered. The RF input signal is injected directly in the MZM which modulates the light coming inside the device from a laser source, which is used in this case only as pure optical oscillator operating in continuous wave. The modulator itself is based on an interferometric scheme in which the light in one branch is subjected to the electro-optic effect which contributes to change the refractive index of the light passing through it, changing its phase. In such way, when the light paths of the two branches are recombined, the amplitude of the resulting interference depends on the phase difference of the two branches of the interferometer.

This architecture can be therefore exploited to modulate both amplitude [3] and phase [4] of the optical signal exploiting in this last case a balanced MZM modulator.

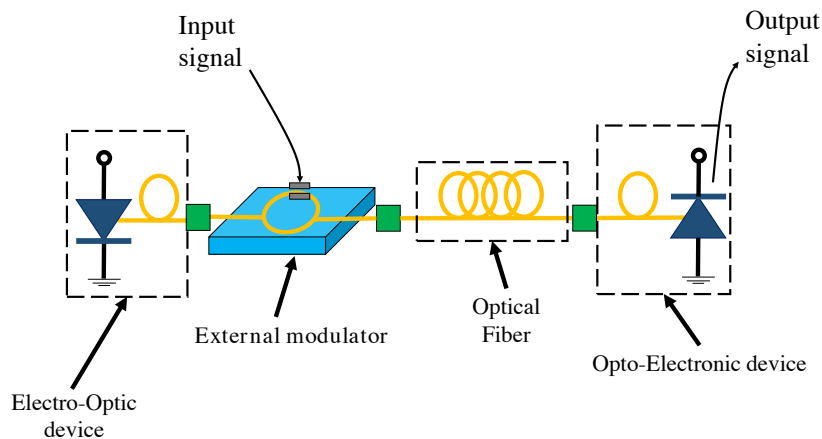


Figure 1.2: Typical schematic of an externally modulated RoF link.

The expression of the optical power which comes out from the modulator can be written as [5]:

$$P_{opt,mod}(t) = P_{opt,0} \cos^2 \left(\pi \frac{V(t)}{2V_{\pi}} \right) \quad (1.2)$$

in which $P_{opt,0}$ is the optical power emitted by the laser, $V(t) = V_0 + v(t)$ is the voltage applied to the modulator which is composed of a biasing point V_0 and the desired signal $v(t)$. Finally V_π is the voltage necessary to reach the phase of π . This last parameter contains the intrinsic quantities which are responsible for the electro-optic effect.

This architecture is generally present in long-haul RoF, in order to avoid the problems related to the non-linearities produced by, for example, the presence of frequency chirping and chromatic dispersion in SSMF-based A-RoF operating at 1550 nm [6]. However, since the cost of this device is not negligible, the range of possible applications is restricted, despite the higher performances reached [5].

Coherent RoF

In the previous section, it has been shown that employing an external optical modulator, the problems related to the direct modulation of the laser can be solved. However, a system limitation in terms of possible modulation schemes to be used is still given by the direct detection of the PD. With this technique only the amplitude can be detected so that no phase or frequency modulations scheme can be exploited. To have the possibility of having information of phase and frequency the detection should in fact be coherent. The principle is the same as homodyne or heterodyne detection, in which the arriving signal is beaten with a known optical carrier (local oscillator). The main scheme of a coherent receiver is shown in Figure 1.3.

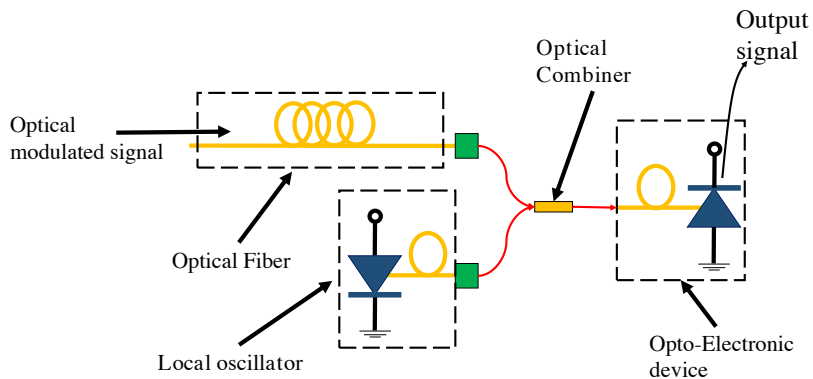


Figure 1.3: Typical Coherent detection RoF link schematic.

This technique exploits the presence of a local oscillator in the receiver side which has the properties of wavelength tuning and low spectral linewidth. In this way the modulated signal with a phase ϕ_u is beaten with the local oscillator having a phase ϕ_w producing two electrical field components having phases $\phi_w + \phi_u$ and $\phi_w - \phi_u$. Therefore, choosing accurately the frequency of the tunable laser, the resulting useful signal can be located in any Intermediate Frequency (IF) of the spectrum or in baseband and phase and frequency can be used as

signal carriers. Moreover, the coherent detection improves the sensitivity compared to direct detection, leading to the extension of transmission reach in a long-haul transmission system. This fact was actually the first main advantage for which this technique became popular [7,8].

Digital RoF

Up to this point, all the possible architectures shown regard the transmission of analog signals with the RoF link. However, a considerable improvement of the performances is obtained when the transmission is realized in digital domain, hence with a Digital Radio over Fiber (D-RoF) system. The main architecture is shown in Figure 1.4. The technique consists in sampling the RF signal through an ADC and sending the samples directly to the laser. Then, after the transmission through the optical fiber and the reception by the PD, the signal is converted again to the analog domain and re-transmitted or simply sent it directly to a central processing unit. Indeed, D-RoF aims to bring the benefits of digital optical link to the world of RoF, such as lower non linearity and reduction of chromatic dispersion effect at same as minimal set of front-end hardware components in the receiver/transmitter functions allowing the post-processing to be centralized [9].

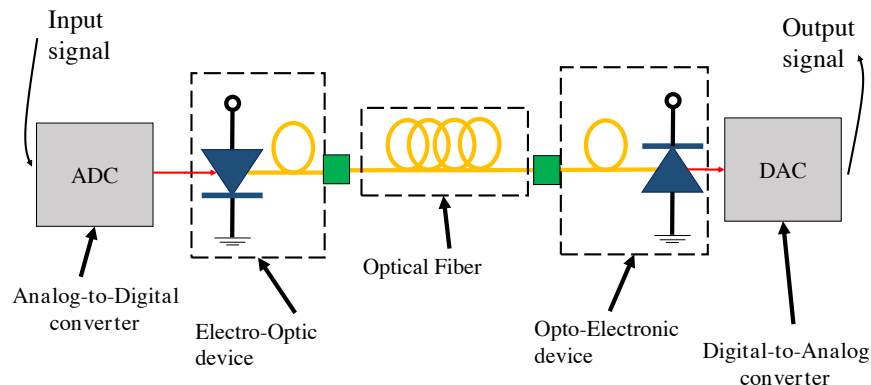


Figure 1.4: Typical D-RoF link schematic.

To be able to sample the RF signals also at high frequency it is necessary to apply the bandpass sampling technique [10]. Indeed, exploiting the fact that the Nyquist's theorem is only sufficient and not necessary it is possible to choose a sampling frequency f_s lower than the one of RF signal centered in f_{RF} having bandwidth B . In particular the condition to be fulfilled is:

$$\frac{2(f_{RF} - \frac{B}{2})}{k} \leq f_s \leq \frac{2(f_{RF} + \frac{B}{2})}{k-1} \quad (1.3)$$

in which k is an integer number which is ranged by the following expression:

$$1 \leq k \leq \left\lfloor \frac{f_{RF} + \frac{B}{2}}{B} \right\rfloor \quad (1.4)$$

in which $\lfloor \cdot \rfloor$ is the integer part operator. However, the trade-off in this case is given by the need of high performance ADCs and digital-to-analog converters (DACs) components able to operate at RF frequencies increasing the cost and complexity. Hence D-RoF is a more complex and costly RAP than the conventional RoF link.

Discussion on different techniques

This paragraph aims to give a summary of the techniques presented up to now giving an overall comparison. The scheme in Figure 1.5 divides the techniques in low cost and ease of implementation and high cost and high performances.

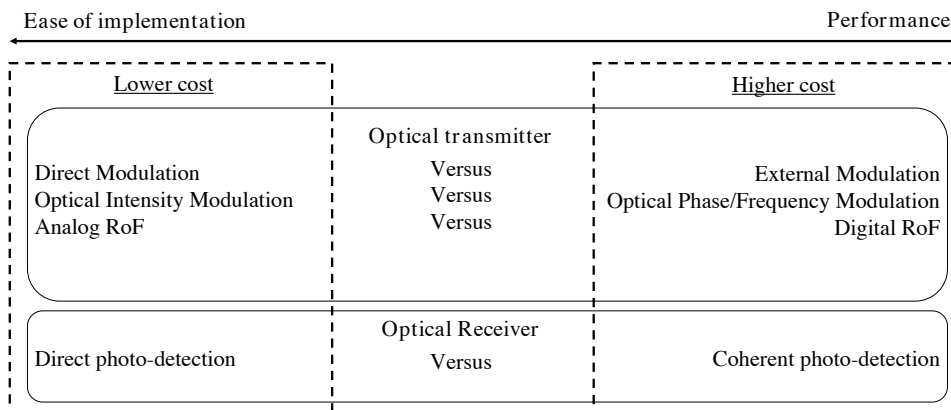


Figure 1.5: Summary of the advantages and trade-off among the different RoF techniques and architectures [5].

Architectures based on direct analog intensity modulation and direct detection (IM-DD) are therefore of easier implementation, but lower performances compared to architectures based on more complex modulation schemes and detection, which are used to get higher performances but leading to more expensive system.

Therefore, for the presented work, the focus is kept on the systems based on IM-DD A-RoF architecture because of the lower cost compared to the other architectures. Indeed, this analysis is independent on the choice of the link components such as type of transmitter or receiver, but regards only transmission and reception techniques. The implementation of particular devices, which are nowadays low cost, will improve the RoF system, as it will be explained later in the Chapter.

In the next Section, possible applications of such RoF architectures are presented, considering those applications as target for the developed low cost and consumption RoF link.

1.2 RoF applications

The purpose of this section is to show the current use of RoF systems in different application scenarios. Indeed, any type of RoF technology shown before can be implemented in any of the following applications. However, depending on performances and costs required one architecture can be more/less convenient.

Cellular networks

The main application of RoF is currently within the cellular networks. The system is generally used to extend the wireless coverage in such places that, for many reasons, are electrically shielded and the wireless propagation is not suitable to reach the desired performances. This is the case for railway tunnels for example, in which one main antenna or BaseBand Unit (BBU) is located outside the tunnel to communicate with the network, while inside the tunnel, many RAPs are present, connected each other with the optical links to provide the users full access to the network. The other scenario in which RoF is currently employed regards the crowded environments. Indeed, when the number of users is very high and dense, as it happens in stadiums, airports and shopping malls, the number of cells must be adequate in order to handle all the accesses and data traffic generated by the users. Therefore, the number of cells must be increased within the environment, connecting all the access points using optical fiber, increasing hence the capacity. Both types of systems are included in Distributed Antenna System (DAS) (see Figure 1.6a), and although it can be realized in many different ways (e.g. hollow coaxial cables and bridge radio link), nowadays RoF is the most used and performing technology.

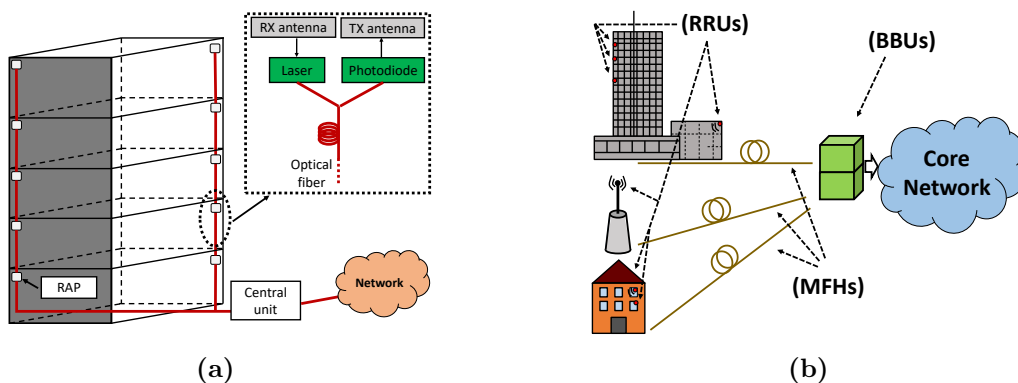


Figure 1.6: Typical RoF link schematic (a) and Example of centralized architecture of Radio Access Network (RAN) (RRU: Remote Radio Unit; MFH: Mobile Front Haul; BBU: Baseband Unit) (b).

Moreover, beside hard propagation environments, to improve further the capacity and flexibility of RANs in current (4G) and future (5G) architecture, the feature observed is the separation of the digital processing/management sections from the radio access ones reaching the end users (see Fig. 1.6b). Indeed in this way the former, which can have different

denominations, like BBU or Digital Unit (DU) section, can be centralized, which leads to a reduction of the related installation and maintenance costs and to an improvement of spectral efficiency through the adoption of appropriate cooperative algorithms. In addition, this makes it possible to realize functionalities like Network Function Virtualization (NFV) and Software Defined Network (SDN) [11–13].

As a consequence of this architecture, the radio access section can be constituted by large amounts of elements, which are typically indicated as Remote Radio Units (RRUs) and Remote Radio Heads (RRHs), Remote Access/Antenna Units (RAUs), or also Radio Dots (RDs), deployed with high capillarity and guaranteeing a high performance traffic available at each of the corresponding cells [14]. The Very Dense Network (VDN) which is created by this architecture, results to be based on the DAS concept, which allows to provide high capacity while minimizing cost and power consumption [15, 16].

Among the possible technologies adopted to realize the Mobile Front-Haul (MFH), which connects RRUs and BBUs (see again Fig. 1.6b), RoF is one of the most promising. Important advantages related to its adoption are indeed the low complexity required at the RRU stages, and the low requirements in terms of link throughput [17].

Summarizing, thanks to these features the IM–DD A–RoF technology constitutes a consolidated optimal solution for the coverage in non-Line of Sight (LoS) and/or crowded environments and can also be efficiently exploited for the realization of MFHs in alternative or in cooperation with the D–RoF technique, on which protocols like the Common Public Radio Interface (CPRI) or the Open Base Station Architecture Initiative (OBSAI) are based [18–23].

Home Area Networks

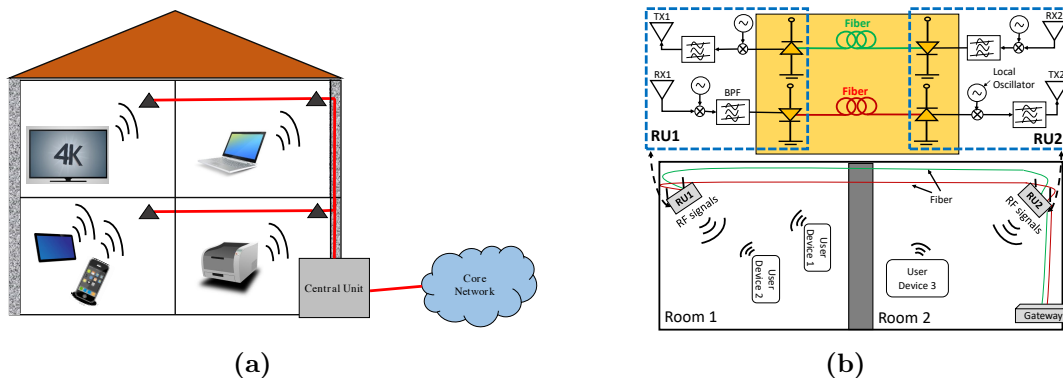


Figure 1.7: Example of HAN(a) and of two rooms RoF link architecture for wireless coverage extension and distribution (b).

Another important application in which RoF systems can be exploited regards the distribution of wireless signals for Home Area Networks. In particular, for new generation of WiFi standard 802.11ad [24] which operates at ISM high frequency band of 60 GHz it is very important to have an infrastructure which is able to distribute the signal within the

environment. The reason is related to the high operating frequency which produces higher losses compared to lower frequency WiFi standards (e.g. 2.4 GHz and 5 GHz). In fact the Free-Space Loss (FSL) is given by the following relation:

$$FSL = \left(\frac{4\pi d}{c} \cdot f \right)^2 \quad (1.5)$$

in which d is the distance, c is the light speed and f is the frequency considered. This means that at 60 GHz $FSL \simeq 60$ dB for the distance $d = 50$ cm. Indeed, this makes not possible a full wireless-based infrastructure which would require a huge amount of power transmitted and therefore high consumption of the RAPs.

RoF architecture is therefore a possible solution for the implementation of a 60 GHz WiFi network. An example of RoF-based architecture for HAN is shown in Figure 1.7a. The signal is distributed in the house exploiting one RAP for each room and connecting everything with optical fiber to a central unit which is connected to the network. The central unit has the main goal of handling the home network, in particular handling the handover when the user move through different rooms. A possible schematic of the RoF link is presented in Figure 1.7b in which the case of only two rooms is considered for simplicity. As it is possible to see, since the very high operating frequency, generally the IF technique is exploited to be able to use the RoF link. This technique consists in down-convert the passband electrical signal from the nominal frequency (in this case 60 GHz) to an intermediate frequency, which is set to be the optimum one for the RoF transmission. This allows indeed to reduce the cost, avoiding external modulators or very high frequency response lasers.

HANs are an example in which cost and consumption are very important, since the cost of the system directly affect the users, typically without any sharing. Many studies have been conducted on the possibility of use low cost VCSEL optical sources coupled with Multi-Mode Fiber (MMF) for 60 GHz WiFi systems [25], or exploiting the characteristics of Plastic Optical Fiber (POF) for multiband and standard transmission. [26]. The next step is to replace MMF with SSMF in order to decrease cost and re-use possible already existing infrastructure, as it will be discussed later in the Chapter.

Radio Astronomy

RoF systems find their utility also in radioastronomic plants where an antenna system (parabola, array, etc..) is used to monitor the RF spectrum of the sky.

In such systems, the received signal has to be transported from the receiving antenna to the baseband unit for post-processing and generally this unit is located hundred of meters far from the receiving system. Because of the very low power level of the received signals, maximum immunity to interference and low noise transmission channel are required. For this purpose, many radio astronomic plants exploit the advantage of optical fibers, which are completely immune by electromagnetic interference and allow easily to work with distances in the range of few kilometers thanks to the low fiber attenuation. Figure 1.8 shows a parabolic antenna downlink system based on RoF.

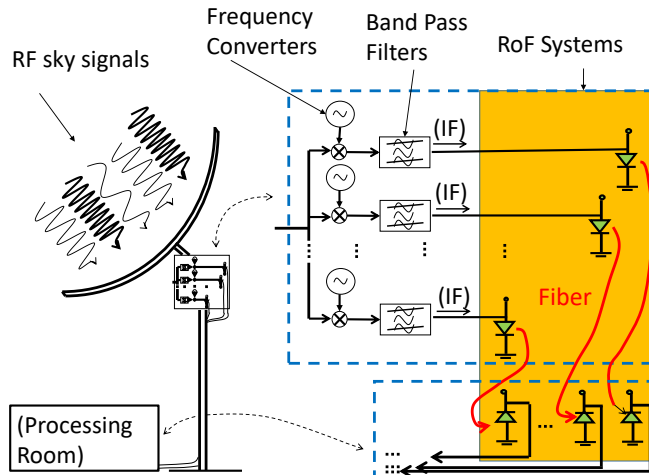


Figure 1.8: Example of RoF system for the downlink of parabolas for radio-astronomy.

Because of the wide frequency range of these type of antennas, which goes from few GHz up to tens of GHz, the system splits into many portions the received signals with the help of different bandpass filters (see Figure 1.8), and then through a local oscillator centers the signals in an IF and sends each signal to different RoF links. All the signals received at the processing room are then recombined and processed.

Recently, RoF has found also application in the Square Kilometer Array (SKA) project [27, 28], the Planar Array Feed (PAF) within the Australian Square Kilometer Array Pathfinder (ASKAP) [29] and the distribution of high quality local oscillator reference signals to reflector antennas. In all the cases, especially for SKA, where more than 200.000 antennas will be used to create two arrays in South Africa and Australia, the IM-DD A-RoF technique is utilized for minimizing the total cost of the system.

Discussion on challenges of such applications

Three main applications in which RoF architecture is exploited have been presented. In all the applications described, the common characteristics are the presence of crowded environment, the necessity of increase the receiving (or transmitting) points to enhance the performances (capacity for network, resolution and sensitivity for radio astronomic plants) or the very high frequency operation which increase the path loss (60 GHz operation). Those characteristics put immediately a strong constrain on cost and consumption of each single link. In the first part it has been shown how, among different techniques, IM-DD A-RoF architecture results to be the simplest one requiring the lowest cost to be implemented, therefore suitable for reducing the overall cost in such applications. Therefore, this architecture is considered in this work. Once the architecture is defined, what affects the cost of the link is then the choice of the components, which means the choice of laser and receiver technology and fiber type. The next Section is therefore dedicated to the description of the low cost components used in this study.

1.3 Low cost optical components

1.3.1 Silica-based optical fiber

Nowadays, the material most used to fabricate optical fibers is the pure Silicon Dioxide SiO_2 also known as Quartz [30]. This material allows to achieve very low attenuation compared with previous materials utilized, such as the amorphous glass, exhibiting low absorption coefficients in three wavelengths considered nowadays the possible operating windows for optical communication systems. These wavelengths correspond to 850 nm, 1310 nm and 1550 nm for which the optical attenuation coefficient is measured around 3 dB/Km, 0.4 dB/Km and 0.2 dB/Km, respectively. Even if it is not a proper name, the SiO_2 fibers are called also Glass Optical Fiber (GOF), to distinguish them from another fiber typology called Plastic Optical Fiber (POF), realized with a polymer called Poly(methyl methacrylate) (PMMA). In this dissertation only GOF fibers are considered since they are more suitable in view of possible future high capacity applications because of the limited bandwidth and high attenuation of POF.

From the manufacturing perspective, the optical fiber is constituted by an internal cylindrical part called *core* surrounded by another cylindrical structure, having larger transverse size and lower refractive index, called *cladding*. Controlling the refractive index difference among the two materials and their dimensions, it is possible to create an optical waveguide. The following law governs the number of propagating modes for optical field propagating at the wavelength λ :

$$V = \frac{2\pi a}{\lambda} \sqrt{n_1^2 - n_2^2} = \frac{2\pi a}{\lambda} \cdot NA \quad (1.6)$$

in which a is the core radius, n_1 is the core refractive index, n_2 is the cladding refractive index and NA is the so called numerical aperture. As shown in Figure 1.9 the number of modes depend directly on the value of V . Note that V is proportional to the radius of the core and the difference of the refractive indexes represented by the NA, while is inversely proportional to the operating wavelength. This means that, once the geometry and material properties are fixed, the waveguide behaves as single-mode or multi-mode depending on the propagating wavelength.

Two main SiO_2 -based fibers are classified as: Single-Mode Fiber (SMF) and Multi-Mode Fiber (MMF) which are standardized by the Recommendation ITU-T G.652 [31] and ITU-T G.651 [32], respectively. The characteristics of both standards are compared in Table 1.1. SSMF is defined to have a single mode behavior in second (1310 nm) and third (1550 nm) window, exploiting the low absorption coefficient of SiO_2 and therefore being suitable for high distance communications. Even though the numerical aperture is not defined by the standard, the typical value of current G.652 fiber in the market is $NA=0.14$ [33, 34].

Beside the low absorption coefficient, to be able to reach high distances and avoid signal distortion, SSMF must respect important requirements in terms of chromatic dispersion parameter $D_{\Delta\lambda}$. This parameter includes effect of waveguide and material dispersion which can cause distortion effects on the desired signal at high distances. Figure 1.10 shows the behavior

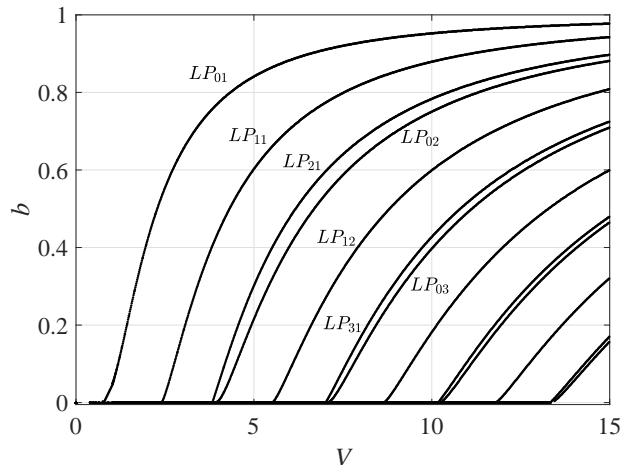


Figure 1.9: Normalized propagation constant b as function of the normalized frequency V .

of $D_{\Delta\lambda}$ defined by the standard G.652 and G.651 as function of the wavelength, highlighting the behavior in the three windows. SSMF presents $D_{\Delta\lambda} \simeq 0$ for $\lambda \simeq 1310$ nm and $D_{\Delta\lambda} \simeq 17$ ps/(nm Km) for $\lambda \simeq 1550$ nm, while a much higher value around 850 nm. Acting on the nominal manufacturing process it is possible to shift the zero-dispersion value to 1550 nm, making it possible to keep the same attenuation value. This fiber typology is defined by the G.653 standard and is called Dispersion-Shifted Fiber (DSF). Moreover, more recent single mode optical fibers of the same family of G.652 have been developed. In particular the G.652D, also called *Low Water Peak* has significantly reduced optical attenuation at water absorption wavelength around 1383 nm providing expanded transmission window from 1310 nm to 1550 nm continuously. Moreover, for Fiber-To-The-Home (FTTH) applications and Local Area Network (LAN)/Wide Area Network (WAN) networks, in which wiring spaces in buildings are very limited, a special fiber with bending radius of 15 mm (instead of 30 mm defined by G.652) has been standardized by the Recommendation ITU-G.657 [35] and is now widely present in the market.

Beside its nominal behavior in second and third window, the proposal of using the SSMF at 850 nm came out in the last recent years [36–40]. The reason lies in the possibility of integrating such type of fiber with 850 nm low cost devices which are now only used within MMF-based systems. However, SSMF is not designed to have a single-mode behavior at such frequency and due to this fact important phenomena occur such as modal noise and intermodal dispersion. Those phenomena are analyzed in details in Chapter 2, which is completely dedicated to the description of the electromagnetic propagation at 850 nm in SSMF.

The propagation characteristic of SSMF, considering the values in Table 1.1 is summarized in Figure 1.11 for all the three windows where the bi-modal propagation at 850 nm is highlighted.

Typically, for application operating at 850 nm the fiber type used is the Graded-Index (GI)-MMF, and is generally installed in short-distance communication systems. Historically, Multi-Mode Fiber (MMF) appeared before SSMF, due the easier realization of its larger core diam-

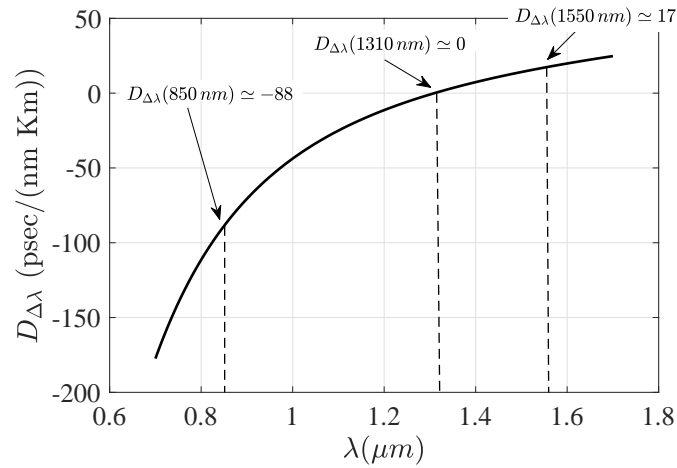


Figure 1.10: Curve of chromatic dispersion $D_{\Delta\lambda}$ according with the standard parameters and definition of [31, 32].

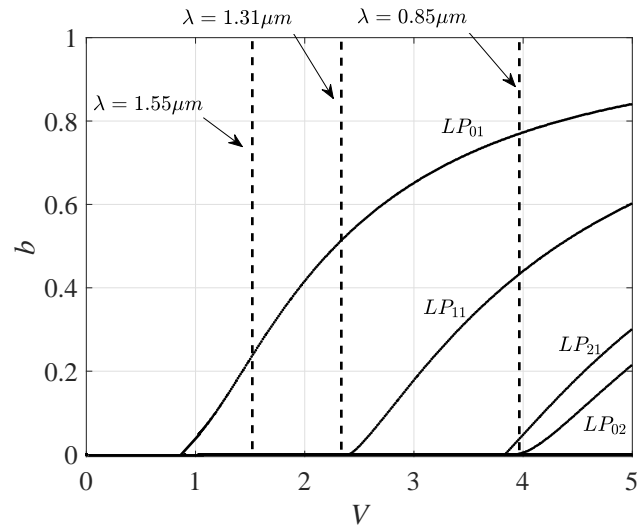


Figure 1.11: Propagation characteristics for the three window in SSMF considering the parameters defined in Table 1.1.

Attribute	Detail	Value G.652	Value G.651
Mode field diameter	Wavelength	1310 nm	N/A
	Nominal values	8.6 – 9.5 μm	N/A
	Tolerance	$\pm 0.6 \mu\text{m}$	N/A
Cladding diameter	Nominal	125 μm	125 μm
	Tolerance	$\pm 1 \mu\text{m}$	$\pm 3 \mu\text{m}$
Core diameter	Nominal	N/A	50 μm
	Tolerance	N/A	$\pm 3 \mu\text{m}$
Cladding concentricity error	Max.	N/A	6%
Cladding noncircularity	Max.	1.0%	N/A
Cable cut-off wavelength	Max.	1260 nm	N/A
Numerical Aperture	Nominal	N/A	0.2 or 0.23
	Tolerance	N/A	± 0.2
Macrobend loss	Radius	30 mm	N/A
	N. of turns	100	N/A
	Max. at 1550 nm	0.1 dB	N/A
Proof stress	Min.	0.69 GPa	0.35 GPa
Modal bandwidth-length product of overfilled launch	Min. at 850 nm	N/A	200 MHz · Km
	Min. at 1310 nm	N/A	200 MHz · Km
Chromatic dispersion coefficient	$\lambda_{0 \min}$	1300 nm	N/A
	$\lambda_{0 \max}$	1324 nm	N/A
	$S_{0 \max}$	0.092 ps/nm ² · km	N/A
	Typical at 850 nm	N/A	$\leq 120 \text{ ps}/(\text{nm} \cdot \text{Km})$
	Typical at 1310	N/A	$1 \leq 6 \text{ ps}/(\text{nm} \cdot \text{Km})$
Attenuation coefficient	Max. at 850 nm	N/A	4 dB/Km
	Max. at 1310 nm	0.5 dB/Km	2 dB/Km
	Max. at 1550 nm	0.4 dB/Km	N/A

Table 1.1: Standard G.652 parameters [31]

eter (nominal $62.5/50\mu\text{m}$) and same cladding size as SSMF (nominal $125\mu\text{m}$).

Besides the geometric dimension, the main characteristic of MMF is the graded-index profile of the core. Indeed, with $50\mu\text{m}$ of diameter it is straightforward from Equation (1.6) that the single mode operation in the three optical windows cannot be achieved since the nominal numerical aperture is $\text{NA}=0.2$. To overcome the problem of multi-mode propagation the solution is to replace the simple step function of the core refractive index profile with a custom function which gradually moves from the core index value to the cladding one (for example with a parabolic profile). Due to the graded profile the different propagating modes travel through the fiber with almost the same velocity up to a certain distance, guarantying the maximum possible modulation response of the fiber. Indeed, a trade-off between distance and bandwidth is present and enclosed in a parameter called *modal bandwidth*. This value measured at 850 nm is generally considered as key parameter of the MMF-based cables standardized by ISO/IEC 11801 (so called OM). All the OM designation and their relative characteristics are summarized in Table 1.2.

OM designation	Core diameter (μm)	OFL BW ($\text{MHz} \cdot \text{Km}$)		
		850 nm	953 nm	1310 nm
OM1	62.5	200	N/A	500
OM2	50	500	N/A	500
OM3	50	1500	N/A	500
OM4	50	3500	N/A	500
OM5	50	3500	1850	500

Table 1.2: ISO/IEC 11801 OM designation in which the modal bandwidth is presented for the case of OverFilled Launch (OFL).

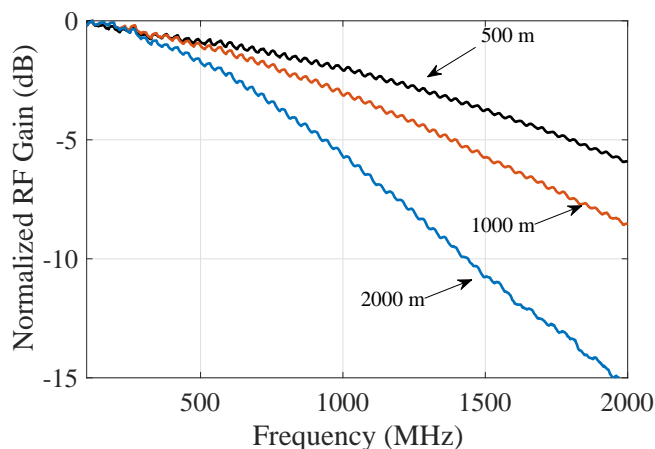


Figure 1.12: Example of OM3 modulation response for different lengths. Increasing the fiber length the fiber bandwidth decreases. The three curves are normalized to the laser response and to their maximum value.

Note that the OM5 has no improvement at 850 nm compared to OM4 but it has specification at 953 nm. This fact is related to possible use of such fiber in Shortwave Wavelength Division Multiplexing (SWDM) systems [41]. This technology consists in exploiting the Wavelength Division Multiplexing (WDM) technique, generally employed around 1310 nm or 1550 nm, at shorter wavelength. In particular, 4 channels spaced by 30 nm from 850 nm to 940 nm are used, being able to increase the data-rate up to 100 Gbps [42] for a maximum distance of 100 meters.

An example of effect of modal bandwidth is shown in in Figure 1.12 for an OM3 cable operating at 850 nm and excited by a Multi-Transverse-Mode (MTM) VCSEL source. This is the reason why typically MMF are employed in high data-rate short-range communications such as in data-centers where the distances to cover are in order of few tens of meters and the bandwidth required is in the GHz range.

Manufacturing processes and optical fiber production costs

The main part of the fibers used today are fabricated principally with material deposition methods called Vapour Deposited Silica (VDS). These methods were proposed to solve the bandwidth problems relative to the previous amorphous glass fibers, which gave low bandwidth and high attenuation principally due to high Numerical Aperture (NA) and material absorption characteristics. To increase the bandwidth, the possible ways are the reduction of NA, which can be obtained with graded index profile in MMFs, or with a drastic reduction of the core diameter to have only one propagating mode as happens in SSMFs. Moreover, because of the interesting properties of low refractive index and low absorption at optical frequencies, the silicon dioxide SiO_2 was chosen as main material for the fiber construction. Because of this changes, the manufacturing processes changed as well during the years. Methods used to realize amorphous glass fibers, e.g. *rod-in-tube* and *double crucible*, were good to realize step-index fibers with high core size and NA, but they had some important mechanical limitations which made the realization of the desired fiber not possible. The solution was the aforementioned VDS, divided in more specific categories, depending on the way of vapor doping, called Inside Vapour Deposition (IVD), Outside Vapour Deposition (OVD) and Vapour Axial Deposition (VAD). Omitting the processes details, the basic part is the realization of a preform with an initial rod of SiO_2 constantly heated up, and then starting to dope the fiber core using dopant gases, e.g. Germanium. After this process, the fiber manufacture is realized heating in a localized point the preform and drawing off the optical fiber into winding wheels. The fiber diameter is controlled by a measuring system directly connected to the wheels. The overall manufacturing costs depend finally on:

- **Preform cost**
- **Preform yield**
- **Production efficiency**

In fact, differently to large amorphous glass fiber manufacturing process, where the costs are related principally to the materials employed, in VDS methods the cost depends on the

perform numerical aperture. This parameter reflects the relative refractive index, thus the higher NA the higher the concentration of expensive dopants to use during the process. The realization of graded-index profile is more complicated than a simple step-index one, and takes much more time. Finally, preforms with high dopants concentration tend to be rather brittle, thus the yield can decrease with time. To conclude, independently of the kind of VDS method, it is clear that the manufacturing costs of SSMFs are lower than MMFs.

Market analysis of fiber optic cables and systems

To validate and actualize the discussion made in the previous section a market analysis has been performed in order to compare the current costs between multi-mode and single-mode fibers. In particular, the cost-per-meter of different fiber types and cables have been analyzed and reported here for FS.COM[®] (Table 1.3), OE Market[®] (Table 1.4) and Fiber24[®] (Tables 1.5a and 1.5b) fiber manufacturers.

Length (m)	G652	OM1/OM2	OM3	OM4	OM5
1	2.40	2.10	2.20	2.40	4.30
10	0.39	0.40	0.49	0.71	2.29
30	0.25	0.28	0.37	0.58	2.14
1000	0.17	0.22	0.30	0.52	2.05

Table 1.3: FS.COM[®] optical fiber cost-per-meter (€/m) for duplex cables ended with LC/UPC connectors.

Length (m)	G.652	G.657	OM3
1	7.99	10.9	7.95
5	1.92	2.58	2.19
1000	0.10	0.10	0.22
5000	0.08	0.09	0.22

Table 1.4: OE Market[®] optical fiber cost-per-meter (€/m) for simplex cables ended with LC/UPC connectors.

Length (m)	G652	OM2	OM3	OM4
25	1.08	1.09	1.23	1.41
300	0.29	0.35	0.37	0.54
500	0.26	0.32	0.39	0.59

(a)

Length (m)	G652	OM2	OM3	OM4
25	0.61	0.64	0.80	1.1
300	0.41	0.48	0.62	0.92
500	0.40	0.47	0.62	0.91

(b)

Table 1.5: Fiber24[®] simplex optical 4-core outdoor(a) and indoor(b) cable cost-per-meter (€/m) ended with LC/UPC connectors.

For all the vendors it is clear how the cost-per-meter depends on the fiber length. For very short fiber (patch-cord) the cost-per-meter results to be quite similar and high between G.652 and OM fibers. The values start then to decrease rapidly already for tens of meters for which the cost-per-meter of G.652 is lower than OM fibers for all the three vendors. Increasing further the distances to hundred of meters the discrepancy of cost-per-meter becomes larger, reaching higher spreading for kilometers-range fibers for which the cost-per-meter of OM cables is almost 3-times the one of G.652 cables.

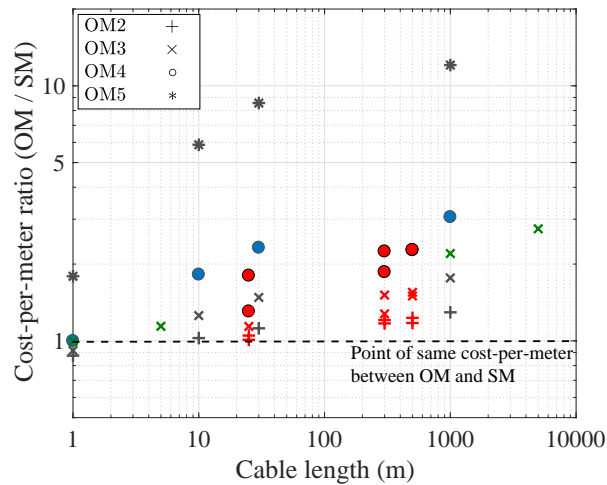


Figure 1.13: Cost-per-meter ratio of all the manufacturers analyzed for the different fiber typologies. The colors differentiate the different fiber producers, FS.COM[®] (grey), OE Market[®] (green) and Fiber24[®] (red).

Figure 1.13 shows the cost-per-meter ratio (OM cables cost over SM cables cost) for all the fiber typologies and producer presented here. This graph put strongly in evidence the higher cost-per-meter of MMF compared to SSMF. Beside the costs, the use of SSMF is more suitable for future applications thanks to lower limitation in terms of bandwidth with respect MMF. Moreover, SSMF is currently deployed and installed in urban environment for FTTH applications, and it would be interesting to exploit the possibility of re-using the already existing infrastructures.

1.3.2 Short wavelength VCSEL technology

The first concept about the possibility of realizing lasers devices which could emit in the direction perpendicular to the wafer surface was proposed in 1977 by Prof. Kenichi Iga [43]. The necessity of having such new type of lasers came up to solve some issues related to Edge Emitting Lasers (EELs). For example, the impossibility of testing the latter devices before cutting the wafer and separating into chips, or the limitation on the monolithically integration of such lasers into optical circuits due to the finite cavity length [44].



Figure 1.14: Top view of a VCSEL.

Since this first publication, VCSELs have been studied by many researchers which gave important contribution to the improvement of this technology. In particular, in 1989 J.Jewell reported the first full-monolithic VCSEL composed of epitaxially grown Distributed Bragg Reflectors (DBR) and InGaAs-GaAs Quantum Wells (QWs) active region [45]. As it will be explained in a later section, the realization of regular Multi-Quantum Wells (MQWs) lead to the important reduction of threshold current keeping high the output optical power. Therefore, thank to their overall benefits, MQWs became a constant presence in VCSEL active regions. Note that this type of technology is not exclusive of VCSELs but it is used also in EEL [46, 47]. The success of MQWs-based VCSELs came at the same time with the development of manufacturing techniques such as Metal-Organic Chemical Vapor Deposition (MOCVD) and Molecular Beam Epitaxy (MBE) which give the possibility of growing materials with very small thickness and high precision.

In fact, these two techniques allow to control the material grown layer by layer, realizing structures with a precise doping and sharp interfaces between different materials. With thickness of few nanometers, electron's De Broglie wavelength is comparable with the spatial dimensions, at least in one of the three directions, and quantum effects are observed. Quantum wires and quantum dots are present if, respectively, two or three dimensions are involved. Instead, QWs occurs in heterostructures realized with materials of different energy bandgap, e.g. GaAs and GaAlAs.

Realizing more than one QW increases the gain, and implies less consumption of bias current than a bulk laser because of the smaller volume of the active region. The PIN-type doping scheme is similar to conventional EELs. In the most simple device layouts, electric current is

injected from ohmic contacts on the top epitaxial side and the backside of the substrate [48]. Nowadays VCSELs are a well-consolidated technology which is already present in many applications such as the high-speed communications in data-centers [49–51] or proximity sensors in mobile devices [52] as for example the iPhone provided by Apple [53] .

VCSELs vs. EELs

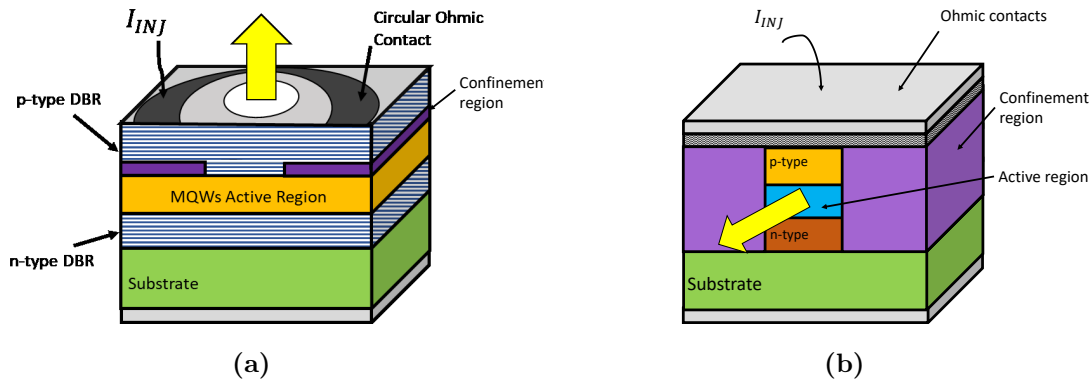


Figure 1.15: Typical structure of GaAs VCSEL (a) and EEL (b).

As the name says, the main characteristic of a VCSEL is the emission direction of the light, which is not from the edge, like other kinds of laser such as Distributed Feed-Back (DFB) or Fabry-Perot (FP), but it is from the top of the structure (see Figure 1.15). This fact gives many advantages compared to EELs: first of all the production cost can be reduced thanks to the possibility of realizing several tens of thousand of VCSELs in the same wafer and testing directly on it. This, indeed, is not possible for EEL for which the wafer must be sliced to test the behavior of each sample from the edge, increasing the time and cost of the testing reliability process. Moreover, because of the compact size of VCSEL, typically $250 \times 250 \mu m^2$ there could be more devices on a wafer than EEL and therefore the production could be done in larger quantities without any type of additional cost.

Summarizing, the advantages of VCSELs compared to EEL are:

- Lower threshold current;
- Higher efficiency but lower emitted power;
- Lower cost;
- Possibility of creating VCSEL arrays without any additional manufacturing cost;
- Higher density of chips in one wafer;
- Narrow beam divergence and circularly symmetric profile;
- Higher modulation bandwidth due to the short photons lifetime, which leads to a high oscillation relaxation frequency.

- Easier matching at typical RF impedance (50Ω or 75Ω)

VCSEL physical structure and behavior

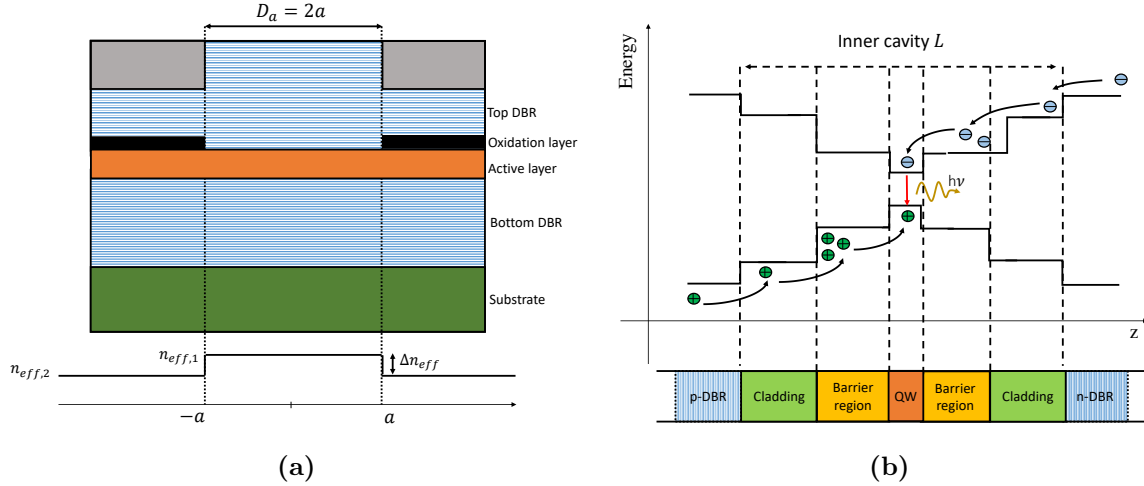


Figure 1.16: Side view of a VCSEL (a) and example of single QW active region (b).

Next, the physics of VCSELs is described in some details for a better understanding of their properties and behavior.

The physical structure of GaAs VCSELs is composed by the following components:

Top and bottom DBR: DBRs are typically used to generate a resonant cavity. They consist of alternating pairs of semiconductor materials (generally alloys) having different refractive index. In the case of VCSEL operating at 850 nm or 980 nm the material employed is typically $\text{Al}_x\text{GaAs}_{1-x}$ in which the parameter x changes between the two layers. This difference causes a refractive index separation between the layers. The layer thickness is designed to be $\lambda/4n$ where n is the layer refractive index and λ is the desired resonant wavelength. Because of the current flow from the contact through the mirrors, they are also doped to reduce the series resistance [54]. Moreover a single-step grading with 5 nm thick layers of intermediate bandgap energy is used to reduce the electrical series resistance [55] realizing a *graded-DBR*. Finally, the bottom DBR has more reflectivity than the top one, to let the light go out only in one direction.

Active region: for the laser operating in the wavelength considered ($\simeq 850$ nm), the active structure is composed generally of few QWs realized in GaAs with some 10nm thickness. In particular the active region consists of half-wavelength thick $\text{Al}_{0.2}\text{Ga}_{0.8}\text{As}$ with three 8 nm thick unstrained GaAsQWs separated by 10 nm barriers in the center. Quarter-wavelength $\text{Al}_{0.5}\text{Ga}_{0.5}\text{As}$ cladding layers are introduced on both sides of the active region to improve longitudinal carrier confinement [48].

Confinement region: it is responsible for the confinement of the electrons in the active region. Actual VCSELs adopts oxide or double-oxide confinement with unrivaled performance [56, 57], exploiting selective lateral oxidation of an about 30 nm thick AlAs. This technology has replaced the initial most common technique based on proton implantation, because of the higher optical losses in the cavity of the latter compared to the oxide [56, 58].

VCSEL emission spectrum behavior

In this paragraph, the emission optical spectrum of VCSELs is analyzed in detail. Their small effective cavity length in the emission direction guarantees only one longitudinal mode within the cavity. Indeed, when the wavelength λ is fixed ($\simeq 850$ nm), only a set of lengths L is admitted to have the resonance condition. In particular, the following condition is necessary for the inner cavity length:

$$L = \frac{\lambda}{2\bar{n}}m \quad m = 1, 2, 3\dots \quad (1.7)$$

in which \bar{n} is the spatial average refractive index. For VCSELs typically is $m = 2$, since for $L = \frac{\lambda}{2\bar{n}}$ the current injection efficiency results to be low [48]. This results in $L = \frac{\lambda}{\bar{n}}$ which for the case of $\lambda = 850$ nm and $\bar{n} \simeq 3.6$ (e.g. GaAs) leads to $L \simeq 236.11$ nm. This value regards the *inner* cavity length (distance between top and bottom DBR). However, the actual cavity that is present in VCSELs takes into account also the presence of the two mirrors. In particular, an effective length l_{eff} for both mirrors can be calculated, making the assumption that the reflection effectively originates from a hard mirror with identical peak reflectivity placed at a distance l_{eff} . From this consideration it is possible to define a *effective* cavity length L_{eff} defined as:

$$L_{eff} = L + l_{eff,t} + l_{eff,b} \quad (1.8)$$

where $l_{eff,t}$ and $l_{eff,b}$ are top and bottom DBR effective length, respectively. Therefore L_{eff} depends on the DBR properties (e.g. number of mirror pairs) and generally is in the order of 1 μm [48, 59].

The longitudinal mode spacing among the possible wavelength for a cavity of length L_{eff} is given by [48]:

$$\Delta\lambda = \frac{\lambda^2}{2\bar{n}L_{eff}} \quad (1.9)$$

Therefore, since L_{eff} is of the same order of magnitude of λ in VCSELs, a large spacing among the possible propagation wavelengths occurs, resulting in $\Delta\lambda \simeq 110$ nm. This value is much larger than the material gain bandwidth, which is in general about 50 nm, and consequently only a single longitudinal mode emission is allowed.

However, due to the transverse size of the device an actual multimode emission occurs. A cylindrical structure is typically created with $D_a = 2a$ as aperture diameter (see Figure 1.16). The oxidized layer, which is used for confining the injected current, also lowers the refractive index (from ~ 3 to ~ 1.6 at wavelength of 850nm [60]). This provides transverse optical

confinement, forming a waveguide for light which propagates in the longitudinal direction. Applying the effective index analysis given by Hadley [61] it is possible to understand the presence of a waveguide. This analysis assumes that any modification of the VCSEL resonator that produces a local shift of the resonance wavelength $\Delta\lambda_0$ produces a corresponding change of the effective index Δn_{eff} (see Figure 1.16) in that region for which holds the relation:

$$\frac{\Delta n_{eff}}{n_{eff}} \approx \frac{\Delta\lambda_0}{\lambda_0} \quad (1.10)$$

Because the oxidation layer lowers the effective refractive index of the material, it is $\Delta\lambda_0 < 0$ and therefore $n_{eff,2} < n_{eff,1}$. Therefore, a cylindrical waveguide of diameter D_a having an effective refractive index difference Δn_{eff} is present, which allows to apply the theory of the step-index optical fiber for analyzing the guiding characteristics. Therefore, assuming the weakly guiding approximation $\Delta n_{eff} \ll n_{eff}$ the modes can be expressed in terms of linearly polarized modes $LP_{l,p}$ in which l and p are the azimuthal and radial mode numbers, respectively. Because of the blue-shift given by the oxidation layer the fundamental mode LP_{01} is the one with higher wavelength compared to the higher order ones. An example of emission spectrum for different biasing conditions of a VCSEL is shown in Figure 1.17.

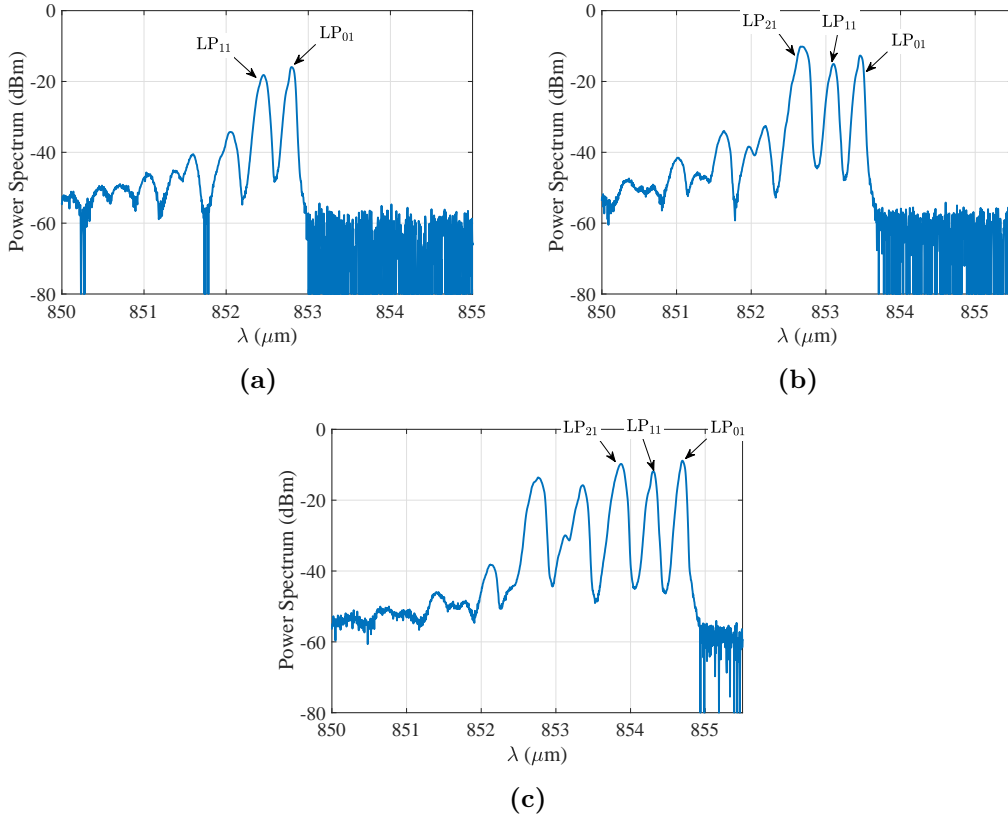


Figure 1.17: Example of optical spectrum measured for a typical oxide confined MTM VCSEL realized on GaAs. The spectrum is measured for $I_{bias} \simeq I_{th}$, $I_{bias} \simeq (I_s - I_{th})/2$ and $I_{bias} \simeq I_s$ current for the real wavelength.

Indeed, it should be pointed out that any deviation of the refractive index profile from the assumed symmetry leads to a more complex transverse mode spectrum which is not possible to describe with the previous approach. In fact three different kinds of problems: electrical, thermal and optical have to be solved considering their mutual couplings. For more details, see [62–64].

Finally, varying the bias current the output field will change in its shape and its frequency (red-shift) with possibly a different number of modes emitted. This last phenomenon is due, beyond the variation of the refractive index of the structure, by spatial hole burning [48] which cause the excitation of lateral modes. Figure 1.18 shows those effects for a MTM VCSEL.

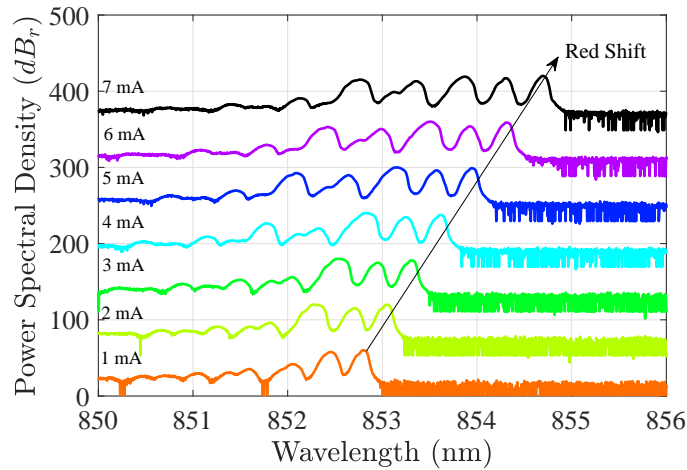


Figure 1.18: Example of spectrum variation changing the biasing current for a MTM VCSEL realized in GaAs.

1.3.3 SiGe HPT technology

HPT generalities

Hetero-junction bipolar Photo-Transistor (HPT) is an opto-electronic device based on the fully-electronic Hetero-junction Bipolar Transistor (HBT) in which an optical window is designed to enable the light interact with the device. Moreover, some of its layers are made of optical absorbing material, especially in the base-collector region to be able to operate as an opto-electronic device. HPT is a good candidate as microwave photo-receivers and, due to the hetero-junction, they could be called microwave photo-transistors, as opposed to low speed homo-junction photo-transistors used in sensor or opto-coupler applications. The performance of HPT, as any other phototransistor, is supported by their internal current gain, not present in PIN and Schottky Photo-Diode (PD). In addition, unlike Avalanche Photo-Detectors (APDs), HPTs do not suffer of extensive noise due to avalanche effect. This advantage, and their process and layer compatibility to hetero-junction bipolar transistor, makes them highly attractive in manufacturing single chip optical receiver [65].

Generally, in phototransistor, the base-collector region behaves as a PIN photo-diode and injects the photo-generated current into the base (holes) and collector (electrons). The photo-generated current goes through the base and is then amplified. If I_b is the base current and I_{ph} is the current produced by the electron-hole generation due to the injected light, the collector current I_c in case of light injection is given by:

$$I_c = \beta(I_b + I_{ph}) \quad (1.11)$$

in which

$$\beta = \frac{I_{c,dark}}{I_b} \quad (1.12)$$

where $I_{c,dark}$ is the collector current in case of no light injection (dark condition). Indeed, in this way, beside I_b , also the photo-current exploits the amplification properties of the transistor.

Different hetero-junction media have been studied and utilized for fabrication of HPT, such as AlGaAs/GaAs [66], InGaP/GaAs [67] and SiGe [68, 69] working at 800-980 nm range or InGaP/InP working at 1550 nm [70].

Among the aforementioned material compositions, SiGe HPT is the highest potential candidates to implement high speed photo-detectors directly integrated within SiGe BiCMOS radio chips for high-speed transceivers in communication networks. In particular, this component has the advantage to determine low cost optical link thanks to the well matured SiGe HBT technologies as it enables to fabricate the phototransistor.

The first SiGe phototransistor developed in standard SiGe HBT technology was presented in 2003 [71, 72]. The structure has $10 \times 10 \mu\text{m}^2$ optical window opening in the emitter through which the light penetrates (see Figure 1.19). A DC responsivity of 1.47 A/W and 3 dB modulation response of 0.4 GHz were achieved for 940 nm.

SiGe HPTs have been further investigated by various laboratories using different industrial process technologies such as TSMC [73], IBM SiGe BiCMOS [74] and AMS SiGe BiCMOS [75].

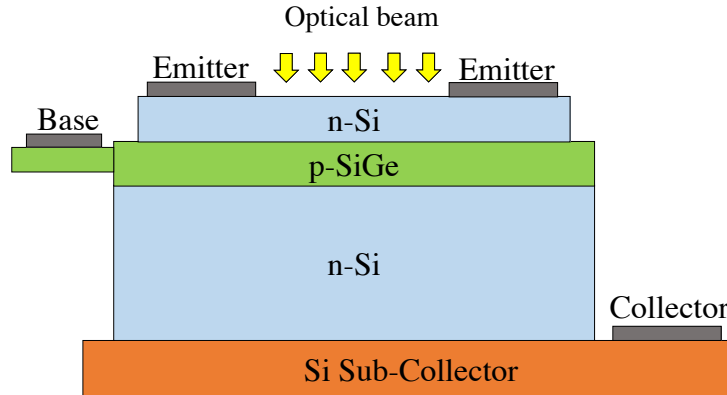


Figure 1.19: Sketch of the vertical stack of the SiGe fabricated in [71, 72]

The SiGe HPT employed in this work is of the same technology of the one presented in [76] and it has been fully characterized in terms of Responsivity, cut-off frequency and substrate effects through the so-called Scanning Near-field Optical Mapping (SNOM) technique [77] employing a $50\ \mu\text{m}$ diameter MMF. Moreover, it has been already investigated the possibility of employing this device for MMF-based RoF link in 60 GHz WiFi transmission systems integrating a Low Noise Amplifier (LNA) for HANs reaching data rate transmission of 3.04 Gbps [78].

Physical structure and electrical properties of the HPT used in this work

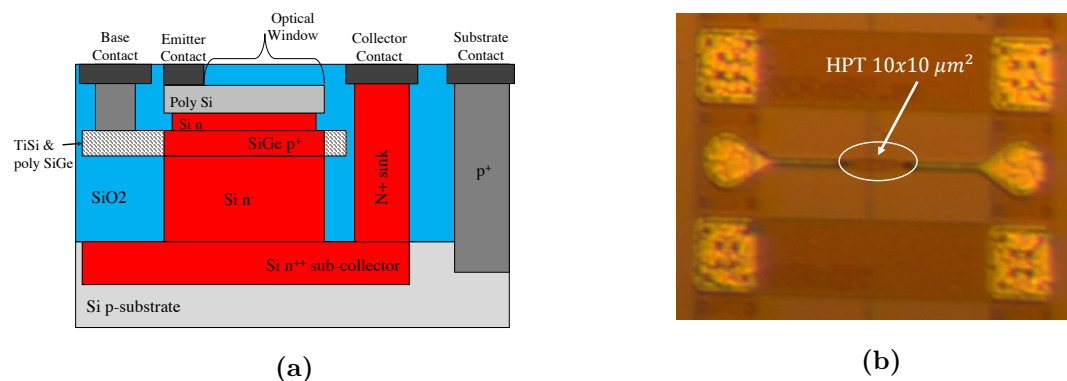


Figure 1.20: Structure and technology of the SiGe HPT studied and employed.

The device employed in this work has been designed by ESYCOM Laboratory and the fabrication is based on an industrial SiGe2RF Telefunken GmbH technology, which provides circuits working above 10 GHz and potentially up to 60 GHz in some configurations [79]. A particular layout configuration was realized to open an optical access for vertical illumination of the base collector region without modification of the vertical stack of the original industrial process technology. The SiGe base layer was sandwiched between the collector and the emitter,

both made of Silicon. The basic HPT structure was developed by extending base, emitter and collector layers of the HBT. A $10 \times 10 \mu\text{m}^2$ optical window size was realized since it has been found to have the best behavior in terms of its frequency response with a responsivity of 0.4 A/W using MMF [80].

The phototransistor can operate in three different modes:

- 3T PD mode: The base voltage (V_b) is lower than the threshold voltage ($V_{b,th}$), this prevents the transistor behavior. Thus, the device works as a photodiode.
- 3T HPT mode: It is $V_b \geq V_{b,th}$. In this mode, there is direct detection of light (so photocurrents are generated) and internal amplification of the photocurrent by the transistor effect of the device. Hence, the opto-microwave gain in HPT mode is higher than under PD mode operation. In the following, with “HPT mode” it is intended the condition where V_b assumes the value in which the Responsivity was found to be maximum [80].
- 2T mode: The base is left unconnected ($I_b = 0$). This configuration can be utilized provided that the HPT device must not feature functionalities for which the base current plays a fundamental role (like for example the possible operation as a mixer).

Figure 1.21 shows the Gummel plot of the HPT showing the respective behavior of β (see (1.12)). This quantity represents the total amplification effect of a typical HBT. In Section 3.3 it will be shown how this behavior is related to the responsivity and noise of the HPT.

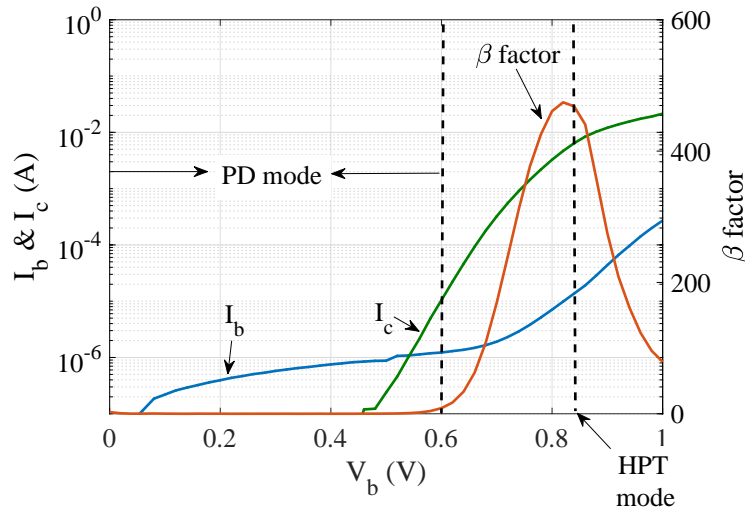


Figure 1.21: Gummel plot, fixing $V_c = 2$ V, of the HPT employed in this dissertation in dark condition.

Figure 1.22 shows instead the behavior of I_c as function of V_c for different I_b applied when no light is injected. This graph represents the dark condition of the devices, which

is indeed different when the base current values change. From Figure 1.22 it is possible to observe also that there is a sharp increase of current after $V_c = 3.5$ V. This it is related to the avalanche/breakdown condition reached by the phototransistor for such value of V_c . This suggest indeed to take $V_c \leq 3$ in order to avoid damage or avalanche effects generated by the device.

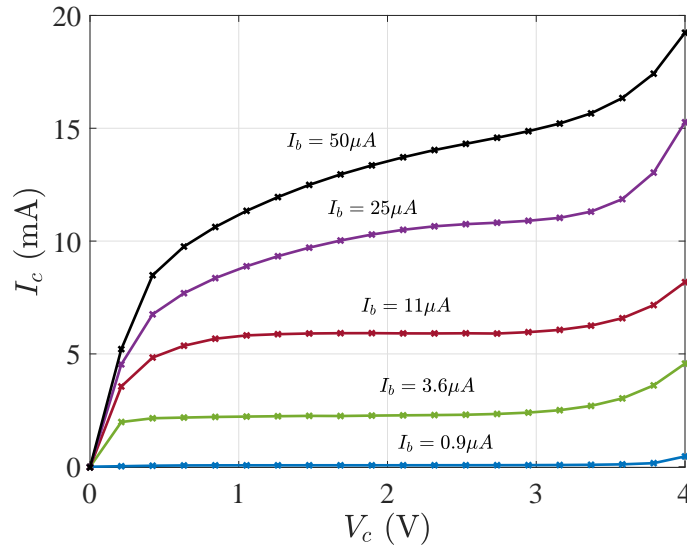


Figure 1.22: I_c characterization with respect to V_c .

The behavior of β is also represented in Figure 1.23 varying V_c showing a small enlargement passing from 1 V to 3 V.

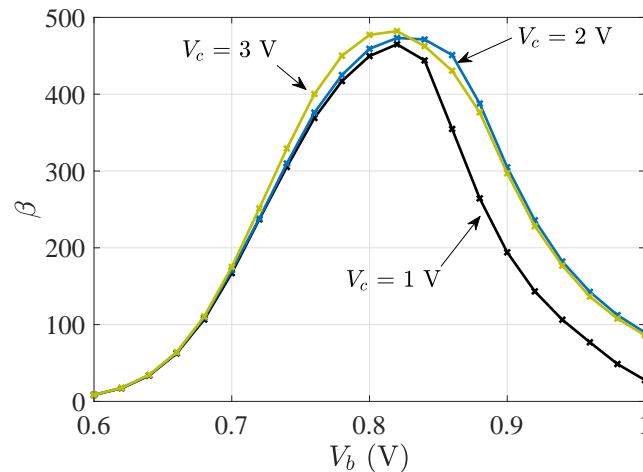


Figure 1.23: β factor as function of V_b taking V_c as parameter.

Considering Figures 1.22 and 1.23 an approximate value of $V_c = 2$ V can be consider as good in terms of performances. This is in agreement with the consideration reported in [76,81].

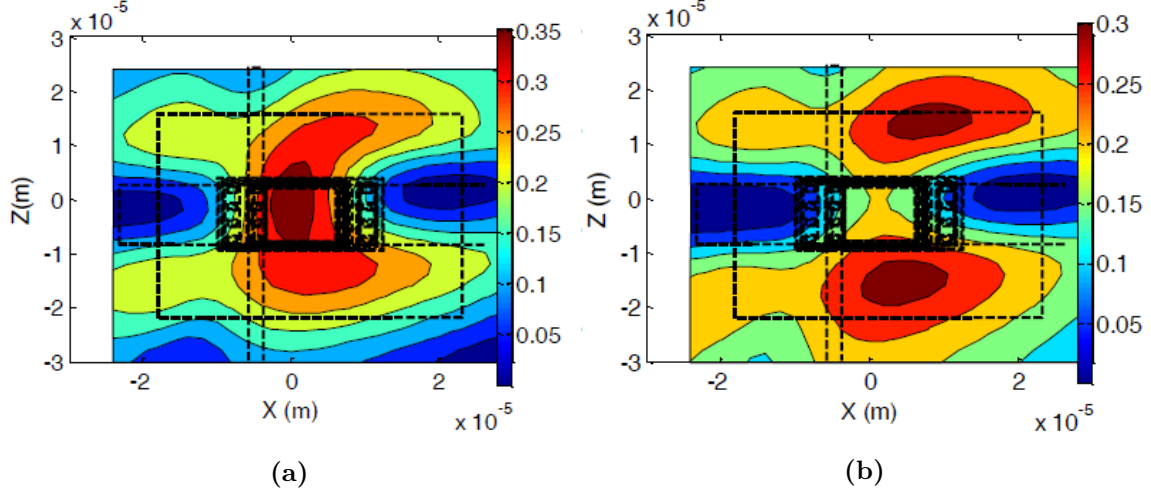


Figure 1.24: Mapping of the Responsivity \mathcal{R} in (A/W) measured in both HPT and PD modes of SiGe HPT under study. The measurement has been performed injecting light from a MMF excited by a MTM VCSEL [76].

Important metrics and definitions to describe the SiGe HPT behavior

This Section aims to define some basic quantities which will be used in Section 3.3 for the characterization of the SiGe HPT in presence of SSMF.

Hereafter, some important concepts and parameters which have been derived in [76] are reported.

The internal properties of SiGe HPT could change due to the impact of the light sensitive Silicon substrate. This effect, already discussed in [76] with MMF, can have a big impact on the total responsivity of the device. The evidence of this effect is related to the fact that for other type of HPT, such as the ones based on InGaAs/InP, the typical condition under light injection is $I_{c,PD} = I_{b,PD}$ in which $I_{c,PD}$ and $I_{b,PD}$ are the measured current in PD mode for collector and base respectively [70].

In case of Silicon-base HPT this condition is not respected, and typically $I_{c,PD} \geq I_{b,PD}$. This can then be related to parasitic effect of the Silicon substrate which is therefore not transparent at the considered wavelength ($\simeq 850$ nm). Indeed the absorption coefficient becomes low for wavelength greater than 1100 nm.

The substrate photocurrent is defined as [76]:

$$I_{c,sub} = (I_{c,PD} - I_{c,PD,dark}) - (|I_{b,PD}| - I_{b,PD,dark}) \quad (1.13)$$

in which $I_{c,PD}$, $I_{c,PD,dark}$ and $I_{b,PD}$, $I_{b,PD,dark}$ are the measured currents with and without light injection, of collector and base respectively.

The total collector current measured in PD mode is then influenced by the substrate current when light is injected. For this reason, the inherent photo-current generated in PD mode can be written as follows:

$$I_{c,PD,i} = I_{c,PD} - I_{c,PD,dark} - I_{c,sub} \quad (1.14)$$

From this concept it is then possible to extract the intrinsic responsivity of the device \mathcal{R}_i as

$$\mathcal{R}_{PD,i} = \frac{I_{c,PD,i}}{P_{opt}} \quad (1.15)$$

Defining now the total responsivity as

$$\mathcal{R}_{\mathcal{PD}} = \frac{I_{c,PD} - I_{c,PD,dark}}{P_{opt}} \quad (1.16)$$

it is possible to individuate the contribution given only by the substrate

$$\mathcal{R}_{sub} = \frac{I_{c,sub}}{P_{opt}} \quad (1.17)$$

which gives directly

$$\mathcal{R}_{\mathcal{PD}} = \mathcal{R}_{PD,i} + \mathcal{R}_{sub} \quad (1.18)$$

The substrate contribution is indeed present also in HPT mode. Therefore, after the computation of the substrate current from PD mode, the same value will be used to extrapolate the quantities $I_{c,HPT,i}$ and $\mathcal{R}_{HPT,i}$. Those quantities can be measured for different points of the HPT, creating a map of the currents and responsivity. Figures 1.24a and 1.24b show an example of SNOM measurement of the responsivity using a MMF coupled with a MTM VCSEL. The results are related to a high resistivity substrate, which have been widely studied in [76].

1.4 Summary and Discussion

In this Chapter the fiber optic based communication technology known as RoF has been introduced in its main aspects. In particular different architectures have been presented and a cost/performance analysis has been provided. Moreover, the manifold applications in which RoF technology can be exploited have been presented showing the heterogeneity and the flexibility of such technology. In all the applications presented, costs and consumption are considered as main challenge for future implementations. For this purpose, the RoF link considered in my work is based on three fundamental components which have been describes in this chapter.

The characteristic of the SSMF are described, focusing on the possibility of using such fiber for wavelengths lower than the cut-off, allowing a multimode propagation. The reason of this choice is that the usage of SSMF allows to decrease further the costs thanks to the manufacturing process and possible re-use of the infrastructures, without installing new cables.

850 nm VCSELs technology has been described in details, analyzing the physical behavior of the device showing the advantages of such technology with respect to EELs which make them suitable for low cost applications.

Finally, on the receiver side, the SiGe HPT has been described as possible high potential photo-detector to be implemented in all the applications described, thanks to its silicon-based technology which allows easy integration of silicon-based electronic devices.

850nm propagation in standard G.652 fiber

In this Chapter a detailed mathematical model for the propagation in SSMF at operating wavelengths below the nominal cut-off wavelength is presented. In particular, the attention will be given to wavelengths around 850 nm, since this is a particular case of interest for low cost applications. As explained in Chapter 1, when the geometry and refractive index of the materials are fixed, decreasing the operation wavelength results in an increased number of propagating modes. In this sense, to operate at 850 nm means to change the nominal propagation of the SSMF from single- to multi-mode. Hence, the model is able to describe in detail phenomena that are typically present in multi-mode environments such as modal noise and intermodal dispersion.

Sections 2.1,2.2 and 2.3 introduce the mathematical model, describing the main effects and analyzing possible solution to mitigate modal noise and intermodal dispersion.

Sections 2.4 and 2.5 show how is possible to reversely calculate the chirp coefficient of the laser source exploiting the two-modes propagation in a optical system.

Finally in Section 2.6 discussion and summary of the Chapter are given.

2.1 Direct modulation of a semiconductor laser

Intensity modulation

Referring to the case of a VCSEL source, the electrical field of a generic optical multi-wavelength source operating around 850 nm is considered. As it has been shown in Chapter 1, such type of laser emits a finite number of wavelengths which have different intensities. Therefore, the total electrical field \bar{E}_L emitted by the laser can be expressed in its complex form as:

$$\bar{E}_L = \sum_{k=1}^{N_W} \bar{E}_{L,k} = E_0 \sum_{k=1}^{N_W} c_k e^{j(\omega_{0,k}t)} \bar{e}_k \quad (2.1)$$

This chapter is based on the results published in P.4, P.3, P.1 and P.10

where N_W is the number of wavelengths emitted by the laser, $\omega_{0,k} = 2\pi f_{0,k}$ is the optical angular frequency of emission, \bar{e}_k the unit vector and c_k the complex relative coefficient of the k -th wavelength given by the following expressions:

$$c_k = \frac{\bar{E}_{L,k}}{|\bar{E}_L|} \quad (2.2)$$

from which it is possible to compute the relative power coefficient p_k given by

$$p_k = |c_k|^2 \quad (2.3)$$

This coefficient represents the percentage of power carried by the k -th line, and then $\sum_{k=1}^{N_W} p_k = 1$ [82]. The field amplitude $E_0 = |\bar{E}_L|$ is given by the well-known relation:

$$E_0 = \sqrt{2ZP_0} \quad (2.4)$$

in which Z is the wave impedance and P_0 is the optical power. The amount of power emitted by a laser is related to the biasing current through a parameter called *slope-efficiency* or *responsivity* η defined as follow:

$$\eta = \frac{dP_0}{dI_{bias}} \quad (2.5)$$

Considering the laser diode operating in linear region above the threshold current I_{th} and below the saturation current I_s (as happens in RoF applications) it is possible to simplify relation 2.5 as follows:

$$\eta = \frac{P_0}{I_{bias} - I_{th}} \quad (2.6)$$

Let's consider now the generic RF signal $s(t)$ defined as:

$$\begin{aligned} s(t) &= I(t) \cos(\omega_{RF}t) + Q(t) \sin(\omega_{RF}t) \\ &= \sqrt{I^2(t) + Q^2(t)} \cos \left[\omega_{RF}t - \tan^{-1} \left(\frac{Q(t)}{I(t)} \right) \right] \end{aligned} \quad (2.7)$$

in which ω_{RF} is the RF carrier frequency and $I(t)$, $Q(t)$ are the in-phase and quadrature baseband components, respectively. Modulating now the laser with the RF signal $s(t)$ around the chosen biasing point, the expression of the electrical field reads as:

$$\bar{E}_L = E_0 \sum_{k=1}^{N_W} c_k \bar{e}_k \sqrt{1 + m_I s(t)} e^{j\omega_{0,k}t} \quad (2.8)$$

in which the Optical Modulation Index (OMI) m_I is defined as:

$$m_I = \frac{\eta_{RF}(\omega_{RF}) \max(|s(t)|)}{P_0} \quad (2.9)$$

where η_{RF} is the efficiency of the laser as function of the modulating frequency. Equation 2.8 represents the modulation expression of the intensity modulation of the laser.

However, equation 2.8 does not take into account a typical phenomenon which is present under the condition of direct modulation, the frequency chirping. This phenomenon will be presented in next Section.

Note that in the following discussion the analysis will be performed for the case of a simple sinusoidal wave, so that

$$s(t) = I_{in,RF} \cos(\omega_{RF}t) \quad (2.10)$$

This expression can be used as example to understand clearly the different phenomena involved in the propagation at 850 nm in SSMF without any loss of generality.

Frequency chirping

One of the main effects produced by the laser direct intensity modulation is the generation of spurious frequency modulation called *frequency chirping*. This phenomenon is generally detrimental for the performances of a telecommunication system. Firstly, the modulated spectrum of the laser is broadened, reducing its effectiveness in optical fiber communications. Moreover, the combined effect of frequency chirping and fiber chromatic dispersion can be source of distortion increasing the non-linearity of the system in long-haul RoF links based, for example, in 1550 nm DFB and SSMF where the dispersion coefficient is not zero [6]. Physically, the frequency chirping is due to the fact that the direct current modulation results in a variation of the refractive index of the active region and, as a consequence, the optical length of the cavity is changed as well. This causes the longitudinal resonant mode to shift back and forth in frequency due to relation (1.7) and produces the emission frequency $\omega_0 + \Delta\omega(t)$. The expression of $\Delta\omega(t)$ assumes the following form [83]:

$$\Delta\omega(t) = \frac{\alpha}{2} \left(\frac{d\ln[S(t)]}{dt} + \frac{\kappa_s S(t)}{\tau_{ph}} - \frac{R_{sp} K_{tot}}{S(t)} \right) \quad (2.11)$$

in which α is the linewidth enhancement factor (or Henry-factor) [84], $S(t)$ is the number of photons in the cavity, τ_{ph} is the photon lifetime, κ_s is the non linear gain coefficient, R_{sp} is the spontaneous emission rate and K_{tot} is the enhancement factor of spontaneous emission rate. Equation (2.11) can be expressed in a more practical form, considering $\Delta\omega(t)$ as function of the optical emitted power $P(t)$, exploiting the so-called Koch-Bowers formula [85]:

$$\Delta\omega(t) = \frac{\alpha}{2} \left(\frac{1}{P(t)} \cdot \frac{dP(t)}{dt} + \kappa P(t) \right) \quad (2.12)$$

in which κ is the so-called adiabatic chirp scaling factor [86], which is directly related to the non linear gain coefficient of the laser κ_s . From Equation 2.12 it is possible to identify two different contributions. One is proportional to the time derivative of the optical power and for this reason is called *transient*, while the other one, proportional to the optical power, is called *adiabatic*. The reason of this last name lies in the fact that thermal effects are not considered.

In fact, the total chirp contribution is also composed of thermal effects, still produced by the current modulation, and they are responsible for changing the cavity refractive index as well. This effect is however slow, and is considered negligible for modulating frequencies above few MHz in semiconductor lasers [1].

From (2.12), considering $P(t) = P_0[1 + m_I \cos(\omega_{RF}t)]$, through simple derivations, it is possible to obtain [87, 88]:

$$\Delta\theta(t) = M \sin(\omega_{RF}t + \psi) \quad (2.13)$$

where M represents the maximum optical phase shift [89], while ψ is the phase difference between intensity and frequency modulation. The expressions of these two quantities are given by [90]:

$$M = \frac{\alpha m_I}{2} \sqrt{1 + \left(\frac{\omega_c}{\omega_{RF}}\right)^2} \quad (2.14)$$

$$\psi = \tan^{-1}\left(\frac{\omega_{RF}}{\omega_c}\right) \quad (2.15)$$

in which $\omega_c = \kappa P_0$ is a frequency value related to the non linear gain of the laser [86, 90]. After these considerations, the final expression of the laser output electrical field is the following:

$$\bar{E}_L = E_0 \sum_{k=1}^{N_W} c_k \sqrt{1 + m_I \cos(\omega_{RF}t)} e^{j[\omega_{0,k}t + M_k \sin(\omega_{RF}t + \psi_k)]} \bar{e}_k \quad (2.16)$$

Equation (2.16) represents the IM-FM modulated signal which is emitted by the laser. The knowledge of such parameter is important in the design phase of IM-DD A-RoF systems in order to understand the limitation of the system.

2.2 Electrical field propagation

Initial assumptions and objectives

Before starting with the description of the electrical field propagation in SSMF some assumptions and considerations have to be made. From Figure 1.11 it is possible to assume two propagating modes at 850 nm, namely the first (LP_{01}) and the second mode (LP_{11}), since the third one (LP_{21}), when present, is just above cutoff.

The objective of the model is then to give a physical explanation of the behavior of the RF gain G in this particular situation of below cut-off propagation of SSMF. This will be described both in frequency and time domain, in which for last case the mean value μ_G and the variance σ_G^2 are considered in order to evaluate the important time fluctuations generated by the presence of the two modes. This effect is called modal noise [91] and happens generally in MMF when a coherent light propagates within. However, contrary to the case of MMF, the multi-mode propagation of SSMF at 850 nm is not mitigated by the exploitation of graded-index profile producing a “stronger” multi-mode propagation.

Regarding the laser behavior, the emitting lines N_W of the VCSEL are considered independent each other omitting the mutual exchange power effect called mode partition noise. This is justified by the fact that the mode partition noise among the different lines of the VCSEL emission spectrum is typically negligible with respect to other important fluctuations generated by other effects such as modal noise [92, 93].

The gain variance σ_G^2 will then be computed as a weighted sum of the variances corresponding to each line [94], which will be assumed equal ($\sigma_{G,k}^2 = \sigma_{G,line}^2$, $k = 1, \dots, N_W$), according to:

$$\sigma_G^2 = \sum_{k=1}^{N_W} p_k^2 \sigma_{G,k}^2 = \sigma_{G,line}^2 \sum_{k=1}^{N_W} p_k^2 \quad (2.17)$$

The average value of G will instead coincide with the average RF gain computed considering each line separately:

$$\langle G \rangle_k = \left\langle 10 \log_{10} \left[\frac{p_k^2 P_{RF,out}}{p_k^2 P_{RF,in}} \right] \right\rangle = \langle G \rangle \quad k = 1, \dots, N_W \quad (2.18)$$

where $\langle (\cdot) \rangle$ means that a time average of the quantity (\cdot) is computed.

Moreover, given the value of chromatic dispersion of the SSMF around $-90 \text{ ps}\cdot\text{nm}^{-1}\cdot\text{Km}^{-1}$ (see Figure 1.10), the mutual delays of spectral lines are more than two orders of magnitude smaller than the mutual delays between the LP_{01} and LP_{11} modes which are typically between $2 - 3 \text{ ps/m}$ [36].

To determine the expression of $\sigma_{G,line}$ it is necessary to start from the expression of the field at the output section of the SSMF strand with length L due to the generic line of the spectrum emitted by the VCSEL, which can be written as:

$$\bar{E}(t, L) = E_0 \sum_{i=1}^{N_m} A_i \bar{e}_i \sqrt{1 + m_I \cos[\omega_{RF}(t - \tilde{\tau}_i L)]} \cdot e^{j(\omega_0 t - \beta_i(t)L - M \sin[\omega_{RF}(t - \tilde{\tau}_i L) + \psi])} \quad (2.19)$$

where $\bar{e}_i(x, y)$ is the normalized field of the i -th fiber mode, A_i its amplitude (assumed real), which depends on the excitation field considered, while $\beta_i(t)$ is its phase constant. The quantity $\beta_i(t)$ is assumed as time-varying, due to changes in environmental quantities, like temperature or mechanical stress. The group delay per unit length of the i -th fiber mode is indicated as $\tilde{\tau}_i$. Indeed, all the quantities listed above are different for the different lines of the VCSEL emission spectrum. For the k -th line it should consequently be necessary to write respectively $\bar{e}_{i,k}(x, y)$, $A_{i,k}$, $\beta_{i,k}(t)$, $\tilde{\tau}_{i,k}$. However, as shown above, the expressions of G and σ_G can be determined from the computation of the correspondent quantities referred to a generic single line. Once the line is chosen, it will then be the only one considered in the derivation. The subscript k can then be omitted for the sake of formal simplicity.

Note also that the LP_{01} and the LP_{11} fiber modes are constituted respectively by a group of two and a group of four Rigorously Computed Fiber Modes (RCFM). The first group of RCFM contains the HE_{11} in its two polarizations, while the second one contains the TE_{01} and TM_{01} plus the HE_{21} in its two polarizations.

In (2.19), a complete coupling is assumed within the two mode groups, while the coupling between them is assumed to be negligible [95]. This hypothesis is justified by the fact that the environmental perturbations consist in temperature variations slower than 1 K/min and the lengths adopted are in the order of hundred of meters for the SSMF span. This last hypothesis allows also to neglect the attenuation coefficient from (2.19).

Computation of the output RF current and evaluation of its behavior

The detected current is proportional to the optical power received on the PD surface S_{PD} through the constant $\frac{\mathcal{R}}{2Z}$, in which \mathcal{R} is the responsivity of the photodiode and Z is the load impedance. It is then:

$$i_{out}(t) = \frac{\mathcal{R}}{2Z} \int_{S_{PD}} |\bar{E}(t, L)|^2 dS \quad (2.20)$$

Computing the integral at the second side of (2.20), the expression of the output current becomes:

$$\begin{aligned} i_{out}(t) = & I_0 \sum_{i=1}^{N_m} A_i^2 b_{ii} \cdot (1 + m_I \cos(\omega_{RF}(t - \tau_i)) \\ & + 2A_1 A_2 b_{12} \cdot [1 + m_I \cos(\omega_{RF} \Delta \tau) \cos(\omega_{RF}(t - \bar{\tau})] \\ & \cdot \left[\cos(\Delta \beta(t)) \cos(x \cos(\omega_{RF}(t - \bar{\tau}) + \psi)) + \sin(\Delta \beta(t)) \sin(x \cos(\omega_{RF}(t - \bar{\tau}) + \psi)) \right] \end{aligned} \quad (2.21)$$

where for sake of simplicity it has been put $\tau_i = \check{\tau}_i L$, and the following parameters are defined:

$$I_0 = \frac{\mathcal{R} E_0^2}{2Z} \quad (2.22)$$

$$b_{ij} = \int_{S_{PD}} \bar{e}_i \cdot \bar{e}_j^* dS \quad i, j = 1, 2 \quad (2.23)$$

$$\Delta \beta(t) = \beta_2(t) - \beta_1(t) \quad (2.24)$$

$$\Delta \tau = \frac{(\tau_1 - \tau_2)}{2} \quad (2.25)$$

$$x = 2M \sin(2\pi f_{RF} \Delta \tau) \quad (2.26)$$

$$\bar{\tau} = \frac{(\tau_1 + \tau_2)}{2} \quad (2.27)$$

With reference to the last term within square brackets at the second side of (2.21), the Jacobi-Anger expansion [96] has been exploited, i.e.:

$$e^{ju \cos(v)} = \sum_{n=-\infty}^{+\infty} j^n J_n(u) e^{jnv} \quad (2.28)$$

where $J_n(u)$ is the Bessel function of first kind and order n . In case of Equation 2.21 it is $u = x$ and $v = \cos(2\pi f_{RF}(t - \bar{\tau}))$. Considering now only the RF component at ω_{RF} of

$i_{out}(t, L)$, it is possible to write the following expression:

$$\begin{aligned} i_{out,RF}(t) &= I_0 \{ [\mathcal{A}_c + \mathcal{B}_c(t)] \cos(\omega_{RF}t) + [\mathcal{A}_s + \mathcal{B}_s(t)] \sin(\omega_{RF}t) \} = \\ &= \Re\{\tilde{I}_{out,RF}(t)e^{j\omega_{RF}t}\} \end{aligned} \quad (2.29)$$

where

$$\tilde{I}_{out,RF}(t) = I_0 \{ [\mathcal{A}_c + \mathcal{B}_c(t)] - j[\mathcal{A}_s + \mathcal{B}_s(t)] \} \quad (2.30)$$

is the complex envelope of the received RF signal, where

$$\mathcal{A}_c = \sum_{i=1}^{N_m} m_I A_i^2 b_{ii} \cos(2\pi f_{RF} \tau_i) \quad (2.31)$$

$$\mathcal{A}_s = \sum_{i=1}^{N_m} m_I A_i^2 b_{ii} \sin(2\pi f_{RF} \tau_i) \quad (2.32)$$

are the time-independent parts, and

$$\mathcal{B}_c(t) = 2A_1 A_2 b_{12} \mathcal{C}_c(t) \quad (2.33)$$

$$\mathcal{B}_s(t) = 2A_1 A_2 b_{12} \mathcal{C}_s(t) \quad (2.34)$$

are the time dependent parts of the envelope, in which \mathcal{C}_c and \mathcal{C}_s are defined as follows:

$$\begin{aligned} \mathcal{C}_c(t) &= m_I \cos(\omega_{RF} \Delta\tau) J_0(x) \cos(\Delta\beta(t)L) \cos(\omega_{RF} \bar{\tau}) \\ &\quad + 2J_1(x) \sin(\Delta\beta(t)L) \cos(\omega_{RF} \bar{\tau} + \psi) \end{aligned} \quad (2.35)$$

$$\begin{aligned} \mathcal{C}_s(t) &= m_I \cos(\omega_{RF} \Delta\tau) J_0(x) \cos(\Delta\beta(t)L) \sin(\omega_{RF} \bar{\tau}) \\ &\quad + 2J_1(x) \sin(\Delta\beta(t)L) \sin(\omega_{RF} \bar{\tau} + \psi) \end{aligned} \quad (2.36)$$

in which the dependence on $\Delta\beta(t)$ has been put in evidence.

It can be noted that, due to the orthogonality of the SSMF modes, in case of a photodiode with infinite surface S_{PD} it should be $b_{11}, b_{22} = 1$ and $b_{12} = 0$. However, $b_{12} \neq 0$ has to be taken into account because of the finite dimensions of a realistic photodiode and possible misalignments [97]. The quantities $\mathcal{B}_c(t)$ and $\mathcal{B}_s(t)$ given by (2.33) and (2.34) represent the time dependent contributions due to the temperature fluctuations, while \mathcal{A}_c and \mathcal{A}_s remain constant over time. The envelope of $i_{out,RF}(t)$ is given by

$$|\tilde{I}_{out,RF}(t)| = I_0 \sqrt{[\mathcal{A}_c + \mathcal{B}_c(t)]^2 + [\mathcal{A}_s + \mathcal{B}_s(t)]^2} \quad (2.37)$$

Since the time dependent terms have zero mean, the magnitude of the mean of the RF current received can be written considering equation (2.30) as follows:

$$\mu_{RF} = \left| \left\langle \tilde{I}_{out,RF}(t) \right\rangle \right| = I_0 \sqrt{\mathcal{A}_c^2 + \mathcal{A}_s^2} \quad (2.38)$$

The link RF gain G and its average value $\langle G \rangle$ assume respectively the form:

$$G = 10 \log_{10} \left[\frac{|\tilde{I}_{out,RF}(t)|^2}{|I_{0in,RF}|^2} \right] \quad (2.39)$$

$$\langle G \rangle = 10 \log_{10} \left[\frac{\mu_{RF}^2}{|I_{0in,RF}|^2} \right] \quad (2.40)$$

and the resulting expression of $\sigma_{G,line}$ is therefore given by:

$$\sigma_{G,line} = \sqrt{\left\langle \left\{ 10 \log_{10} \left[\frac{|\tilde{I}_{out,RF}(t)|^2}{\mu_{RF}^2} \right] \right\}^2 \right\rangle} \quad (2.41)$$

The expression given by (2.41) can be always used. When the following relation holds:

$$\begin{aligned} |\tilde{I}_{out,RF}(t)| &\simeq I_0 \left[\sqrt{\mathcal{A}_c^2 + \mathcal{A}_s^2} + \frac{\mathcal{A}_c}{\sqrt{\mathcal{A}_c^2 + \mathcal{A}_s^2}} \mathcal{B}_c(t) + \frac{\mathcal{A}_s}{\sqrt{\mathcal{A}_c^2 + \mathcal{A}_s^2}} \mathcal{B}_s(t) \right] = \\ &= \mu_{RF} + \Delta I_{out,RF}(t) \end{aligned} \quad (2.42)$$

an easier expression can be written for $\sigma_{G,line}$. Indeed, exploiting the relationship $20 \log_{10}(1+y) \simeq \frac{20}{\log_e(10)} y$, for $y \ll 1$, it becomes:

$$\sigma_{G,line} \simeq \frac{20}{\log_e(10)} \frac{\sqrt{\langle \Delta I_{out,RF}^2 \rangle}}{\mu_{RF}} = \frac{20}{\log_e(10)} \frac{\sigma_{RF}}{\mu_{RF}} \quad (2.43)$$

with σ_{RF} representing the standard deviation of $|\tilde{I}_{out,RF}|$. When the condition given by (2.42) is not valid, it is necessary to compute $\sigma_{G,line}$ through (2.41). This happens for example if the LP_{01} and the LP_{11} fiber modes have almost the same weight and the frequency considered is such that $2\pi f_{RF} \Delta\tau$ is an odd integer of $\pi/2$, in which case μ_{RF} tends to zero. Equation (2.43) is anyway useful because it allows to qualitatively describe some behaviors of $\sigma_{G,line}$.

Indeed, in the vicinity of the frequencies mentioned above, μ_{RF} , which is at the denominator, diminishes its value. At the same time, it can be observed that σ_{RF} , which is at the numerator, depends (see (2.43) and (2.42)) on the standard deviation of the terms $\mathcal{B}_c(t)$ and $\mathcal{B}_s(t)$, which in turn (see (2.33) and (2.34)) depend on the standard deviation of the terms $\mathcal{C}_c(t)$ and $\mathcal{C}_s(t)$ given by (2.35) and (2.36). Both the expressions of (2.35) and (2.36) are composed by the sum of two addends. The first depends on $\cos(2\pi f_{RF} \Delta\tau)$ and tends to zero when the frequency f_{RF} is such that $2\pi f_{RF} \Delta\tau$ tends to be an odd integer of $\pi/2$. The second addend is proportional to $J_1(x)$, where x , given by (2.26), is instead proportional to $\sin(2\pi f_{RF} \Delta\tau)$ and tends to a maximum for the same frequencies. The values assumed by x allow typically to approximate $J_1(x) \sim x/2$, and therefore it can be expected that $\sigma_{G,line}$ due to modal noise exhibits high values in the vicinity of the frequencies f_{RF} where μ_{RF} tends to a minimum.

Experimental measurements and validation of the model

The model described in previous Section put in evidence two main effects related to the multimode propagation that have to be considered for the realization of RoF links based on SSMF below cut-off wavelengths. To validate the model the experimental setup shown in Figure 2.1 has been employed.

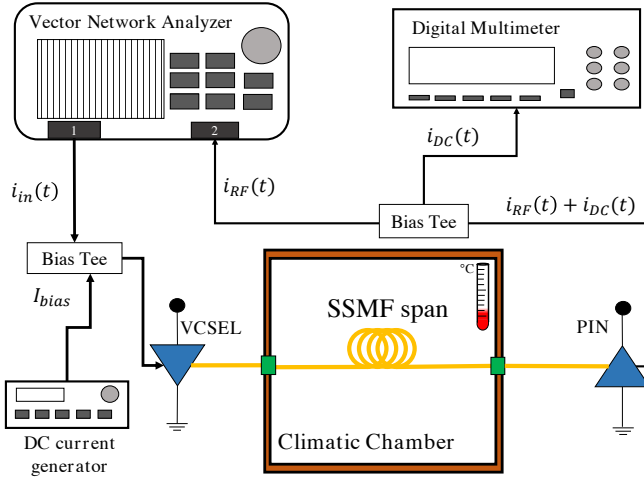


Figure 2.1: Functional scheme of the experimental setup.

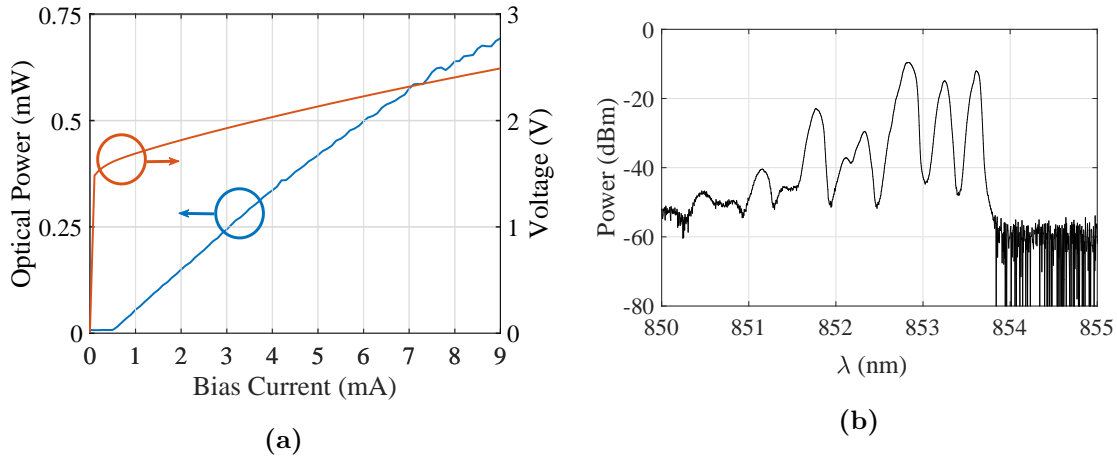


Figure 2.2: LIV characteristic (a) and optical spectrum at 4 mA (b) of the MTM VCSEL employed.

In particular, a directly modulated 10 Gbps VCSEL (Optowell TP85-LCP1H) emitted the optical signal into a channel constituted by a SSMF strand. The optical receiver was constituted by a PIN PD (Optowell RP85-LCT0N) followed by a RF matching circuit. A Vector Network Analyzer (VNA) was then used to generate and receive different radio frequencies through port 1 and port 2, respectively. To emulate possible conditions causing modal noise, a temperature stress was produced with a climatic chamber. This was done by

Parameter	Symbol	Value
Threshold current	I_{th}	0.8 mA
Bias current	I_{bias}	4 mA
Slope-efficiency DC	η	0.1 mW/mA
Slope-efficiency RF	η_{RF}	0.1 mW/mA
OMI	m_i	0.35
Linewidth enhancement factor	α	2
Adiabatic chirp frequency	f_c	300 MHz
Line emission weight	$p_1 \simeq p_2$	1/2
Number of emission lines	N_W	2
PIN Responsivity	\mathcal{R}	1 mA/mW
Intermodal delay-over-meter	$\tau_2 - \tau_1$	2.3 ps/m

Table 2.1: System parameters employed in the model.

the insertion of the G.652 strand inside a climatic chamber, controlled and monitored by a Resistor Temperature Detector (RTD) sensor connected to a digital data acquisition block (see again Fig. 2.1). Using the VNA, the measurement of the behavior of G versus time due to temperature variations was performed in a time span of few hours, with a sampling time of 6 seconds. The quantities $\langle G \rangle$ and σ_G could be determined from the values of $G(t)$.

Table 2.1 lists the values of the electrical and optical quantities of the modeled system, which are the characteristics of the real system on which the experimental activity was subsequently performed. In particular, the MTM VCSEL utilized was biased at 4 mA and its spectrum presents two lines of approximately the same weight which prevail over the others by at least 6 dB (see LIV and spectrum curve of Figure 2.2). For this reason it is possible to consider the following relation:

$$\sigma_G \simeq \frac{1}{\sqrt{2}} \sigma_{G,line} \quad (2.44)$$

The analysis has been performed on the characteristics of a link with SSMF strand length $L_{SSMF} = 300$ m.

Intermodal dispersion

The first effect is related to the bandwidth of the RoF link. In particular a drastic reduction of the 3dB frequency response is present. To better understand the phenomenon it is possible to consider the terms $B_c(t) = B_s(t) = 0$, which means neglecting the fluctuations of $\Delta\beta(t)$ and therefore any temperature variation. The expression of the RF current becomes the same as μ_{RF} in Eq. (2.38):

$$|\tilde{I}_{out,RF}| = I_0 \sqrt{\mathcal{A}_c^2 + \mathcal{A}_s^2} \quad (2.45)$$

which in case of two modes can be expanded as follows:

$$|\tilde{I}_{out,RF}| = I_0 \left[(A_1^2 b_{11} \cos(\omega_{RF} \tau_1) + A_2^2 b_{22} \cos(\omega_{RF} \tau_2))^2 + (A_1^2 b_{11} \sin(\omega_{RF} \tau_1) + A_2^2 b_{22} \sin(\omega_{RF} \tau_2))^2 \right]^{1/2} \quad (2.46)$$

To better investigate the behavior of the channel due to intermodal dispersion the case of $b_{11} = b_{22} = 1$ and $A_1 = A_2 = A$ can be considered, leading to a simplification of Equation (2.46) in the following expression:

$$|\tilde{I}_{out,RF}| = I_0 A^2 \sqrt{2 + 2 \cos(2\omega_{RF} \Delta\tau)} = I_0 A^2 \cos(\omega_{RF} \Delta\tau) \quad (2.47)$$

From this expression it is possible to understand that the fiber transfer function will be subjected to a periodicity which depends on the term $2\pi f_{RF} \Delta\tau$. Recalling the definition $\tau = \check{\tau}L$, a trade-off of between frequency and length appears. When the length of the fiber is fixed the k -th minimum $f_{RF, \min, k}$ is given by:

$$f_{RF, \min, k} = \frac{2(k+1)}{2\Delta\check{\tau}L} \quad (2.48)$$

while if f_{RF} is fixed the k -th minimum $L_{\min, k}$ becomes:

$$L_{\min, k} = \frac{2(k+1)}{2\Delta\check{\tau}L} \quad (2.49)$$

From the frequency bandwidth measurement using a fixed fiber length is then possible to estimate $\Delta\check{\tau}$. An example of intermodal dispersion effect on the RF response is shown in Figure 2.3 for 300 meters of length employing and 850 nm VCSEL source.

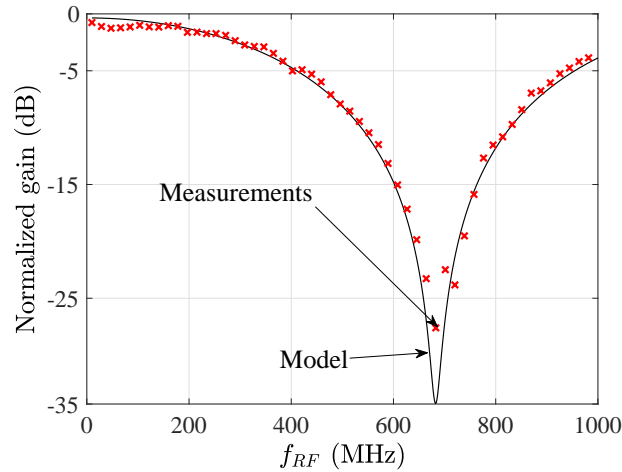


Figure 2.3: Example of intermodal dispersion in 300 meters of SSMF at 850 nm on the RF gain (normalized in this case to the characteristics measured for $L = 1$ m).

Modal noise

The second effect produced by the multi-mode behavior within SSMF at 850 nm is called *modal noise*. As mentioned above, modal noise results in slow fluctuations of the optical received power which have important consequence on the modulating signal as well. The fluctuations of the RF envelope $|\tilde{I}_{out,RF}|$ are related in this case to the quantities $\mathcal{B}_c(t)$ and $\mathcal{B}_s(t)$ in the Equations (2.37) and (2.30) which are directly dependent on the quantity $\Delta\beta(t)$. An example of behavior of σ_G is shown in Figure 2.4, in which the model described has been used to fit the measurements. From this Figure, it is possible to see also the combined effect of intermodal dispersion and modal noise given by the fact that the detrimental effect produced in the bandwidth results to be detrimental as well for σ_G in the same frequencies interval, which is therefore not optimum for transmission.

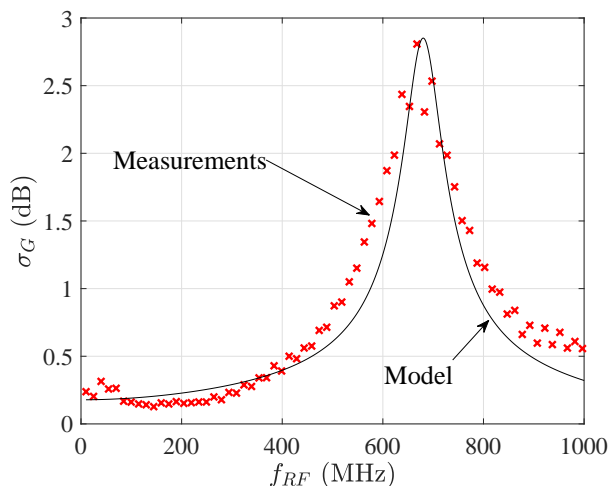


Figure 2.4: Example of modal noise in terms of σ_G for 300 meters of SSMF at 850 nm.

The fluctuation of the constant phase difference $\Delta\beta(t)$ is related to mechanical or temperature stress together with possible imperfections or non-ideal situations which make the two modes lose they orthogonality. An example can be the finite surface area of the photodetector but also the connectors misalignment between two fibers (as it will be shown in next Sections).

Indeed, to be able to interfere, the modes should be coherent each other, which means that the delay difference between the modes should be lower than the coherence time of the source. The lower the coherence of the source, the lower the effect of modal noise, which for sufficient long distances disappears. In the case considered, it is $\Delta\tilde{\tau} \simeq 2.3$ ps/m for the fiber modes. Typical values of coherence bandwidth of MTM VCSEL and SM VCSEL are respectively around 200 MHz [38] and 20 MHz [48], respectively. Those values give a coherence time of $\tau_{coh} \simeq 5$ ns for SM and $\tau_{coh} \simeq 50$ ns. Therefore the length L_{uncoh} for which the propagation in the SSMF is not coherent anymore is given by $L_{uncoh} = \tau_{coh}/\Delta\tilde{\tau}$ [98], which is around 2 Km for MTM VCSEL and 20 Km for SM VCSEL.

An image of output pattern form a multimode fiber excited by coherent and incoherent source is shown in Figure 2.5.

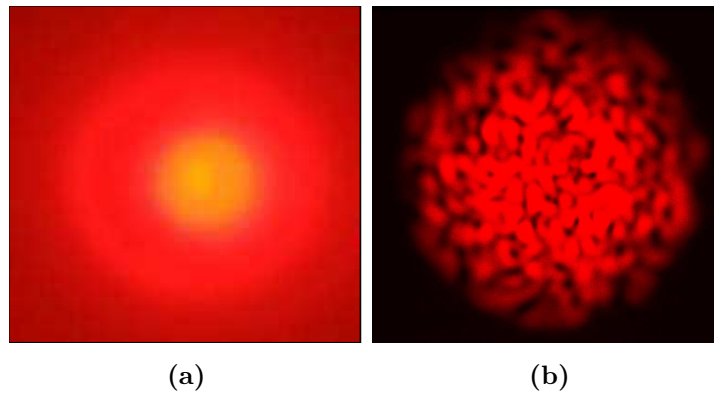


Figure 2.5: Output pattern of MMF excited by a LED (a) and by a MTM VCSEL (b) [91].

2.3 Investigation of possible solutions to mitigate modal noise and intermodal dispersion

In this Section two different techniques to mitigate the effect of multimode propagation in SSMF at 850 nm are presented. Both techniques are related to the possible suppression or attenuation of the higher order mode, trying to reach a quasi-single mode propagation.

Post-Filtering

A first possible solution to mitigate the presence of modal noise and modal dispersion is to place a mode filter right before the photo-detector (see Figure 2.6).

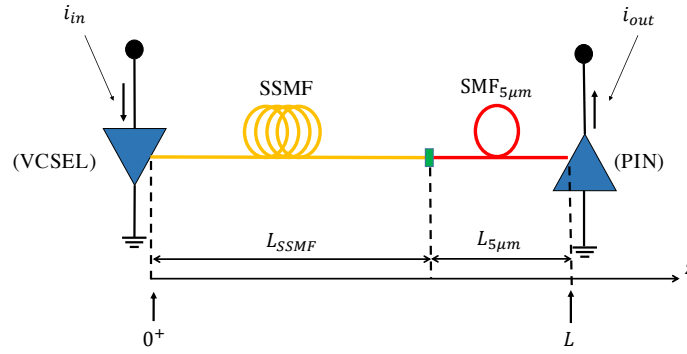


Figure 2.6: Post-filtering setup.

In the following description, the mode filter considered is a 3 meter optical fiber with a core diameter of around $5 \mu\text{m}$ and having cut-off wavelength of 780 nm provided by Thorlabs[®] which operate in single mode regime at 850 nm. This fiber will be called in the following as “SMF_{5μm}” and all the quantities related to it are differentiated with the sub-index 5μm. With reference to Eq. (2.19) the field $\bar{E}(t, L)$, in which $L = L_{SSMF} + L_{5\mu\text{m}}$ in such link is expressed by:

$$\begin{aligned} \bar{E}(t, L) = & \bar{e}_{5\mu\text{m}} e^{j(\omega_0 t - \beta_{5\mu\text{m}} L_{5\mu\text{m}})} \sum_{i=1}^{N_m} A_i a_i e^{-j[\beta_i(t) L_{SSMF}]} \\ & \cdot \sqrt{1 + m_I \cos[\omega_{RF}(t - \tau_i - \tau_{5\mu\text{m}})]} e^{-jM \sin[\omega_{RF}(t - \tau_i - \tau_{5\mu\text{m}}) + \psi]} \end{aligned} \quad (2.50)$$

in which the quantity $\bar{e}_{5\mu\text{m}}$ and $\tau_{5\mu\text{m}}$ represent the normalized mode vector and the fundamental mode group delay of the SMF_{5μm}, and

$$a_i = \int_{S_{5\mu\text{m}}} \bar{e}_i \cdot \bar{e}_{5\mu\text{m}}^* dS \quad (2.51)$$

where $S_{5\mu\text{m}}$ is the cross section of the SMF_{5μm} fiber, represents the overlap integral between the i -th mode of the SSMF and the LP₀₁ mode of the SMF_{5μm}. Note that due to the shapes of the fields of the fiber modes considered, in case of ideal connection it should be $a_1 \neq 0$

and $a_2 = 0$. However, due to imperfections in the connection, for example the presence of connector misalignments, a value $a_2 \neq 0$ has to be taken into account.

Proceeding in same computations as previous section the output current $i_{out,5\mu m}$ can be written as

$$\begin{aligned}
 i_{out,5\mu m}(t) = & I_0 \sum_{i=1}^{N_m} A_i^2 a_i^2 b_{5\mu m} \cdot (1 + m_I \cos(\omega_{RF}(t - \tau_i - \tau_{5\mu m}))) \\
 & + 2A_1 A_2 a_1 a_2 b_{5\mu m} [1 + m_I \cos(\omega_{RF} \Delta \tau) \cos(\omega_{RF}(t - \bar{\tau})] \\
 & \cdot \left[\cos(\Delta \beta(t)) \cos(x \cos(\omega_{RF}(t - \bar{\tau}) + \psi)) + \sin(\Delta \beta(t)) \sin(x \cos(\omega_{RF}(t - \bar{\tau}) + \psi)) \right]
 \end{aligned} \tag{2.52}$$

Note that, in case there $SMF_{5\mu m}$ is not present at the end of the SSMF span, the output current $i_{out}(t)$ assumes the same formal aspect as in (2.21). This let Eq. (2.52) have the same expression of the RF component as in Eq. (2.29) with the only difference being that in (2.31) and (2.32) the term b_{ii} must be replaced by $a_i^2 b_{5\mu m}$ and in (2.33) and (2.34) the term b_{12} must be replaced by $a_1 a_2 b_{5\mu m}$. The $SMF_{5\mu m}$ span, which exhibits a single mode behavior at $\lambda = 850$ nm, performs an output filtering operation. This solution has been shown to determine an increase of the passband with respect to the case where only a SSMF strand is utilized, leading to a BER reduction of digital optical links [38].

Fig. 2.7 reports modeled results which compare the performance of the optical link having the $SMF_{5\mu m}$ at the SSMF end section, to when only the SSMF is used (without $SMF_{5\mu m}$).

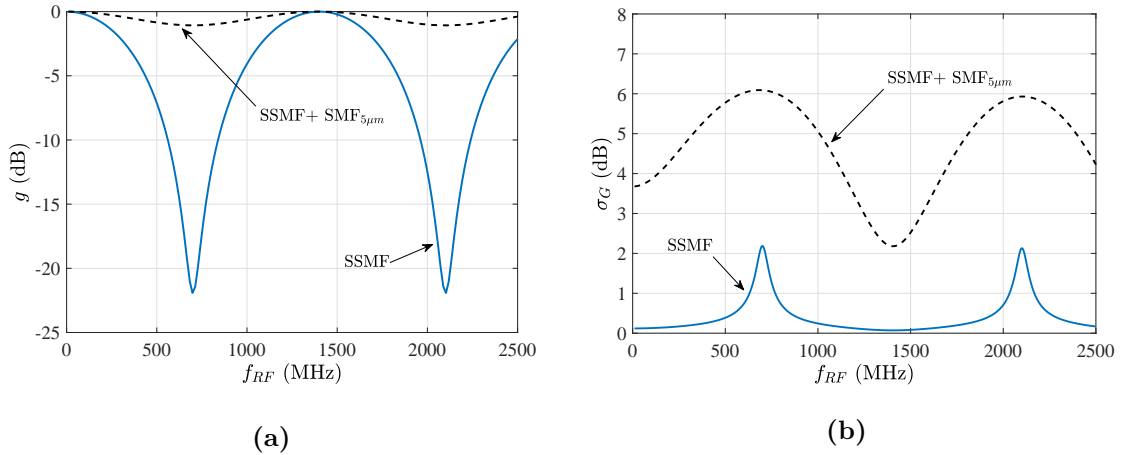


Figure 2.7: Comparison of simulated results for a transmission link with SSMF length $L = 300$ m in case of presence and in case of absence of $SMF_{5\mu m}$ patch between SSMF and PD. The bandwidth improvement due to the $SMF_{5\mu m}$ employment can be noticed in (a) while the increase of the standard deviation σ_G of the fluctuations of G due to modal noise is shown in (b). The parameters values utilized in the simulation program are: $m_I = 0.375$, $A_1^2 = 0.54$, $A_2^2 = 0.46$, $a_1^2 = 0.9$, $a_2^2 = 0.065$, $b_{11} = 0.985$, $b_{22} = 0.985$, $b_{12} = 0.015$.

The simulations confirm that the insertion of $SMF_{5\mu m}$ at the output section of the SSMF improves the available bandwidth. Figure 2.7a shows the behavior of the normalized gain

$g = \langle G \rangle - \langle G \rangle|_{max}$. It can be noticed that the difference Δg between the maximum and the minimum values of g is largely reduced by the introduction of the $SMF_{5\mu m}$ patch with respect to the case when only the SSMF is present.

It is however important to observe, that, as reported in Figure 2.7b, the model predicts an increase of the maximum value $\sigma_G|_{max}$ of σ_G with respect to the case of the SSMF span alone. Moreover, in the vicinity of $\sigma_G|_{max}$ an enlargement of the bandwidth where the values of σ_G are relatively high results in the case when the $SMF_{5\mu m}$ is present.

Pre-Filtering

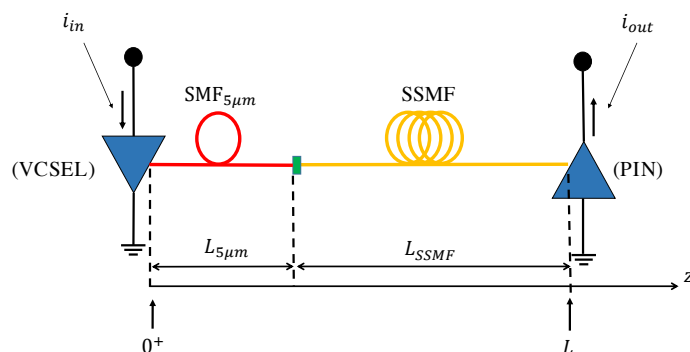


Figure 2.8: Pre-filtering setup.

The expression of $\sigma_{G,line}$ given by (2.43), where μ_{RF} is present at denominator, suggests that a reduction of the amplitude A_2 of the LP_{11} fiber mode would diminish the impact of modal noise. In fact, reducing the degree of destructive interference at the detection stage, the presence of the minima of μ_{RF} is also reduced, mitigating the effect of modal noise.

From the practical point of view, this can be achieved on putting the $SMF_{5\mu m}$ patch before the SSMF strand acting as pre-filtering (see Figure 2.8).

Figure 2.9 shows the expected behavior of the transmission link in terms of g and σ_G when the value of A_2 is gradually reduced with respect to A_1 . The transmission link features a SSMF length $L_{SSMF} = 300$ m and a $SMF_{5\mu m}$ patch between SSMF and PD, and all the other parameters are the same as in Fig. 2.7. In Figure 2.9a positive effects are observed in the behavior of g , since the value of Δg decreases when A_2 is reduced with respect to A_1 .

In addition to this, Figure 2.9b suggests that important reductions of σ_G can be expected when the relative weight of the LP_{11} fiber mode is reduced with respect to the LP_{01} .

In this way we expect that the large reduction of A_2 leads to a low impact of the terms related to modal noise given by (2.33) and by (2.34), in which case the quantity b_{12} is expectedly small.

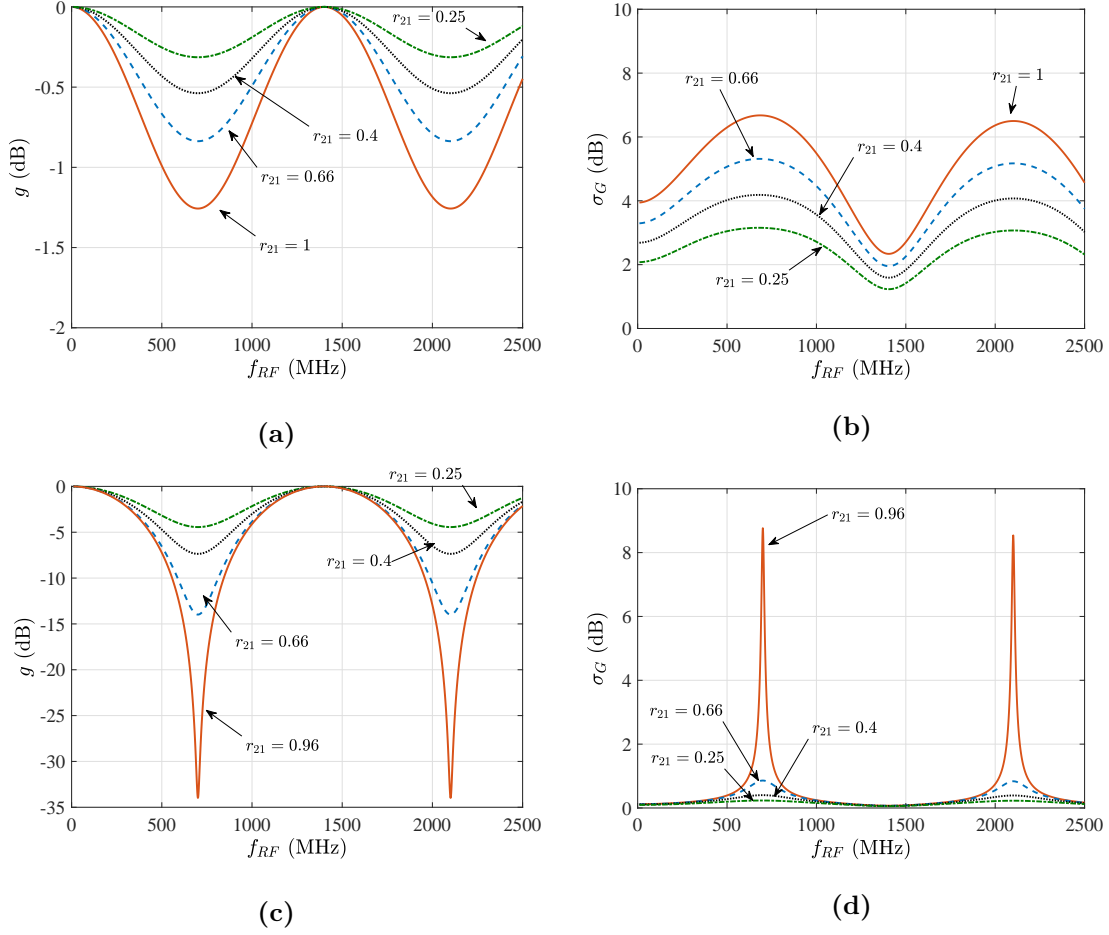


Figure 2.9: Behavior of g (a) and σ_G (b) as a function of the RF modulating frequency as function of the parameter $r_{21} = (A_2/A_1)^2$. A reduction in both Δg and σ_G can be noticed due to the reduction of A_2 with respect to A_1 . The transmission link considered is the one with SSMF length $L_{SSMF} = 300$ m in case of presence of $SMF_{5\mu m}$ patch between SSMF and PD.

Experimental results of the two filtering techniques

Four configurations of the optical channel were considered to investigate the behavior of modal noise and take appropriate countermeasures. The first analysis regarded the effect of the insertion of an $SMF_{5\mu m}$ span between SSMF and PD. A passband increase can be observed in Fig. 2.10a, which compares the behaviors of g in the two cases, with reference to a SSMF strand of length $L_{SSMF} = 300$ m. The value of Δg has been measured to be about 6 dB in the frequency range $B = [10 \text{ MHz}, 2.5 \text{ GHz}]$, while the same quantity showed a much higher value of about 34 dB in the case when only the SSMF is used.

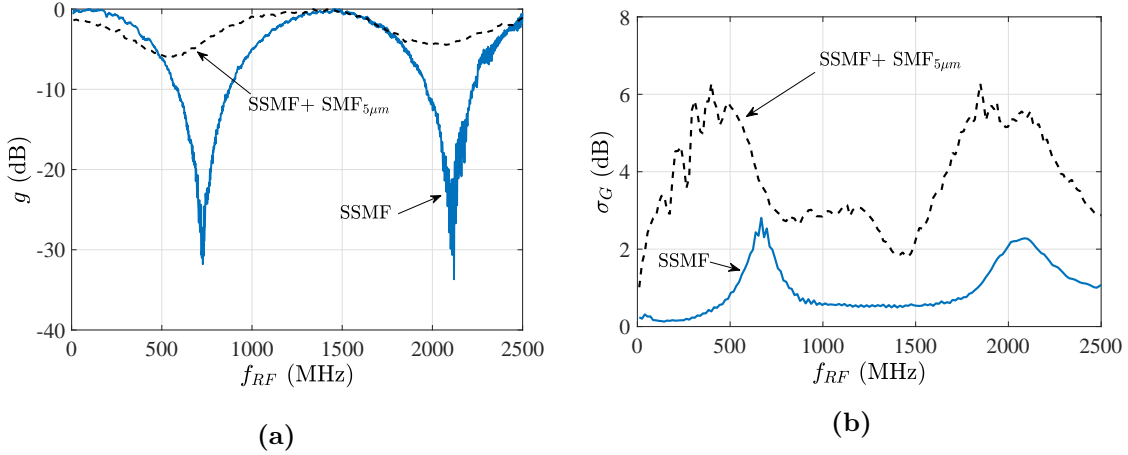


Figure 2.10: Behaviors of g (a) and σ_G (b) versus frequency of two VCSEL based transmission links utilizing 300 m of SSMF, respectively with and without $SMF_{5\mu m}$ at the end of the SSMF span. The curves reported in (b) coincide with the curves representing the standard deviation σ_{NF} of the noise figure NF of the links considered.

However, this solution also brings about an undesired increase of modal noise. Fig. 2.10b allows to observe the increase of σ_G , whose maximum value $\sigma_G|_{max}$ is about 6 dB, which is more than 3 dB larger than the case when only 300 m of SSMF was used. Note that, in agreement with the modeled results of the previous Section, in the vicinity of $\sigma_G|_{max}$ an enlargement of the bandwidth where the values of σ_G are relatively high is observed in the case when the $SMF_{5\mu m}$ is present, with respect to the case of the SSMF span alone.

Nevertheless, this configuration will be taken as the reference since it emulates the worst performance for VCSEL-based SSMF transmission link in terms of modal noise.

The presence of a truly singlemode fiber at 850 nm between VCSEL and SSMF propagates mostly the LP_{01} fiber mode. Hence a very low weight is assigned to the higher order mode. The effect of this solution can be noticed in Fig. 2.11.

An improvement in terms of the system bandwidth can be noticed in Fig. 2.11a, where it is $\Delta g \simeq 6$ dB in the system described in [38] (SSMF + $SMF_{5\mu m}$) whereas it is $\Delta g \simeq 1.6$ dB when an additional $SMF_{5\mu m}$ patch-cord is placed between the VCSEL and the SSMF strand ($SMF_{5\mu m} + \text{SSMF} + SMF_{5\mu m}$). In terms of 3 dB modulation bandwidth, computed taking as a reference $g(0)$, the improvement goes from $B_{3dB} \simeq 380$ MHz to $B_{3dB} \simeq 2500$ MHz.

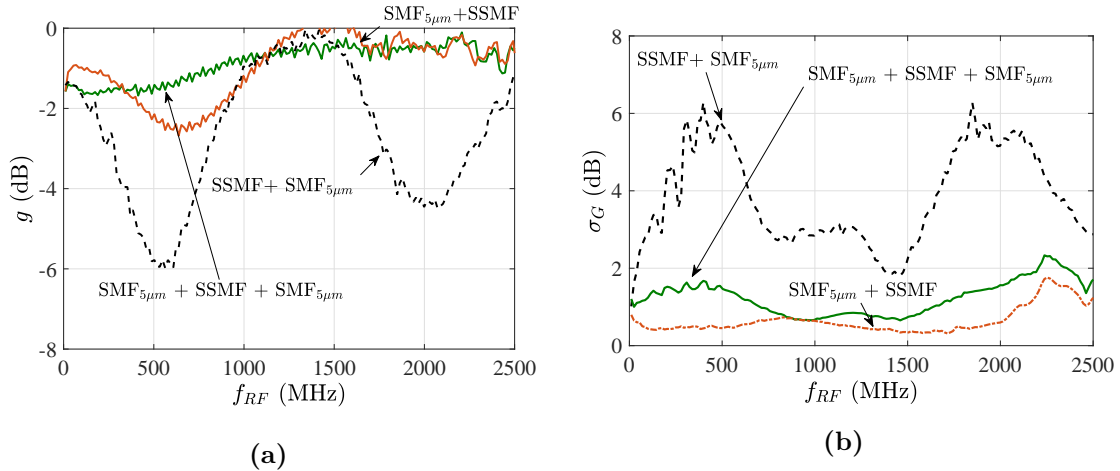


Figure 2.11: Behaviors of g (a) and σ_G (b) versus frequency of three VCSEL based transmission links utilizing 300 m of SSMF, respectively with a patchcord of $SMF_{5\mu m}$ at the beginning, at the end, and both at the beginning and at the end of the SSMF span. As in Fig. 2.10b, the curves reported in (b) are also representative of the standard deviation σ_{NF} of the noise figure NF of the links considered.

A noticeable improvement can additionally be observed in Fig. 2.11b, where $\sigma_G|_{max}$ is reduced to less than 2 dB within B . The performance of the structure $SSMF + SMF_{5\mu m}$ has then shown an important improvement with the introduction of the $SMF_{5\mu m}$ patch before the SSMF strand.

With the aim to consider a more realistic condition, in Fig. 2.11 it has also been reported the behavior of a VCSEL-based transmission link where the $SMF_{5\mu m}$ patch is placed before the SSMF strand of length $L_{SSMF} = 300$ m, and no other $SMF_{5\mu m}$ patch is placed after. This configuration shows indeed a slightly higher value of Δg ($\simeq 2$ dB) which anyway leads to the same $B_{3dB} = 2500$ MHz with respect to the case where the $SMF_{5\mu m}$ is placed before and after the SSMF strand. Moreover, $\sigma_G|_{max}$ is further reduced from $\simeq 2.1$ dB to $\simeq 1.8$ dB. Taking also into account the considerations on optical insertion losses specified below, this leads to the conclusion that the only introduction of the $SMF_{5\mu m}$ patch between VCSEL and SSMF gives the best performance in terms of B_{3dB} and $\sigma_G|_{max}$ of VCSEL-based SSMF transmission links. To give an idea of the power penalties caused by the introduction of the $SMF_{5\mu m}$ in the system, the behavior of $\langle G \rangle$ is reported in Fig. 2.12a.

The maximum additional RF loss introduced in the configuration where the $SMF_{5\mu m}$ patch is placed both between VCSEL and SSMF and between SSMF and PD can be quantified in about 15 dB, corresponding to 7.5 dB of optical insertion loss. On the contrary, in the case where only one $SMF_{5\mu m}$ patch is utilized (either between VCSEL and SSMF or between SSMF and PD) the two losses are 11-12 dB and 5.5-6 dB respectively.

From the values of $\langle G \rangle$ it is possible to evaluate the average $\langle NF \rangle$ of the noise figure NF in the different cases. This value represents a meaningful quantity in case the VCSEL-based link is utilized for the transmission of RF signals through the RoF technology.

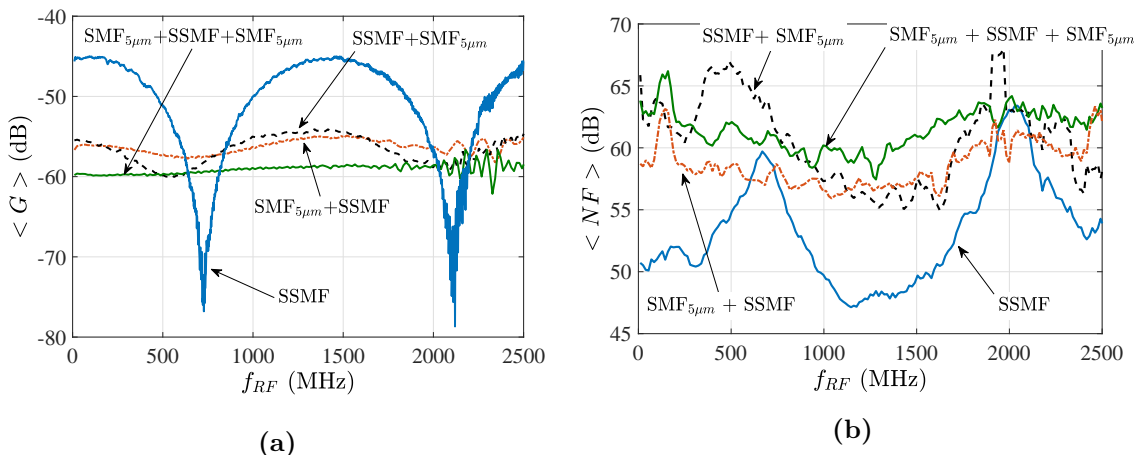


Figure 2.12: Behaviors of (a) the average RF gain $\langle G \rangle$ for $L_{SSMF} = 300m$ and (b) the noise figure NF , in the four configurations of VCSEL-based transmission links considered in the present work.

Exploiting the definition (see for example [99]) of NF for RoF links, it is $\langle NF \rangle|_{dB} = N_{out}|_{dB(W/Hz)} - \langle G \rangle|_{dB} - 10 \log_{10}(kT)|_{dB(W/Hz)}$, where N_{out} is the available noise output power per unit bandwidth of the system, while $k = 1.38 \cdot 10^{-23} J/K$ is the Boltzmann constant and $T = 300 K$ is the reference temperature. It can be noted that, due to the higher values of $\langle G \rangle$ presented by the configuration where only the SSMF is utilized, the values of $\langle NF \rangle$ are generally smaller than in the other configurations. However, the fluctuations of G due to modal noise cause in turn fluctuations of NF . This leads to standard deviations of the noise figure σ_{NF} represented by the same curves reported in Fig. 2.10b and Fig. 2.11b. From the observation of both figures, it can be concluded that the solution proposed here ($SMF_{5\mu m}$ patch followed by the SSMF span) is the only one which presents $\sigma_{NF} < 2 dB$ within the band B .

Keeping in mind applications in the fields of in-building wireless coverage as well as remote radio antennas used for astronomy, further experiments have been performed with shorter SSMFs. The obtained results can be observed in Fig. 2.13 which reports the behavior of $\sigma_G|_{max}$ within the bandwidth B when SSMF strands of the same optical fiber with different lengths are utilized.

Starting from the left-hand side, the four histograms report the measured values of $\sigma_G|_{max}$ for $L_{SSMF} = 30 m$, $70 m$, $100 m$ and $300 m$, respectively, for the four configurations. Proceeding to the right-hand side, the reduction of $\sigma_G|_{max}$ for all the values of L_{SSMF} can be observed, when the $SMF_{5\mu m}$ patch is introduced in this system between VCSEL and SSMF. The last two sets of the histograms allow to perform a similar comparison between the cases when the optical channel is constituted by the SSMF strand alone and the case when the $SMF_{5\mu m}$ patch is introduced between the VCSEL and the SSMF strand itself.

Note that in this last case the values of $\sigma_G|_{max}$ are $0.2 dB$ and $0.3 dB$ for $L_{SSMF} = 70 m$ and $L_{SSMF} = 100 m$, respectively, which, unlike the case when the initial $SMF_{5\mu m}$ patch

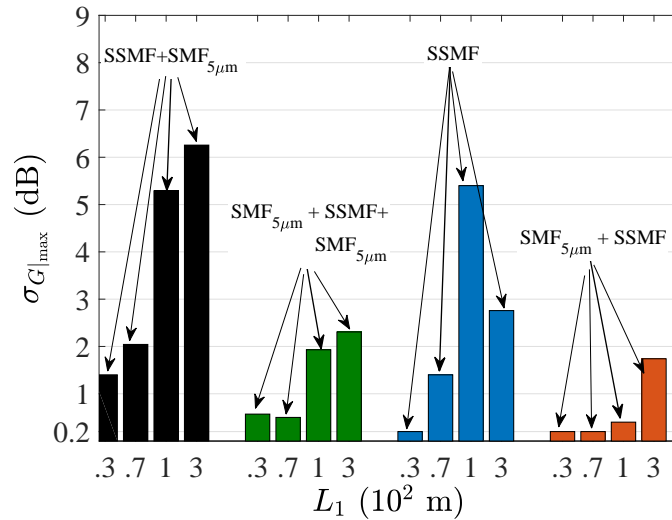


Figure 2.13: Behaviors of $\sigma_{G|_{max}}$ for links of different length L_{SSMF} in the four configurations of VCSEL-based transmission links considered in the present work.

is absent, makes the system potentially usable in typical VLBI downlink chains. Indeed, for these applications, fluctuations of G of the order of 0.4 dB are typically required under a temperature stress $\Delta T = 4^\circ\text{C}$ [100]. Since the values of $\sigma_{G|_{max}}$ have been measured under a temperature stress $\Delta T \simeq 10^\circ\text{C}$, we can conclude that the system proposed here fulfills requirements which are more strict than mentioned above.

Beside the good behavior of σ_G , it is clear that the optical insertion loss given in the cases SMF_{5μm}+SSMF is such high that the noise figure (and consequently Signal-to-Noise Ratio (SNR)) decreases strongly. To be able of using such link and techniques in real applications, a better coupling between the laser and this type of solution is necessary. To solve partially this problem, a SM VCSEL designed to be coupled with SSMF will be used in next Chapters. Indeed, this solution presents anyway an optical insertion loss between the case of only SSMF and SMF_{5μm}+SSMF, but with a lower weight which is acceptable for applications as it will be shown.

2.4 Exploitation of modal noise for the computation of the frequency chirp factor of 850 nm VCSEL

In this Section a possible way to exploit the two modes propagation inside the SSMF for measuring the chirp parameters of a 850 nm VCSEL source is presented.

The method is based on modal noise produced by propagation within SSMF for the wavelength of 850 nm as it has been shown in previous Section. In particular, the mutual interference of the LP_{01} and LP_{11} modes under temperature stress produces specific fluctuating behaviors of the amplitudes of DC and RF components which are dependent on the terms $\cos(\Delta\beta(t))$ and $\sin(\Delta\beta(t))$ as shown in Equations 2.35 and 2.36.

This fact can be usefully exploited to fit the chirp parameters. Letting the fiber undergo linear temperature variation, the fluctuations feature a sinusoidal behavior with specific characteristics of amplitude and phase, which depend also on frequency chirping. Measuring the phase difference between the amplitude fluctuations of the RF component and the ones of the DC component of the detected current it is possible to directly measure the chirp parameters.

The optical system considered is composed by a single mode, single polarization, 850 nm VCSEL, operating under RF direct modulation, followed by an optical isolator and by a strand of standard G.652 fiber with length L_{SSMF} . To enhance the effect of modal noise, the post-filtering setup shown in previous section will be exploited. As mentioned before, the method could be applied equivalently with a small area photo-detector.

From equation 2.52 it is possible to distinguish RF and DC current components, named i_{DC} and i_{RF} which can be written as follows:

$$i_{out,DC}(t) = I_{DC,0} + \Delta I_{DC}(t) \quad (2.53)$$

$$\begin{aligned} i_{out,RF}(t) &= \Re \{ [I_{out,RF,\Re}(t) - jI_{out,RF,\Im}(t)] e^{j\omega_{RF}t} \} = \\ &= [I_{out,RF,\Re,0} + \Delta I_{out,RF,\Re}(t)] \cos(\omega_{RF}t) + \\ &+ [I_{out,RF,\Im,0} + \Delta I_{out,RF,\Im}(t)] \sin(\omega_{RF}t) \end{aligned} \quad (2.54)$$

where the notation $\Re \{(\cdot)\}$ means that the real part of (\cdot) is taken. In Eq. (2.53) and (2.54) $I_{out,DC,0}$, $I_{out,RF,\Re,0}$, $I_{out,RF,\Im,0}$ are the mean values of the envelopes of DC component, real ($I_{out,RF,\Re}$) and imaginary ($I_{out,RF,\Im}$) RF components given by the following expressions:

$$I_{out,DC,0} = I_0 A_1^2 a_1^2 b_{5\mu m} + A_2^2 a_2^2 b_{5\mu m} \quad (2.55)$$

$$I_{out,RF,\Re,0} = I_0 m_I [A_1^2 a_1^2 b_{5\mu m} \cos(\omega_{RF}\tau_1) + A_2^2 a_2^2 b_{5\mu m} \cos(\omega_{RF}\tau_2)] \quad (2.56)$$

$$I_{out,RF,\Im,0} = I_0 m_I [A_1^2 a_1^2 b_{5\mu m} \sin(\omega_{RF}\tau_1) + A_2^2 a_2^2 b_{5\mu m} \sin(\omega_{RF}\tau_2)] \quad (2.57)$$

while $\Delta I_{out,DC}$, $\Delta I_{out,RF,\Re}$, $\Delta I_{out,RF,\Im}$ are the corresponding fluctuating terms of the envelopes which depend directly on the time variation of $\Delta\beta_{12}(t)$, and can be expanded as follows:

$$\Delta I_{out,DC}(t) = I_0 2A_1 a_1 A_2 a_2 b_{5\mu m} J_0(x) \cos(\Delta\beta_{12}(t)) \quad (2.58)$$

$$\begin{aligned} \Delta I_{out,RF,\Re}(t) = 2I_0 A_1 a_1 A_2 a_2 b_{5\mu m} \cdot [m_I \cos(\omega_{RF} \Delta \tau_{12}) J_0(x) \cos(\omega_{RF} \bar{\tau}_{12}) \cos(\Delta \beta_{12}(t)) + \\ + 2J_1(x) \cos(\omega_{RF} \bar{\tau}_{12} + \psi)] \sin(\Delta \beta_{12}(t)) \end{aligned} \quad (2.59)$$

$$\begin{aligned} \Delta I_{out,RF,\Im}(t) = 2I_0 A_1 a_1 A_2 a_2 b_{5\mu m} \cdot [m_I \cos(\omega_{RF} \Delta \tau_{12}) J_0(x) \sin(\omega_{RF} \bar{\tau}_{12}) \cos(\Delta \beta_{12}(t)) + \\ + 2J_1(x) \sin(\omega_{RF} \bar{\tau}_{12} + \psi)] \sin(\Delta \beta_{12}(t)) \end{aligned} \quad (2.60)$$

Mathematical derivation of the chirp parameters from the phase shifts between DC and RF components

Equations (2.58)-(2.60) show that while in the case of $\Delta I_{DC}(t)$ the time dependence is only given by a term proportional to $\cos(\Delta \beta_{12}(t))$, in the case of $\Delta I_{RF,\Re}(t)$ and $\Delta I_{RF,\Im}(t)$ it is given by two terms which are respectively proportional to $\cos(\Delta \beta_{12}(t))$ and $\sin(\Delta \beta_{12}(t))$. This determines the presence of phase shifts of both $\Delta I_{RF,\Re}(t)$ and $\Delta I_{RF,\Im}(t)$ with respect to $\Delta I_{DC}(t)$. For a given value of ω_{RF} , their expressions are respectively given by:

$$\Delta \phi_{\Re,DC}(\omega_{RF}) = \tan^{-1} [\mathcal{U}(\omega_{RF}, M) \cdot \mathcal{V}_c(\omega_{RF}, \psi)] \quad (2.61)$$

$$\Delta \phi_{\Im,DC}(\omega_{RF}) = \tan^{-1} [\mathcal{U}(\omega_{RF}, M) \cdot \mathcal{V}_s(\omega_{RF}, \psi)] \quad (2.62)$$

where:

$$\mathcal{U}(\omega_{RF}, M) = \frac{2J_1(x)}{m_I \cos(\omega_{RF} \Delta \tau_{12}) J_0(x)} \quad (2.63)$$

$$\mathcal{V}_c(\omega_{RF}, \psi) = \cos(\omega_{RF} \bar{\tau}_{12} + \psi) / \cos(\omega_{RF} \bar{\tau}_{12}) \quad (2.64)$$

$$\mathcal{V}_s(\omega_{RF}, \psi) = \sin(\omega_{RF} \bar{\tau}_{12} + \psi) / \sin(\omega_{RF} \bar{\tau}_{12}) \quad (2.65)$$

The method which is here described consists in determining experimentally $\Delta \phi_{\Re,DC}(\omega_{RF})$, $\Delta \phi_{\Im,DC}(\omega_{RF})$, and subsequently extracting the values of $M(\omega_{RF})$, $\psi(\omega_{RF})$ from the inversion of respectively Eq. (2.61) and Eq. (2.62).

Note that in case the assumption $\psi(\omega_{RF}) \simeq 0$ could be taken, it would be $\mathcal{V}_c \simeq \mathcal{V}_s \simeq 1$ and both Eq. (2.61) and Eq. (2.62) would become

$$\Delta \phi_{\Re,DC} \simeq \Delta \phi_{\Im,DC} \simeq \tan^{-1} [\mathcal{U}(\omega_{RF}, M)] \quad (2.66)$$

The value of M will then have to be determined also for operating conditions where the value of ψ cannot be neglected, i.e. both M and ψ must be extracted from Eq. (2.61) and Eq. (2.62).

This extraction procedure for a given ω_{RF} not only requires the measurement of $\Delta \phi_{\Re,DC}$, $\Delta \phi_{\Im,DC}$ at ω_{RF} , but also in the vicinity of that angular frequency.

Indeed, as will be shown with greater detail, the functions $\mathcal{V}_c(\omega_{RF}, \psi)$, $\mathcal{V}_s(\omega_{RF}, \psi)$ exhibit for varying ω_{RF} tangentoid-like behaviors with a periodicity which is of a few MHz when the value of the length L_{SSMF} of the fiber connection is of the order of a few tens of meters. This determines in turn a fast variation of the second sides of Equations (2.61) and (2.62)

even within relatively small frequency intervals in the vicinity of a given value ω_{RF} . Fig. 2.14 shows examples of theoretical behaviors of these functions for different values of M and ψ in a short interval centered in $f_{RF} = 300 \text{ MHz}$, utilizing typical values for the parameters involved.

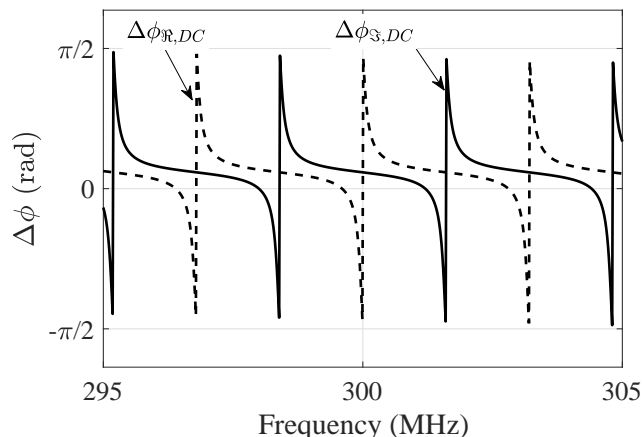


Figure 2.14: Example of theoretical behaviors of $\Delta\phi_{\Re,DC} = \tan^{-1} [\mathcal{U} \cdot \mathcal{V}_c]$ and $\Delta\phi_{\Im,DC} = \tan^{-1} [\mathcal{U} \cdot \mathcal{V}_s]$ for different values of M , ψ . Note that the functions exhibit fast variations with respect to f_{RF} even in the short frequency interval considered. See text for details.

As a consequence of this, it is necessary to have at disposal a high number of measured values of $\Delta\phi_{\Re,DC}$ and $\Delta\phi_{\Im,DC}$ in the vicinity of ω_{RF} in order to perform the extraction operation with satisfactory accuracy.

The extraction procedure can be applied independently either determining experimentally the values of $\Delta\phi_{\Re,DC}$ at various frequencies centered in f_{RF} and then inverting Eq. (2.61), or determining similarly the values of $\Delta\phi_{\Im,DC}$ and then inverting Eq. (2.62). Both procedures lead to obtain the same values of $M(\omega_{RF})$, $\psi(\omega_{RF})$. In the remainder, the focus will be maintained to the former procedure, namely the one which exploits the inversion of Eq. (2.61).

Evaluation of M and ψ from the phase differences between RF and DC fluctuating components of the photocurrent

The expression of $\Delta\phi_{\Re,DC}$ given by equation (2.61) depends in turn on the relations expressed by equations (2.63) and (2.64). The first one contains the information about M (through x , given by Eq. (2.26)), while the other one about ψ .

To identify the contribution of each of these two variables on Eq. (2.61) the function $\mathcal{V}_c(\omega_{RF}, \psi)$ is initially considered, It can indeed be observed that such function is periodical in ω_{RF} (or f_{RF}) with period given by $\Omega = \pi/\bar{\tau}_{12}$ (or $F = 1/(2\bar{\tau}_{12})$). Since it is $\bar{\tau}_{12} \simeq 0.5 \cdot 10^{-9} \cdot L$, with L in the order of tens of meters, the value of F is of the order of a few MHz. Within this interval, $\mathcal{V}_c(\omega_{RF}, \psi)$ encompasses all the values in the interval $]-\infty, \infty[$. A reasonable approximation that can be taken at this point is that in the range of frequencies Δf_{RF} given

by a very few periods F (or, equivalently, in the range of angular frequencies $\Delta\omega_{RF}$ given by a very few periods Ω) the variations of M and ψ with respect to frequency are much slower than the ones of $\mathcal{V}_e(\omega_{RF}, \psi)$ (see Eq. (2.14) and (2.15)). Indeed, considering a reference angular frequency $\bar{\omega}_{RF} \in 2\pi \cdot [100, 1500] \text{ MHz}$, and typical operating conditions, for a generic $\omega_{RF} \in \Delta\bar{\omega}_{RF} = [\bar{\omega}_{RF} - \Delta\omega_{RF}/2, \bar{\omega}_{RF} + \Delta\omega_{RF}/2]$ it is in line with the models generally assumed in literature [1, 90, 101] to take:

$$\left| \frac{\partial M}{\partial \omega_{RF}}(\omega_{RF} - \bar{\omega}_{RF}) \right| \ll |M(\bar{\omega}_{RF})| \quad (2.67)$$

$$\left| \frac{\partial \psi}{\partial \omega_{RF}}(\omega_{RF} - \bar{\omega}_{RF}) \right| \ll |\psi(\bar{\omega}_{RF})| \quad (2.68)$$

This practically means that within the interval $\Delta\omega_{RF}$ centered in $\bar{\omega}_{RF}$ the values of M and ψ can be considered to be constant: $M|_{\omega_{RF} \in \Delta\bar{\omega}_{RF}} \simeq M(\bar{\omega}_{RF})$, $\psi|_{\omega_{RF} \in \Delta\bar{\omega}_{RF}} \simeq \psi(\bar{\omega}_{RF})$.

Remembering that it is $\Delta\tau_{12} \sim 10^{-12} \cdot L$, the same considerations can be applied to the function \mathcal{U} given by Eq. (2.63), which will be considered to be constant in the same interval: $\mathcal{U}|_{\omega_{RF} \in \Delta\bar{\omega}_{RF}} \simeq \mathcal{U}(\bar{\omega}_{RF}, M(\bar{\omega}_{RF}))$.

The considerations developed above simplify equation (2.61) and allow to operate in a single interval $\Delta\bar{\omega}_{RF}$ around the desired frequency $\bar{\omega}_{RF}$, in which equation (2.61) can be written as follows:

$$\Delta\phi_{\Re, DC} = \tan^{-1} [\mathcal{U}(\bar{\omega}_{RF}, M(\bar{\omega}_{RF})) \cdot \mathcal{V}_e(\omega_{RF}, \psi(\bar{\omega}_{RF}))] \quad (2.69)$$

To separate the contributions of M and ψ to $\Delta\phi_{\Re, DC}$, a procedure is utilized which requires two steps.

The first one consists in computing the absolute value of $\Delta\phi_{\Re, DC}$ and subsequently perform its average on the frequency values. Formally, the expression can be written as $\langle |\Delta\phi_{\Re, DC}| \rangle$ in which $\langle \cdot \rangle$ is the frequency mean operator. The operation of averaging allows to achieve the independence of the function on the periodicity in ω_{RF} of $\mathcal{V}_e(\omega_{RF}, \psi(\bar{\omega}_{RF}))$, while performing the absolute value allows to achieve its independence (or weak dependence) on the quantity ψ .

This point is further detailed in Figures 2.15a and 2.15b. Note that in Figure 2.15a the intersections between the hypothetical measured value $\langle |\Delta\hat{\phi}_{\Re, DC}| \rangle$ and the functions $\langle |\tan^{-1}(\mathcal{U} \cdot \mathcal{V}_e)| \rangle$ give a restricted interval of possible solutions of \mathcal{U} , which constitutes a useful first step for the resolution of the problem. In Figure 2.15b instead, the intersections between $\langle \Delta\hat{\phi}_{\Re, DC} \rangle$ and $\langle \tan^{-1}(\mathcal{U} \cdot \mathcal{V}_e) \rangle$ produce a larger range of possible values of \mathcal{U} and ψ which makes the problem indeterminate.

Figure 2.16a shows this first step of the procedure in which the following relation is solved:

$$\langle |\Delta\hat{\phi}_{\Re, DC}| \rangle = \langle |\tan^{-1} [\mathcal{U}(\bar{\omega}_{RF}, M(\bar{\omega}_{RF})) \cdot \mathcal{V}_e(\omega_{RF}, \psi(\bar{\omega}_{RF}))]| \rangle \quad (2.70)$$

in which $\Delta\hat{\phi}_{\Re, DC}$ represents the measured phase-shift among RF real part and DC component of the output current. Eq. (2.70) allows to find a first set of possible solutions (\mathcal{U}_{sol} ,

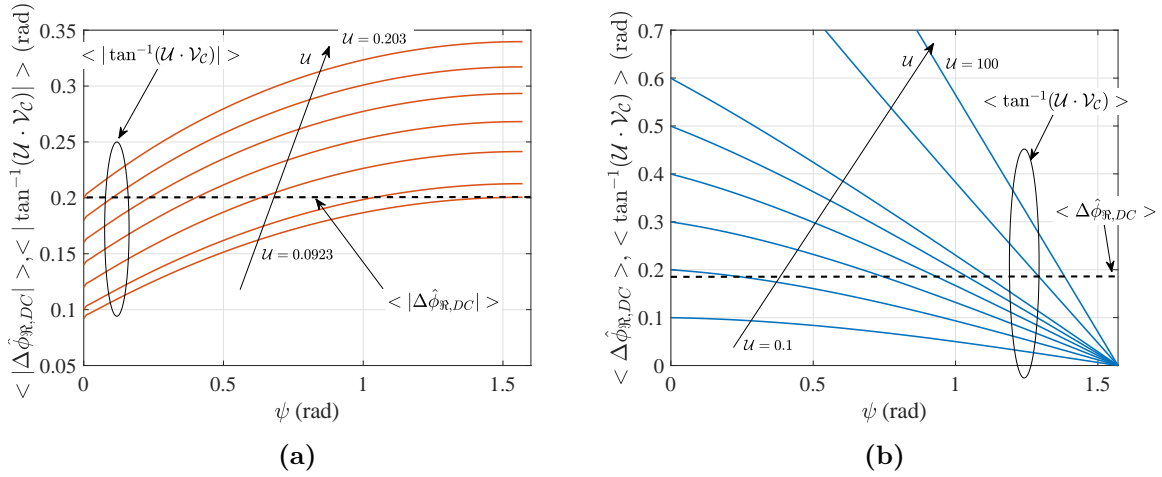


Figure 2.15: Dependence of the functions $\langle |\Delta\phi_{\mathcal{R},DC}| \rangle$ (a) and $\langle \Delta\phi_{\mathcal{R},DC} \rangle$ (b) on the variable ψ fixing different values of \mathcal{U} . The intersections \mathcal{U} with the measured value $\langle |\Delta\hat{\phi}_{\mathcal{R},DC}| \rangle$ restrict the possible solution to a small interval of \mathcal{U} , while the intersections with $\langle \Delta\phi_{\mathcal{R},DC} \rangle$ make the resolution of the problem difficult.

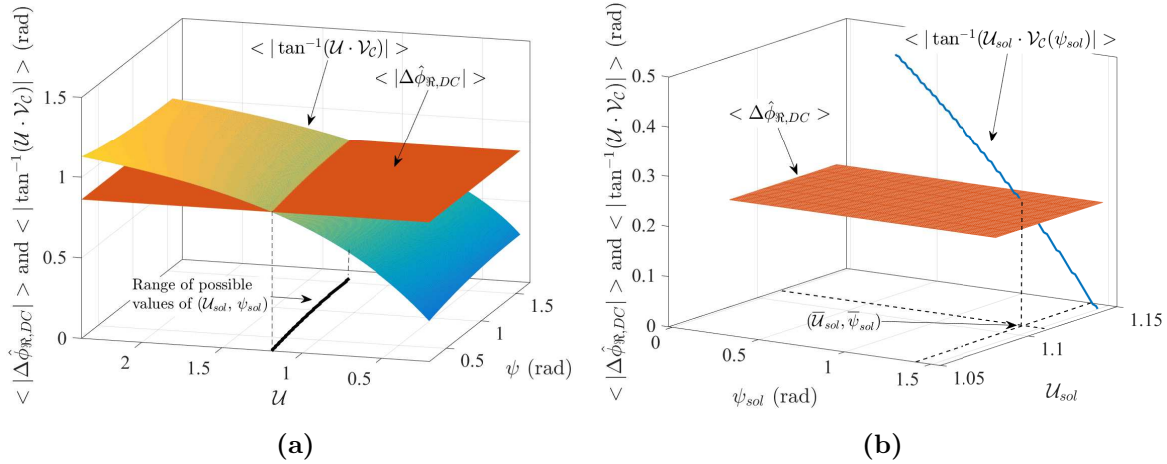


Figure 2.16: (a) 3D plot of the function $\langle |\Delta\phi_{\mathcal{R},DC}| \rangle$ and of the plane $\langle \Delta\hat{\phi}_{\mathcal{R},DC} \rangle$. The intersection produces possible couples of solution $(\mathcal{U}_{sol}, \psi_{sol})$. (b) 3D plot of the function $\langle \Delta\phi_{\mathcal{R},DC} \rangle$ computed in the values founded in the first step $(\mathcal{U}_{sol}, \psi_{sol})$. The intersection with the plane corresponding to $\langle \Delta\hat{\phi}_{\mathcal{R},DC} \rangle$ gives the final solution.

ψ_{sol}) where \mathcal{U}_{sol} belongs to a restricted region in the surrounding of $\tan \left(\langle |\Delta\hat{\phi}_{\Re,DC}| \rangle \right)$, while $\psi_{sol} \in [0, \pi/2]$. It can be appreciated in Figure 2.16a that the application of the operator $\langle |\cdot| \rangle$ makes the possible values of \mathcal{U}_{sol} to fall into to a quite restricted region.

The second and final step of the procedure consists in considering the solutions $(\mathcal{U}_{sol}, \psi_{sol})$ determined at the first step and determine among them the one which solves the equation:

$$\langle \Delta\hat{\phi}_{\Re,DC} \rangle = \langle \tan^{-1} [\overline{\mathcal{U}}_{sol}(\overline{\omega}_{RF}, M(\overline{\omega}_{RF})) \cdot \mathcal{V}_c(\omega_{RF}, \overline{\psi}_{sol}(\overline{\omega}_{RF}))] \rangle \quad (2.71)$$

which coincides with Equation (2.70) save for the absence of computation of the absolute value.

This operation allows to identify the exact solution $(\overline{\mathcal{U}}_{sol}, \overline{\psi}_{sol})$ of the problem.

After having solved Equation (2.71), the extrapolation of M from $\overline{\mathcal{U}}_{sol}(\overline{\omega}_{RF}, M(\overline{\omega}_{RF}))$ can be directly performed from Equation (2.63).

Experimental Application of the method

The method just exposed is applied to 850 nm SM VCSEL, since the model has been developed taking into account only one emission line. Beside the different laser, the experimental setup is the same as in the case of post-filtering technique (see Figure 2.1) in which a short span of SMF_{5μm} is inserted right after the SSMF span. The reason lies in the enhancement of modal noise as explained and proved in Section 2.3. This allows to improve the quality of the measurement of $\Delta I_{out,DC}$, $\Delta I_{out,RF,\Re}$ and $\Delta I_{out,RF,\Im}$. The L-I curve and the optical spectrum at different I_{bias} of the SM VCSEL employed are shown in Figure 2.17.

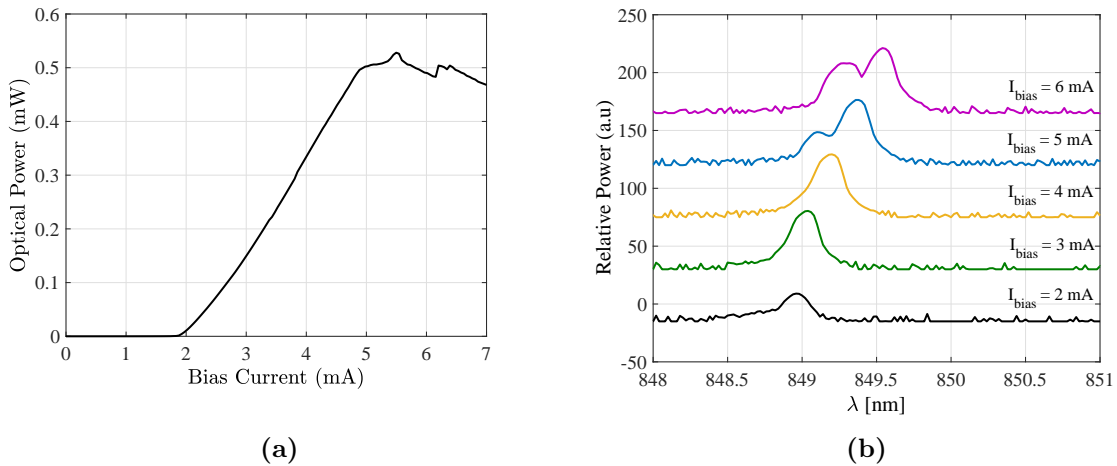


Figure 2.17: L-I curve (a) and optical spectrum at different biasing (b) for the SM VCSEL considered.

In this case 30 meters of G.652 fiber are placed into the controlled climatic chamber and an isolator is placed right after the laser to avoid back reflections that can affect the measurements.

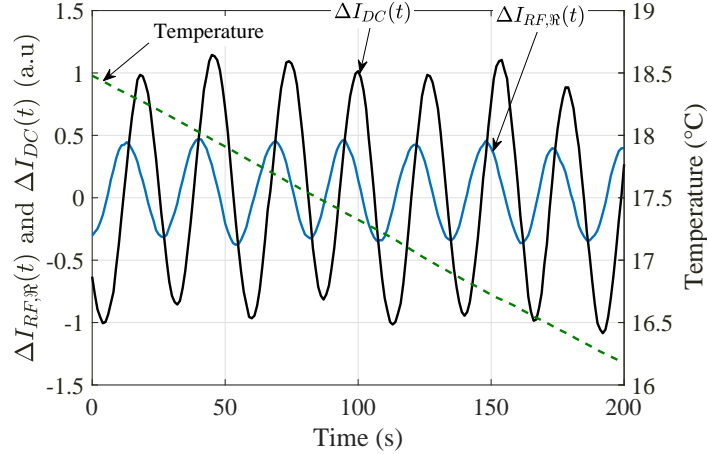


Figure 2.18: Typical measurement in the time domain of $\Delta I_{DC}(t)$ and $\Delta I_{RF,\Re}(t)$. The value of the modulating frequency is $f_{RF} = 300 \text{ MHz}$. The phase shift between the two fluctuating behaviors is clearly visible. In this case it is $\Delta\phi_{\Re,DC} \simeq -0.075 \text{ rad}$.

In order to perform correctly the extraction of the parameters $M(\omega_{RF})$, $\psi(\omega_{RF})$ for a given frequency $f_{RF} = \omega_{RF}/(2\pi)$, the measured values of $\Delta\phi_{\Re,DC}$ (or $\Delta\phi_{\Im,DC}$) should be available for a high number of frequencies in the vicinity of ω_{RF} . For this reason the measurement is performed in correspondence to 1001 equally spaced frequencies located in a small interval centered in f_{RF} . The width of such interval has been chosen as 10 MHz .

For each one of such frequencies, data from VNA and acquisition block are taken with a period of one second, which is appropriate in view of the subsequent processing of the received signal, which is based on its Discrete Fourier Transform (DFT). Indeed, with the temperature variations imposed in the experiments, the periods of the fluctuating behaviors of $\Delta I_{DC}(t)$ and $\Delta I_{RF,\Re}(t)$, (and also of $\Delta I_{RF,\Im}(t)$) do not fall in any case below values of tens of seconds. The frequencies considered for determining $M(\omega_{RF})$ and $\psi(\omega_{RF})$ ranged from 100 MHz to 1.5 GHz with intervals of 50 MHz . The value of the OMI has always been kept lower than 10%. As mentioned above, for each one of the RF frequencies considered, after having performed the time measurements of $\Delta I_{DC}(t)$ and $\Delta I_{RF,\Re}(t)$ (see Fig. 2.18), the DFT is applied to the time waveforms to extrapolate the phase difference $\Delta\hat{\phi}_{\Re,DC}$. Figure 2.19 shows typical measured values of $\Delta\hat{\phi}_{\Re,DC}$ for different centered frequencies f_{RF} .

The values obtained of M and ψ are shown in Figure 2.20a. Note that M is shown performing a normalization with respect to the optical modulation index m_I , which shows directly the FM/AM relation. Furthermore, it is worth to point out that modal birefringence has been considered negligible in this work. The reason is that contribution in terms of intra-modal delay is in the order of tens of ps/Km for weakly guided few modes fiber [102]. This value is 1000 times lower than the group delay measured $\Delta\tilde{\tau}_{12}$ and its contribution can therefore be neglected.

The chirp characterization of the same laser source has been performed also employing the procedure described in [103]. The application of this method requires that the system operates

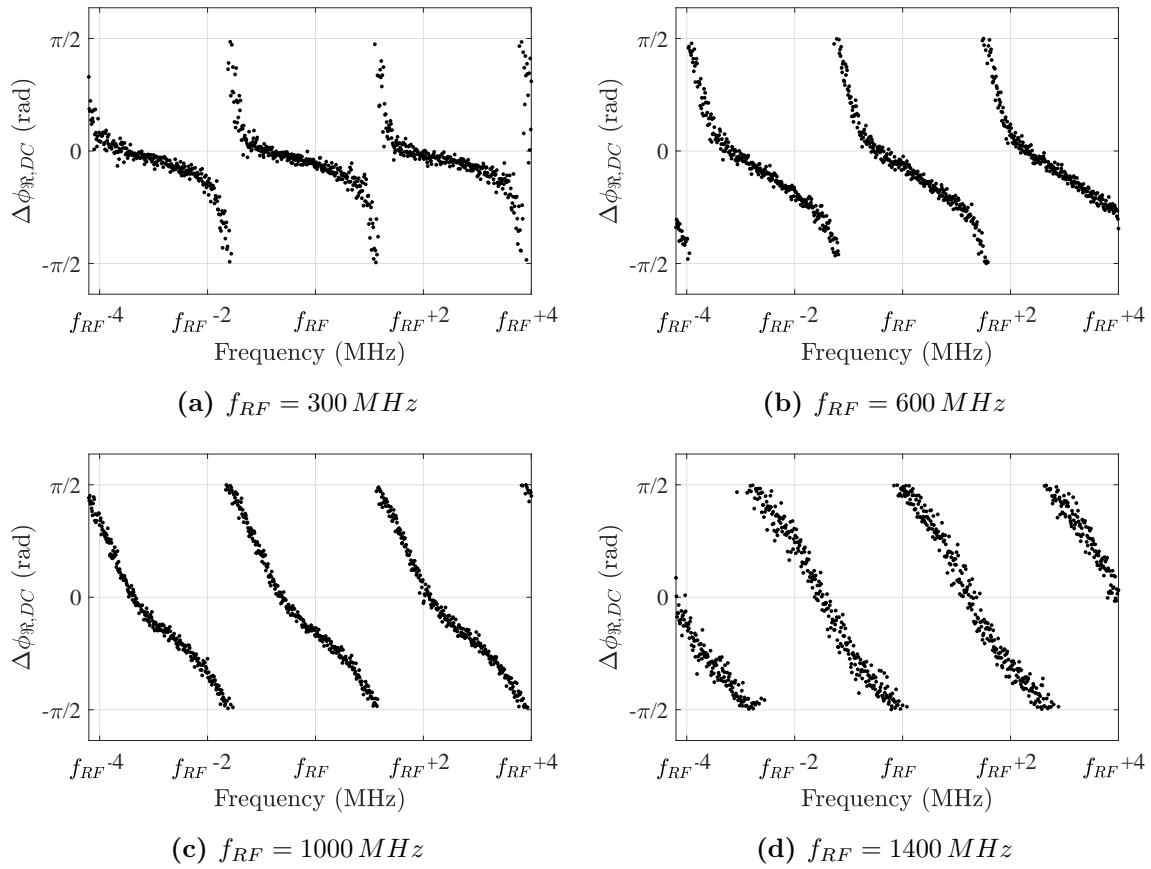


Figure 2.19: Example of four different measurements of $\Delta\phi_{\mathcal{R},DC}$ for four center frequencies f_{RF} .

in single-mode regime, and is consequently suited for characterizing laser sources operating in the second and third optical windows. To realize this technique a number of components exhibiting a truly single mode behavior at 850 nm have been utilized, including a strand 100 m long of SMF_{5μm} fiber, which may not be typically present in an optics laboratory. The purpose of performing the measurement also with this technique was however to validate the method proposed.

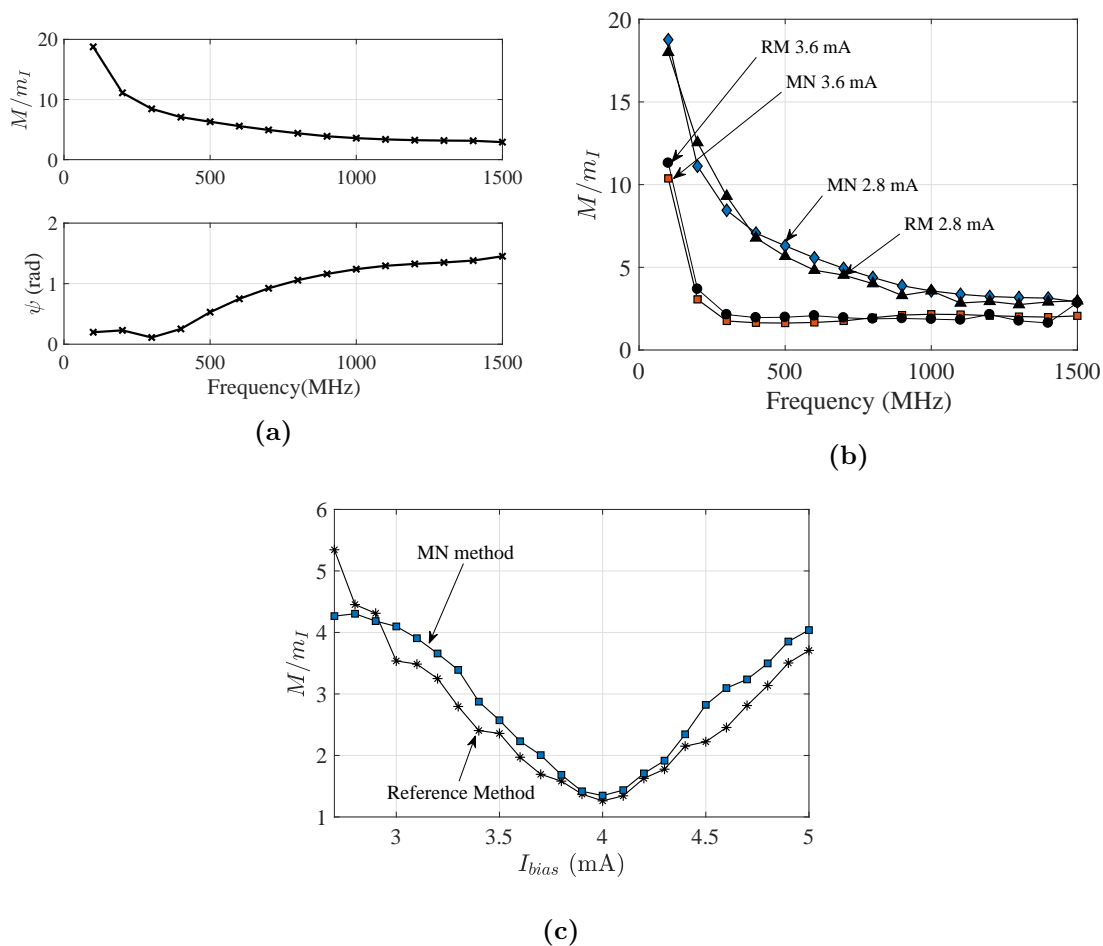


Figure 2.20: (a) Example of results obtained from the implementation of the method proposed. (b) Comparison of the proposed technique based on Modal Noise (MN) with the method taken as reference (RM) proposed by [103]. The comparison is shown for two different level of biasing. (c) Application of the proposed and reference method for $f_{RF} = 800 \text{ MHz}$ for different values of I_{bias} .

The comparison of the two methods are shown in Figure 2.20b for two different values of bias current. An average relative difference among the two methods has been found to be around 10% with a standard deviation of 5.5% which are quantities considered acceptable. To have a further validation, the method has been also applied fixing $f_{RF} = 800 \text{ MHz}$ for different values of biasing current I_{bias} (see Figure 2.20c). An average difference among the

two methods has been found to be about 12% with a standard deviation of 6%. Note that in this case the laser presents a minimum of M/m_I (therefore of M) for $I_{bias} = 4 mA$, which can be exploited to improve the quality of transmission. Moreover, this type of behavior is also in agreement to what has been observed for other semiconductor lasers [104].

Accuracy and tolerance of the method proposed

The accuracy of the proposed method depends on many factors which are summarized hereafter.

- **Number of points in the frequency interval considered**

The density of measurement points should be high enough to guarantee an accurate measurement of $\Delta\phi_{\Re,DC}$ (or $\Delta\phi_{\Im,DC}$) within one frequency period $F = 1/(2\bar{\tau}_{12})$ of the function $\mathcal{V}_e(\omega_{RF}, \psi)$ (or $\mathcal{V}_s(\omega_{RF}, \psi)$). In the present case it can be estimated $\bar{\tau} \simeq 5 \cdot 10^{-9} \cdot L \text{ sec}$, which results in $F \simeq 3 \text{ MHz}$ if $L = 33 \text{ m}$. It was found that measuring $\Delta\phi_{\Re,DC}$ (or $\Delta\phi_{\Im,DC}$) at frequencies separated by 10 KHz , which corresponds to about 300 samples per frequency period, and performing an averaging of the obtained results, gives repeatable values of $\Delta\phi_{\Re,DC}$ (or $\Delta\phi_{\Im,DC}$). To further increase the confidence on the measurement, a frequency span of $3F$ has been always considered, with the same sampling rate, which however gave the same values of $\Delta\phi_{\Re,DC}$ (or $\Delta\phi_{\Im,DC}$) obtained considering a frequency span just equal to F .

- **Appropriate length of the Standard Single Mode Fiber span**

The sampling period adopted for measuring the time waveform at each measurement frequency should be low enough to measure properly the sinusoidal variation due to modal noise. The period of the sinusoidal waveform depends on the parameter $\Delta(\dot{\beta}_{12})$ which in turn depends proportionally on the temperature time slope $\frac{dT}{dt}$ and on SSMF length L_{SSMF} , while is independent from the SMF_{5μm} length. Formally it can be written as:

$$\Delta(\dot{\beta}_{12}) = \frac{2\pi}{\lambda} L_{SSMF} \left[\Delta n_{eff,12} \frac{dL_{SSMF}}{L_{SSMF} dT} + \left(\frac{dn_{eff,1}}{dT} - \frac{dn_{eff,2}}{dT} \right) \right] \cdot \frac{dT}{dt} \quad (2.72)$$

in which $\Delta n_{eff,12} = (n_{eff,1} - n_{eff,2})$ where $n_{eff,1}$ and $n_{eff,2}$ are the effective refractive indexes of mode 1 and 2 respectively. The time behavior of the fluctuations is governed by the terms $\cos[\Delta(\dot{\beta}_{12}) \cdot t]$ and $\sin[\Delta(\dot{\beta}_{12}) \cdot t]$ having a time period \mathcal{T} given by

$$\mathcal{T} = \frac{\lambda}{\left[\Delta n_{eff,12} \frac{dL_{SSMF}}{L_{SSMF} dT} + \left(\frac{dn_{eff,1}}{dT} - \frac{dn_{eff,2}}{dT} \right) \right] \cdot L_{SSMF} \frac{dT}{dt}} \quad (2.73)$$

In the presented case it is $L_{SSMF} = 30 \text{ m}$ and $\frac{dT}{dt} \simeq 1.1 \cdot 10^{-2} \text{ K/s}$ (see Figure 2.18). It can also be taken $\Delta n_{eff,12} \simeq 1.2 \cdot 10^{-3}$ [105] and $\frac{dL_{SSMF}}{L_{SSMF} dT}$ of the order of $5 \cdot 10^{-7} \text{ K}^{-1}$ [106]. Moreover, considering that for the refractive index of silica it is $5 \cdot 10^{-6} \leq \frac{dn}{dT} \leq 3 \cdot 10^{-5} \text{ K}^{-1}$ [107], it is reasonable to think that $\frac{dn_{eff,1}}{dT} - \frac{dn_{eff,2}}{dT}$ is at least two orders of magnitude smaller, due to the vicinity of the two effective refractive indexes, and can

therefore be estimated to be not higher than $10^{-7} K^{-1}$, bringing finally to be \mathcal{T} of the order of a few tens of seconds. The utilized sampling period of $T_s = 1 s$ gives the number of measured samples per period which guarantees an accurate evaluation of $\Delta\phi_{\mathfrak{R},DC}$ (or $\Delta\phi_{\mathfrak{S},DC}$ at the considered frequency).

Note from Eq. (2.73) that the fluctuations period is inversely proportional to L and $\frac{dT}{dt}$. For the value utilized of $\frac{dT}{dt}$, the chosen value of $L_{SSMF} = 30 m$ results from a compromise between the necessity of having L long enough, to guarantee not too high values of \mathcal{T} (which would mean too long measurement times), and the necessity to have L_{SSMF} short enough to allow an adequate sampling of the fluctuating waveforms, and to avoid coupling between the two modes, which can be taken as negligible only up to tens or hundreds of meters [95].

- **Necessity of misalignment between SSMF and SMF_{5μm}**

The higher the amplitude of fluctuations, the higher the precision of the measurements. The amplitude is enhanced in this work exploiting the SMF_{5μm} fiber right after the SSMF. This insertion enhances the fluctuations due to the fact that this type of connection is highly sensitive to misalignment. The total absence of fluctuations ($a_2 = 0$) would take place in case of perfect alignment and cannot be theoretically excluded. However it does not constitute a realistic operating condition in presence of commercial connectors. Considering for example a small misalignment of $0.2 \mu m$ between SSMF and SMF_{5μm}, from Eq.(2.51) it is $a_2 = 0.03$, which is large enough to have fluctuations.

2.5 Interferometry-Based (IB) technique for measuring the chirp factor of DFB lasers

This Section aims to investigate the possibility of applying the same concept discussed in the previous section to the case of a DFB laser operating a 1310 nm or 1550 nm. For DFB lasers of commercial use in fact, it is possible to consider f_c around the order of some GHz thanks to the low non linear gain value and the higher power compared to VCSEL [86, 108]. This means that when values of f_{RF} are of the order of hundreds of MHz or also few GHz, the approximation $\left(\frac{\omega_{RF}}{\omega_c}\right) \ll 1$ can be taken [6, 109–111], which means to assume that the adiabatic chirp term prevails over the transient one ($\psi \simeq 0$), and M can be expressed as $M = \frac{K_f I_{RF}}{f_{RF}}$, in which K_f is the *adiabatic chirp coefficient*.

To re-create and analogous situation of the method proposed in the previous Section the scheme shown in Figure 2.21 is considered.

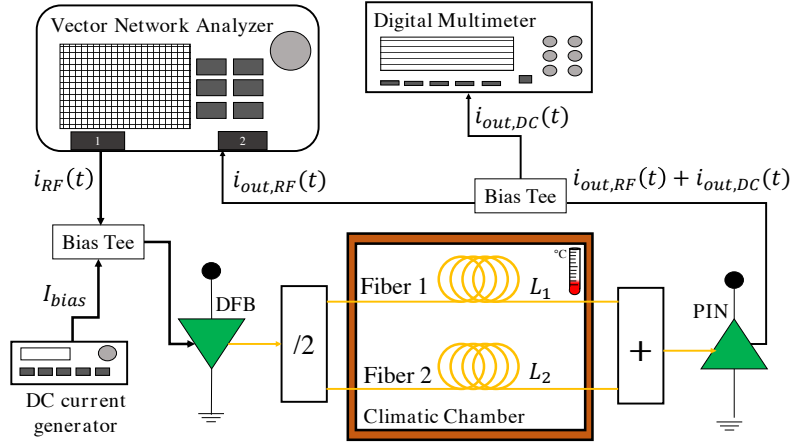


Figure 2.21: Experimental setup utilized to apply the method of determination of K_f . See text for details

Hence, with the aid of an optical directional coupler, the electrical field is equally split into two spans of single mode fiber. It is then:

$$|\bar{E}_{in,1}(t)| = |\bar{E}_{in,2}(t)| = \frac{|\bar{E}_{in}(t)|}{\sqrt{2}} \quad (2.74)$$

where $\bar{E}_{in,1}(t)$ and $\bar{E}_{in,2}(t)$ are the input fields of fiber 1 and fiber 2 respectively having the same expression of Eq (2.16) with $N_W = 1$.

The propagation in the two different fiber spans leads to different delays of the two fundamental modes. In particular, it is $\tau_1 = \tilde{\tau}_1 L_1 = \frac{n_{g1}}{c} L_1$ for fiber 1, and $\tau_2 = \tilde{\tau}_2 L_2 = \frac{n_{g2}}{c} L_2$ for fiber 2, where L_i , $\tilde{\tau}_i$ and n_{gi} ($i = 1, 2$) are respectively the length, the mode group delay per unit length and the mode group refractive index referred to the i -th fiber, and where c is the speed of light. At the end of the propagation inside the fibers, an optical coupler performs

the complementary function of the splitter, giving the following electrical field $\bar{E}_{out}(t)$:

$$\begin{aligned} \bar{E}_{out}(t) = \frac{E_0}{2} \bar{e} \left\{ \sqrt{1 + m_I \cos(\omega_{RF}(t - \tau_1))} \cdot e^{j\left[\omega_0 t - \beta_1(t) + \frac{K_f I_{RF}}{f_{RF}} \sin(\omega_{RF}(t - \tau_1))\right]} + \right. \\ \left. + \sqrt{1 + m_I \cos(\omega_{RF}(t - \tau_2))} \cdot e^{j\left[\omega_0 t - \beta_2(t) + \frac{K_f I_{RF}}{f_{RF}} \sin(\omega_{RF}(t - \tau_2))\right]} \right\} \end{aligned} \quad (2.75)$$

In (2.75) the optical phase terms $\beta_1 = n_{eff1} \frac{\omega_0}{c} L_1$ and $\beta_2 = n_{eff2} \frac{\omega_0}{c} L_2$, where n_{effi} ($i = 1, 2$) is the mode effective refractive index referred to the i -th fiber, have been assumed to vary in time due to possible changes of temperature. Note that strictly speaking, the same changes determine also the group delays to vary with time. However, these variations are much slower than the variations of $\beta_1(t)$, $\beta_2(t)$. Indeed, typically for a mode propagating with group index n_g and effective index n_{eff} in a standard single mode optical fiber of length L , both $\frac{dn_g}{dT}$ and $\frac{dn_{eff}}{dT}$ are of the order of 10^{-5} K^{-1} , while $\frac{dL}{dT}$ is of the order of few 10^{-7} K^{-1} [106] [112]. In front of the same rate of temperature change $\frac{dT}{dt}$, the speed of phase change caused by the variation of the group delay is then $\omega_{RF}/\omega_0 \sim 10^{-5}$ times the one caused by the variation of the optical phase term. As will be later clarified, this fact brings as a consequence that the approximation of considering τ_1 and τ_2 not to vary with time can be regarded as applicable to the method here presented.

Equation (2.75) results to be of the same shape of Equation (2.19) with the only difference that the two propagating fields are considered of exactly the same weight and shape. This fact leads to $b_{11} = b_{22} = b_{21} = 1$ where the output current is computed exploiting Eq. (2.20), leading to a simplification of Equations (2.31) and (2.32), Equations (2.33) and (2.34) and Equations (2.35) and (2.36), for which $\psi = 0$, $N_m = 2$ and $b_{ii} = 1$ and $A_i^2 = 0.5$ for $i = 1, 2$. This means that the fluctuations reach the maximum possible value. Since $\psi = 0$ it is $\Delta\phi_{\Re, DC} = \Delta\phi_{\Im, DC} = \Delta\phi$ which can be simply expressed by:

$$\Delta\phi = \tan^{-1} \left[\frac{2J_1(x)}{m_I \cos(\omega_{RF}\Delta\tau) J_0(x)} \right] \quad (2.76)$$

which can be used to determine directly K_f . In fact, it can be noted that the argument of the function \tan^{-1} at the second side of (2.76) is simplifiable when $f_{RF}\Delta\tau \ll \frac{1}{2\pi}$. In this case, it is indeed possible to apply the following approximations:

$$\cos(2\pi f_{RF}\Delta\tau) \simeq 1 \quad (2.77)$$

$$\sin(2\pi f_{RF}\Delta\tau) \simeq 2\pi f_{RF}\Delta\tau \quad (2.78)$$

$$x \simeq 4\pi K_f I_{RF}\Delta\tau \quad (2.79)$$

Furthermore, if the product $I_{RF}K_f$ is such that $x \ll 1$ the Bessel functions J_0 and J_1 can be approximated at first order as:

$$J_1(x) \simeq \frac{x}{2} \quad (2.80)$$

$$J_0(x) \simeq 1 \quad (2.81)$$

leading to the following relationship of $\Delta\phi$:

$$K_f = \frac{\tan(\Delta\phi)}{4\pi(I_{bias} - I_{th})\Delta\tau} \quad (2.82)$$

where $\Delta\phi$ represents the phase shift between RF and DC output current components produced by the chirp coefficient. The equation above states that once $\Delta\tau$ and $(I_{bias} - I_{th})$ are fixed, for low frequency and modulating RF current values it is possible to compute straightforwardly K_f .

However, in the general case a numerical approach has to be followed in the computation of K_f , since Eq. (2.76) does not allow a direct inversion of the relationship between $\Delta\phi$ and K_f . As it will be explained in the next section, in this case multiple values of K_f can correspond to the same value of $\Delta\phi$, and this brings as a consequence the necessity to perform different measurements with different values of I_{RF} for the univocal determination of the laser adiabatic chirp factor.

The hypothesis of considering τ_1 and τ_2 not to vary with time can now be further motivated. Assuming that the two spans of fiber are coming from the same manufacturer, the following conditions can reasonably be taken.

$$\left| \frac{d\beta_1}{dT} - \frac{d\beta_2}{dT} \right| \leq \left| \frac{1}{10} \frac{d\beta_i}{dT} \right| \quad i = 1, 2 \quad (2.83)$$

$$\left| \frac{d\tau_1}{dT} - \frac{d\tau_2}{dT} \right| \leq \left| \frac{1}{10} \frac{d\tau_i}{dT} \right| \quad i = 1, 2 \quad (2.84)$$

$$\frac{1}{2} \left(\frac{d\tau_1}{dT} + \frac{d\tau_2}{dT} \right) \sim \left| \frac{d\tau_i}{dT} \right| \quad i = 1, 2 \quad (2.85)$$

$$(2.86)$$

Due to the fact that in our experiments it is $\frac{dT}{dt} \simeq \frac{1}{500}$ K/sec, considering fiber lengths of a few hundred meters, the terms $\cos(\Delta\beta(t))$ and $\sin(\Delta\beta(t))$ feature angular velocities between about 0.5 rad/sec and 5 rad/sec. Looking at Equations (2.33) and (2.34), the time behaviors of \mathcal{B}_c and \mathcal{B}_s are proportional to $\cos(\omega_{RF}\bar{\tau})$ and $\sin(\omega_{RF}\bar{\tau})$, respectively. While $\mathcal{C}_c(t)$ and $\mathcal{C}_s(t)$ vary on the same time scales of $\cos(\Delta\beta(t))$ and $\sin(\Delta\beta(t))$, the terms $\cos(\omega_{RF}\bar{\tau})$ and $\sin(\omega_{RF}\bar{\tau})$, for frequencies ranging from a few hundred MHz to a few hundred GHz, present angular velocities around $10^{-4}, 10^{-5}$ rad/sec. The time behavior of $\mathcal{C}_c(t)$ and $\mathcal{C}_s(t)$, and consequently of $\Delta I_{out,RF,\Re}(t)$ and $\Delta I_{out,RF,\Im}(t)$ is practically not influenced by this slow modulation. In the intervals of observation time, which are always smaller than 1000 sec (corresponding to $\Delta T \simeq 2$ K), the quantity $\bar{\tau}$ can then be assumed to be constant.

As for the quantity $\Delta\tau$, it can be observed that in the same conditions specified above, for a temperature variation ΔT of one or two Kelvin, it can be assumed $|\frac{d\tau_1}{dT}\Delta T - \frac{d\tau_2}{dT}\Delta T| \leq \frac{1}{100}|\Delta\tau|$. It has also to be noted that the frequencies f_{RF} at which K_f is evaluated, are chosen in order that $\omega_{RF}\Delta\tau$ is about 0.3 rad away from $m\frac{\pi}{2}$ with $m = 0, 1, \dots$. Indeed, this guarantees that both $\cos(\omega_{RF}\Delta\tau)$ and $\sin(\omega_{RF}\Delta\tau)$ (to which, according to (2.26) x is proportional) are sufficiently far from zero, and allows $\mathcal{C}_c(t)$ and $\mathcal{C}_s(t)$ to exhibit both the term proportional to

$\sin(\Delta\beta(t))$ and the term proportional to $\cos(\Delta\beta(t))$.

From a direct mathematical derivation, it can be shown that, for frequencies f_{RF} belonging to the interval specified above, admitting an uncertainty of 1% for $\Delta\tau$ in (2.76) brings to an uncertainty in the values of $\Delta\phi$ of a few percent. The time fluctuation of $\Delta\tau$ can be one of the reasons that cause the measured values of the quantity $\Delta\phi$ to exhibit fluctuations of a few percent, as will be illustrated later in the Chapter. Assuming $\Delta\tau$ to be constant can then bring to the final value of K_f an uncertainty of this order of magnitude, which is in line with the ones presented by other methods (see for example [103]).

Application of the Method and procedure to determine K_f

Referring to Fig. 2.21, a RF signal from a Vectorial Network Analyzer (VNA) is used to directly modulate a DFB laser diode biased at 67 mA through a bias tee on port 1. Its optical power is split into two different paths using a 3 dB coupler, feeding two different spans of fiber on the output. The spans, which are produced by the same manufacturer, exhibit both a nominal length of 200 m and are placed in a climatic chamber, where they undergo a monitored temperature stress. However, note that the presence of the climatic chamber is actually not necessary, but improves the speed and repeatability of the overall measurement process. Indeed, day and night temperature variations are enough for the correct application of the method.

The two output fields are combined using another 3 dB coupler, which is connected to the two spans of fiber on one side and to a PIN photodetector on the other side. The output current generated by the photodetector is split into DC and RF components using a bias tee circuit. The RF component is sent to port 2 of the VNA, which is set for measuring separately the phase and quadrature (“real and imaginary”) terms of S_{21} and consequently of the RF component, while the DC component is measured through a digital multimeter.

To apply the proposed method, the value of $\Delta\tau$ has to be preliminarily determined: in general it depends both on the difference between the group delays over meter of the considered fibers and on the difference between the lengths. From a mathematical point of view, it is:

$$\Delta\tau = \check{\tau}_k \Delta L + L_p(\Delta\check{\tau}) \quad (2.87)$$

where $\Delta L = \frac{L_1 - L_2}{2}$, $\Delta\check{\tau} = \frac{\check{\tau}_1 - \check{\tau}_2}{2}$, and $p, k = 1, 2$ with $p \neq k$.

The characterization of this parameter is possible by making a frequency sweep through the VNA (in our case between 10 MHz and 3 GHz), measuring the module of the time average of $\tilde{I}_{out,RF}(t)$, and computing its first minimum frequency $f_{RF,min}$.

Note indeed that from the relationships $\langle \cos(\Delta\beta(t)) \rangle = 0$, $\langle \sin(\Delta\beta(t)) \rangle = 0$ it comes that $\langle \mathcal{B}_c(t) \rangle = \langle \mathcal{B}_s(t) \rangle = 0$. It is then:

$$\langle \tilde{I}_{out,RF}(t) \rangle = I_0(\mathcal{A}_c + j\mathcal{A}_s) \quad (2.88)$$

and, consequently:

$$| \langle \tilde{I}_{out,RF}(t) \rangle | = I_0 \sqrt{\mathcal{A}_c^2 + \mathcal{A}_s^2} \quad (2.89)$$

Substituting (2.31) and (2.32) in (2.89) it follows that:

$$| \langle \tilde{I}_{out,RF}(t) \rangle | = I_0 m_I \cos(2\pi f_{RF} \Delta\tau) \quad (2.90)$$

Therefore, by measuring the first minimum of the time average of the output RF current module, the value of $\Delta\tau$ can be computed by the following equation:

$$\Delta\tau = \frac{1}{4f_{RF,min}} \quad (2.91)$$

The method was first applied to a DFB laser source having an emission wavelength of 1310 nm. The fact that the optical fibers are produced by the same manufacturer guarantees the possibility to have values of ΔL and $\Delta\tilde{\tau}$ such that the minimum frequency can be easily measured for frequencies in the range of few GHz or less, as shown in Fig. 2.22.

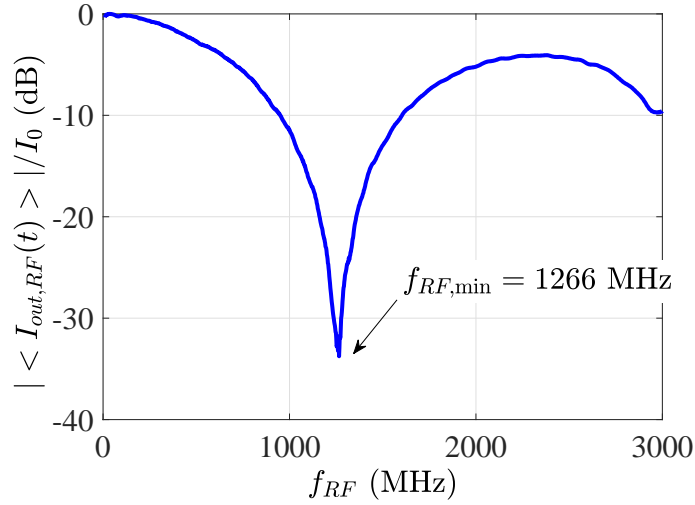


Figure 2.22: Measure of $\frac{\langle I_{out,RF}(t) \rangle}{I_0}$ averaging 200 measurements of 1601 frequencies in the interval [10 MHz - 3 GHz] for the system considered, exploiting a DFB laser source operating at $\lambda = 1310$ nm. See text for details.

A value of $f_{RF,min} = 1.266$ GHz has been measured in this case, with a consequent value of $\Delta\tau = 1.9747 \cdot 10^{-10}$ sec which, to give a reference number, would correspond to $\Delta L \simeq 40$ mm in case the similarity between the two fibers makes the first term at the second side of

(2.87) to prevail. Even under a temperature variation $\Delta T = 10$ K the values of $\Delta\tau$ exhibited a standard deviation $\sigma_{\Delta\tau} = 1.51 \cdot 10^{-12}$ sec, in line with the considerations expressed above.

After the estimation of $\Delta\tau$, the next step is the measurement of the phase difference $\Delta\phi$ between the sinusoidal fluctuations $\Delta I_{out,DC}(t)$ and $\Delta I_{out,RF,\Re}(t)$ (or $\Delta I_{out,RF,\Im}(t)$) of the amplitudes of the DC and RF components of the detected current i_{out} , respectively. For this measurement, the fibers undergo a monitored temperature change, which forces β_1 and β_2 to vary with time. As explained in the previous section, this determines time fluctuations of the amplitudes of the DC and of the RF components of the detected current i_{out} .

The time behaviors of $\Delta I_{out,RF,\Re}(t)$ and $\Delta I_{out,RF,\Im}(t)$ have always observed to be in phase, i.e. to show the same $\Delta\phi$ with respect to $\Delta I_{out,DC}(t)$. Note that this fact is a validation of the assumption taken in the previous Section of neglecting ψ in (2.13).

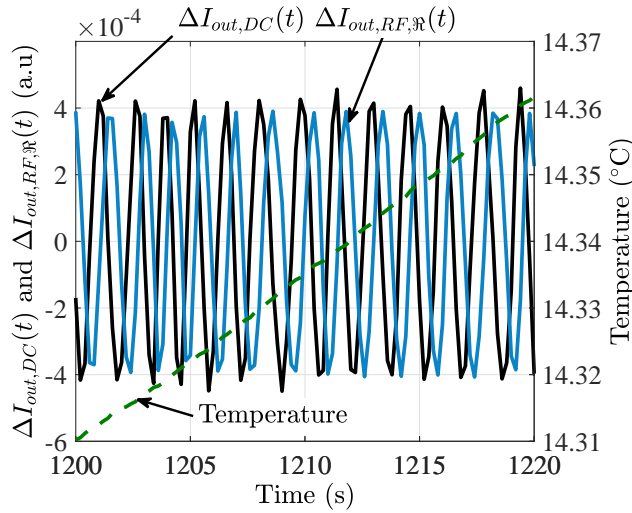


Figure 2.23: Typical measured time behavior of $\Delta I_{out,RF,\Re}(t)$ (light blue curve) and $\Delta I_{out,DC}(t)$ (black curve) for the system represented in Fig. 2.7. See text for details.

The phase shift $\Delta\phi$ is then evaluated employing an algorithm based on the Discrete Fourier Transform (DFT), applied to the measured behaviors (see Figure 2.23) of $\Delta I_{out,DC}(t)$ and to either $\Delta I_{out,RF,\Re}(t)$ or $\Delta I_{out,RF,\Im}(t)$. To determine K_f from $\Delta\phi$, it is convenient to start the measurement applying low values of I_{RF} to be sure that the relationship between $\Delta\phi$ and K_f behaves like a single-valued function for a large range of values of K_f , within which an estimation of a shorter range can be subsequently performed. This means (see (2.76)) that in the first measurement, for the considered span of K_f , x is kept < 2.405 which is the first zero of $J_0(x)$. The concept just explained is illustrated in Figure 2.24 where the relationship between $\Delta\phi$ and K_f for $I_{RF} \simeq 1$ mA is shown.

The measurement reported in Figure 2.24 allows to identify a region ($\simeq [80, 200]$ MHz/mA) where the distribution of values of K_f is higher, and which is then expected to contain the value of K_f to be determined. To improve the quality of the evaluation of K_f , the current amplitude I_{RF} is changed so that (2.76) provides higher slopes of $\Delta\phi$ with respect to K_f in the interval $\simeq [80, 200]$ MHz/mA.

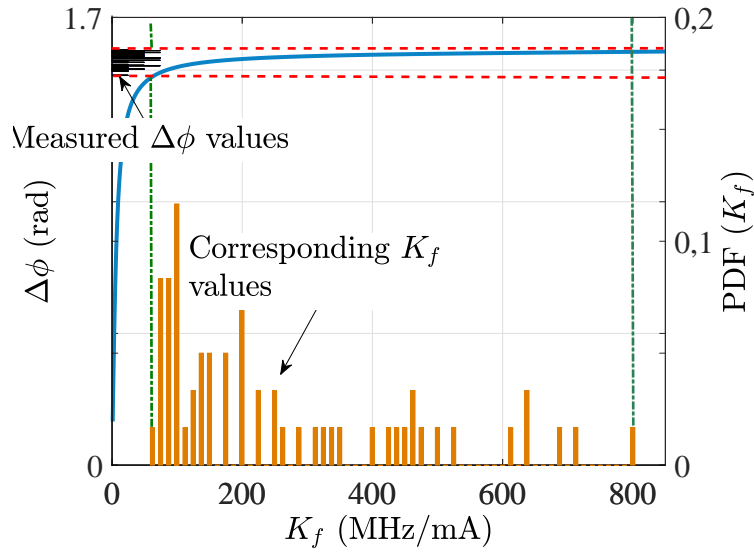


Figure 2.24: Curve $\Delta\phi(K_f)$ resulting from (2.76) for $I_{RF} \simeq 1$ mA (light blue line). The value of the modulating RF frequency is in this case $f_{RF} = 100$ MHz. Measured values of $\Delta\hat{\phi}$ are also shown (horizontal bars), together with the corresponding values of K_f (vertical bars). The values of K_f are mostly concentrated in the interval $\simeq [80, 200]$ MHz/mA. See text for details.

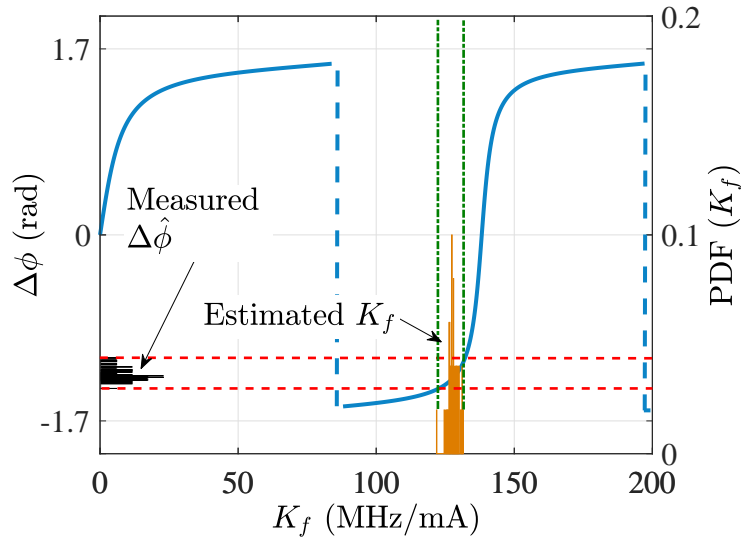


Figure 2.25: Curve $\Delta\phi(K_f)$ resulting from (2.76) for $I_{RF} \simeq 11$ mA (light blue line). The value of the modulating RF frequency is $f_{RF} = 100$ MHz. Measured values of $\Delta\hat{\phi}$ are also shown (horizontal bars), together with the corresponding values of K_f (vertical bars). The values of K_f are now concentrated in the interval around 128 MHz/mA with a standard deviation of 2.865 MHz/mA. See text for details.

In the present case, the new measurement is made by setting a value of RF current $I_{RF} \simeq 11$ mA, and the result is represented in Fig. 2.25. This choice of I_{RF} is such that the set of values of K_f corresponding to the measured values of $\Delta\phi$ are now distributed in a narrower region. This provides a great reduction of the uncertainty in the estimation of K_f which results in this case to be 128 MHz/mA with a standard deviation of 2.865 MHz/mA. Note that it would not have been possible to arrive to this result operating immediately with $I_{RF} \simeq 11$ mA, because an uncertainty between the values $K_f \simeq 128$ MHz/mA and $K_f \simeq 265$ MHz/mA (not reported in Fig. 2.25) would have been present.

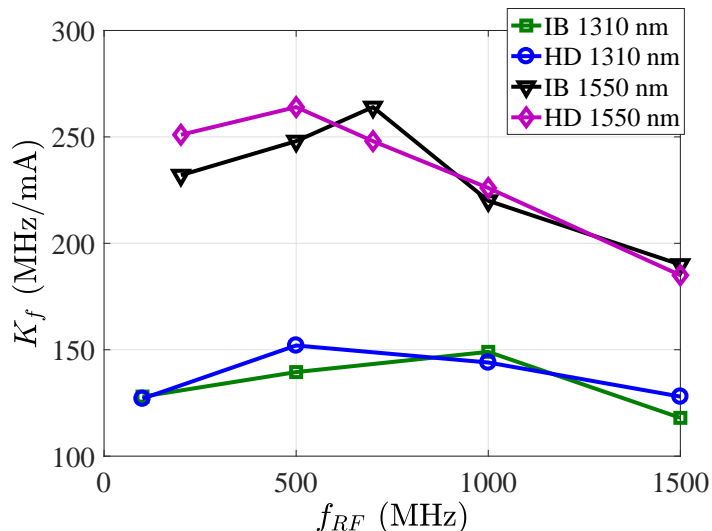


Figure 2.26: Comparison between the measured adiabatic chirp values for two lasers operating respectively in the second (1310 nm) and third window (1550 nm), both with the Interferometry-Based (IB) technique described and with the Homodyne (HD) technique, for different values f_{RF} of the modulating RF frequency.

The values of $K_f|_{IB}$ determined by the application of the present (“Interferometry Based”) method, for different values of the modulating frequency f_{RF} , are shown in Fig. 2.26.

In the same figure, a comparison with the values $K_f|_{HD}$ obtained through the above mentioned Homodyne technique is reported as well. A very good agreement with the results obtained with the two methods can be appreciated. The relative difference between the two types of measurement $\delta K_f = \frac{K_f|_{IB} - K_f|_{HD}}{0.5 \cdot (K_f|_{IB} + K_f|_{HD})}$ keeps smaller than about 4.5% for the lasers considered so far. Fig. 2.26 reports also the results of an additional DFB laser operating at 1550 nm, for which the value of K_f was determined with an approximation $\delta K_f < 5\%$ for all the modulating frequencies considered. The very good agreement between the values obtained determines a mutual validation of the two methods, and in particular proves the correctness of the Interferometry-Based technique which is here proposed. Note that the method can be applied also in the cases where ΔL is either lower or higher than the 40 mm specified in the example reported above. Introducing short patchcords before the final combiner it is indeed possible to artificially force the difference in the lengths to be within a desired range.

This gives practicability to the method e.g, when ΔL is equal to a few mm or less, in which case the determination of $\Delta\tau$ to be put in (2.76) would require from laser, photodiode and Network Analyzer the ability to operate with modulating frequencies of tens of GHz or more. At the same time, this operation can be helpful when the difference in the lengths of the fibers happens to be of the order of some meters or more, which is possible due to the fact that the length tolerances given by manufacturers can be of few percent. Indeed, although the determination of $\Delta\tau$ would not be difficult in this case, some problems would arise. First, ranging from a few hundred MHz to a few GHz, a high number of frequencies f_{RF} would meet the condition $2\pi f_{RF}\Delta\tau = m\frac{\pi}{2}$, $m = 1, 2, \dots$. Consequently, as specified at the end of Section 2, this would prevent the measurement of K_f in a relevant portion of the bandwidth investigated. Moreover, if the difference in the lengths becomes greater than the laser coherence, this would inhibit the achievement of the interference between the signals coming from the two branches.

The system depicted in Fig. 2.21 where an additional patchcord to one or to both of the fibers inside the climatic chamber is introduced, can be described by the same mathematical model developed, where the quantities $\beta_i, \tau_i, n_{effi}, n_{gi}, \dots$ $i = 1, 2$ with their corresponding derivatives have to be intended as equivalent weight-averaged values. The application of the method adding a patchcord of length 2 m to one fiber and a patchcord of 1.65 m, (which resulted in $\Delta\tau = 1.196 \cdot 10^{-9}$ sec or $\Delta\tau = 0.80906 \cdot 10^{-9}$ sec according to the branch where each patchcord was attached) allowed to obtain the same value of K_f found in the case $\Delta L = 40$ mm, confirming the practicability of this solution.

Finally some considerations can be developed regarding the polarization state presented by the two signals before recombination, which indeed, may be different, and could lead to absence of the interferometric signal in case of perfect orthogonality between the two [113] Placing a manual fiber polarization controller between the output of one of the two fibers and the combiner, and a patchcord of appropriate length in the other branch of the interferometer, this risk can be avoided without compromising the correct application of the method, as explained above.

However, excluding the case when the signals are perfectly orthogonal already before starting the temperature variations, this insertion may result to be not necessary. Indeed, the temperature variation induces inside each branch of the interferometer a variation of the birefringence $B_i = (n_{effi\perp} - n_{effi\parallel}) L_i$, $i = 1, 2$, where $n_{effi\perp}$ and $n_{effi\parallel}$ are the effective indexes of the modes polarized along the principal states of polarization of the i -th fiber. Due to this variation a mutual polarization change between the optical fields of the two branches can take place, resulting in an envelope modulation of the interferometric signal. However, taking into account that for a few hundred meters of fiber $\frac{dB_i}{dT}$ can be estimated to be of the order of some $10^{-8} K^{-1}$ [114], it can be easily shown that this envelope modulation varies no faster than $\cos\left(\frac{\omega_0}{c} \frac{dB_i}{dT} \frac{dT}{dt} t\right)$ and exhibits then an angular velocity of the order of $10^{-4} rad/sec$. With reference to the system reported in this work $\frac{dB_i}{dT}$ was estimated around $4 \cdot 10^{-8} K^{-1}$. Similarly to what has been said with reference to the time variations of the group delays τ_1, τ_2 the effect of this mutual polarization change will not affect the correctness of the results

on the typical time scales of the measurement observations.

2.6 Summary and Discussion

A detailed mathematical model has been developed for describing the propagation in SSMF when a direct modulated VCSEL is employed. This model helps in understanding and controlling two main phenomena related to the multi-mode propagation: intermodal dispersion and modal noise. The first effect produces a detriment of the modulation response of the fiber link which is related to the different group velocity of the propagating modes, while the second one produces fluctuations of the received power due to the different phase of modes and its behavior under external stress on the fiber. The main parameters which contribute to enhance these effects have been presented and discussed. In particular, it has been pointed out the importance of the finite area of the photodiode, the connector misalignment and the frequency chirping.

Once individuated the main reasons for intermodal dispersion and modal noise, a comparison among two different techniques for mitigating those effects has been shown. The two techniques consist both in filtering the higher order mode, after or before the propagation in SSMF. It has been shown that higher advantages are obtained by employing a pre-filtering technique (input section of SSMF) compared to the post-filtering (output section of SSMF). In the first case both modal noise and intermodal dispersion are mitigated, while for the second case intermodal dispersion is mitigated but modal noise is quite enhanced.

The second part of the chapter is dedicated to the exploitation of fluctuations generated by modal noise for extracting the chirp parameters of the VCSEL single mode source. In fact, from the model is possible to individuate a clear behavior of the RF and DC output current components which is directly related to the chirp coefficients. Measuring the phase difference between these two time waveform it is possible analytically to extract such parameters. The same concept is then applied to a 1310 nm or 1550 nm DFB source. In this case the two mode propagation is created on purpose using a interferometer composed of two fibers with almost the same length.

VCSEL-SSMF-based IM-DD A-RoF for LTE applications

This Chapter aims to show a possible real application of the RoF link based on 850 nm VCSEL and SSMF. The application considered is the transmission of a single 20 MHz LTE channel operating in band 20 (800 MHz).

The Chapter is then divided in two main parts. The first one, composed of Section 3.1 and Section 3.2, aims to show the performance of the aforementioned link using a PIN photodiode as receiver. In this case, the concepts seen in the previous Chapter are applied in order to reduce the effect of modal noise and intermodal dispersion on performances.

The second part of the Chapter, composed of Section 3.3, is dedicated to the possible use of SiGe HPT as receiver compared to PIN PD. In this case, before showing the performances in LTE transmission, the photo-transistor is characterized in terms of DC and RF response, leading to the characterization of SiGe HPT with the SSMF for the first time.

Finally in Section 4.5 discussion and summary of the Chapter are given.

3.1 Performance evaluation of VCSEL-SSMF IM-DD A-RoF system for LTE applications

The experimental setup is represented in Fig. 3.1 and comprises substantially three main parts: a first one, composed by an off-line LTE frame generator and by a Vector Signal Generator (VSG), which generates an LTE signal, a second one, which is an A-RoF system transmitting such signal, and a third one, composed by a Vector Signal Analyzer (VSA) followed by an off-line LTE frame receiver, which studies the characteristics of the received signal evaluating the performances.

The core of the whole experimental bench is the A-RoF system, whose optical transmitting section consists of a directly modulated laser operating at 850 nm. In the system analyzed, the laser is a SM VCSEL, and the fiber span consists of a strand of SSMF. This means that

This chapter is based on the results published in P.2, P.7 and P.6

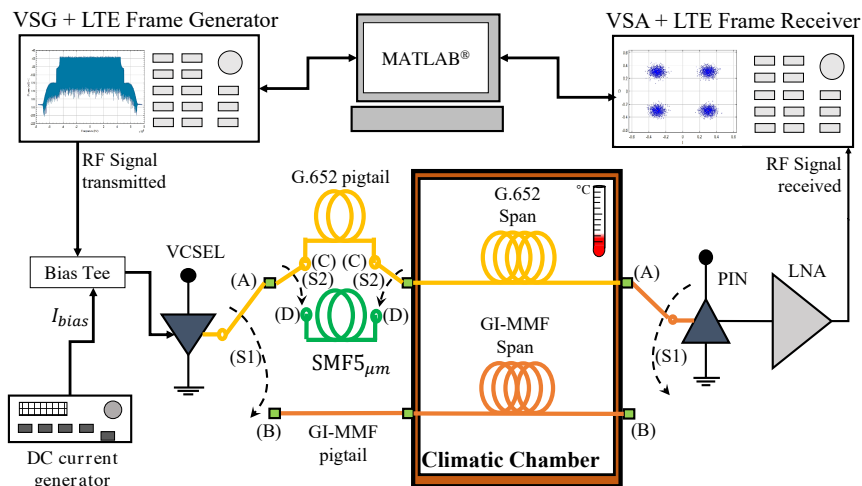


Figure 3.1: Analog Radio over Fiber systems considered and corresponding measurement setup.

the switch (S1) of Fig. 3.1 is in position (A). Another symbolical switch (S2) is represented in Fig. 3.1 to illustrate two possible configurations of the system. In the first, where (S2) is in position (C), a short pigtail of G.652 fiber connects the SM VCSEL to the G.652 strand. In the second (position (D)) the connection with the G.652 strand is obtained introducing a truly-single mode fiber at $\lambda \simeq 850 \text{ nm}$ as initial pigtail of about 3 meters. This fiber applies the pre-filtering technique explained in the previous Chapter and it will be indicated as $\text{SMF}_{5 \mu\text{m}}$. The fiber strands, either SSMF or GI-MMF, determine the link length and are placed inside a climatic chamber, where a ramp of temperature variation can be imposed. This allows to test the performances of the RoF link in presence of environmental variations, determining a statistical time variation of the Error Vector Magnitude (EVM) and the outage probability of the system. Finally, at the fiber end section, a GaAs PIN photo-detector is present, followed by a low consumption LNA. Note that no feedback loop was employed for temperature stabilization of the SM VCSEL, since the environment temperature was not undergoing sharp variations. As mentioned above, the first part of the experimental setup generates the LTE signal which is given in input to the A-RoF system. The emulated practical situation is a Frequency Division Duplexing (FDD) downlink LTE frame transmission, which is realized compliantly with the release 13 of the standard [115]. In particular, the entire frame of 10 ms duration is created offline using a locally developed MATLAB[®] software which generates the samples and then uploads them to the VSG. The VSG in turn creates the modulating signal and up-converts it to the wanted RF carrier through an internal oscillator, in order for it to be launched into the RoF link under test. The RF power $P_{RF,IN}$ of such signal can arbitrarily swept with the VSG. After the A-RoF link the signal is received by the VSA, which down-converts the received bandpass signal, making the received data available to perform an off-line post processing. This operation is again performed through an ad-hoc locally developed MATLAB[®] software, which is able to synchronize the frame, equalize the

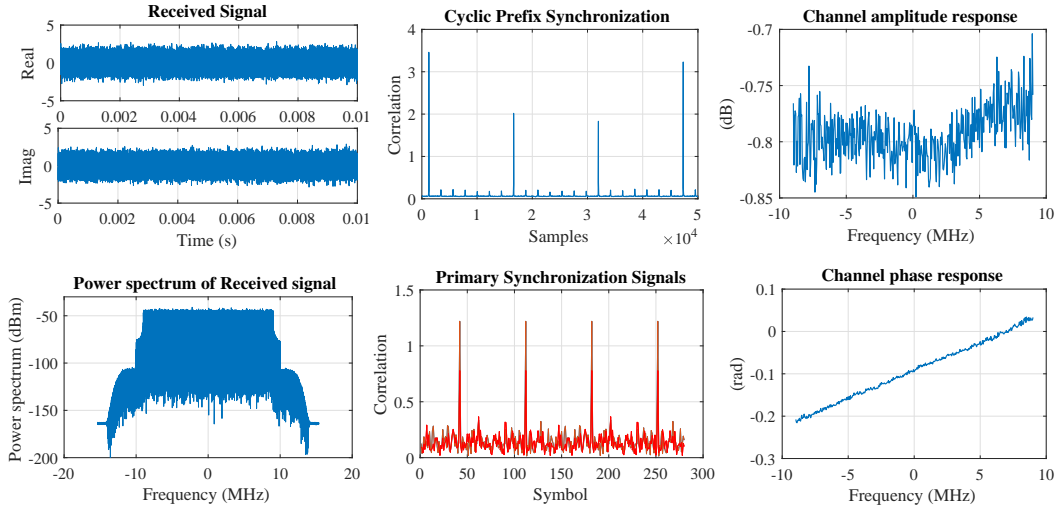


Figure 3.2: Example of information about the transmission given as output from the developed MATLAB[®] program. For more details about the program see [116].

channel and extract the EVM for each physical and logical channel of the transmitted signal. An example of information on the received signal, on the synchronization process and on the measured characteristics of the channel, given by the developed MATLAB[®] software, are shown in Figure 3.2. For more details on how the software is developed see [116].

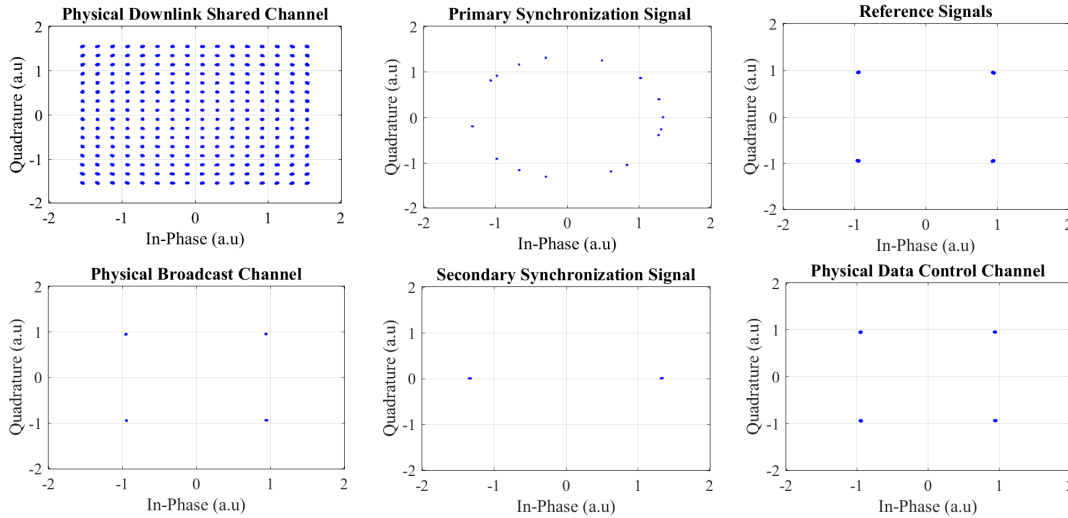


Figure 3.3: Example of constellations obtained for the LTE channels contained in the frame in case of B2B configuration taking $P_{RF,IN} = 0$ dBm and $f_{RF} = 800$ MHz.

In compliance with the LTE standard, the EVM computed through the off-line post-processing operations, is defined as follows:

$$EVM = \sqrt{\frac{\sum_k (I_k - \tilde{I}_k)^2 + (Q_k - \tilde{Q}_k)^2}{\sum_k I_k^2 + Q_k^2}} \quad (3.1)$$

where, referring to the k -th symbol, I_k , Q_k and \tilde{I}_k , \tilde{Q}_k are the phase and quadrature components of the transmitted and received k -th symbol respectively.

Figure 3.3 shows an example of received symbols on all the channels of the LTE Frame for 20 MHz bandwidth on 800 MHz carrier in B2B (i.e. VSG port directly connected to VSA port). The program has therefore been tested implementing different modulation schemes and measuring the curve EVM vs. power. For the evaluation of the performances, only the Physical Downlink Shared CHannel (PDSCH) is taken in consideration, since it contains the useful data and the higher number of symbols compared to the other channels, so that the EVM statistic results more precise. Figure 3.4 shows the behavior of EVM vs. the input power for QPSK, 16-QAM, 64-QAM and 256-QAM.

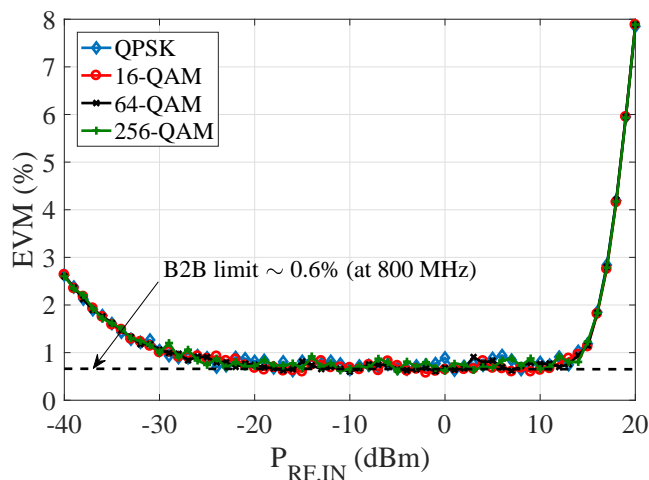


Figure 3.4: EVM evaluation versus the input RF power for different modulation schemes of 20 MHz bandwidth LTE signal centered at 800 MHz in B2B configuration.

It can be noted that the curves are overlapped each other, which suggests that the EVM in the present case is not highly dependent on the modulation scheme.

The receiver part of the A-RoF system depicted in Fig. 3.1 is composed of a GaAs PIN photodiode and a $50\ \Omega$ LNA having a gain of 20 dB and a noise figure of 2.7 dB at 800 MHz. Note that an important characteristic of the amplifier employed is that it has a relative low current consumption (30 mA), which is suitable for low cost VDN requirements.

The LTE signal chosen exhibited a bandwidth of 20 MHz and a measured Peak-to-Average Power Ratio (PAPR) of about 10.5 dB in the B2B configuration. The link characterization was performed with particular reference to band 20 of the LTE standard (frequency carrier $f_{RF} = 800\ \text{MHz}$). With reference to the A-RoF system described, the measured PAPR in band 20

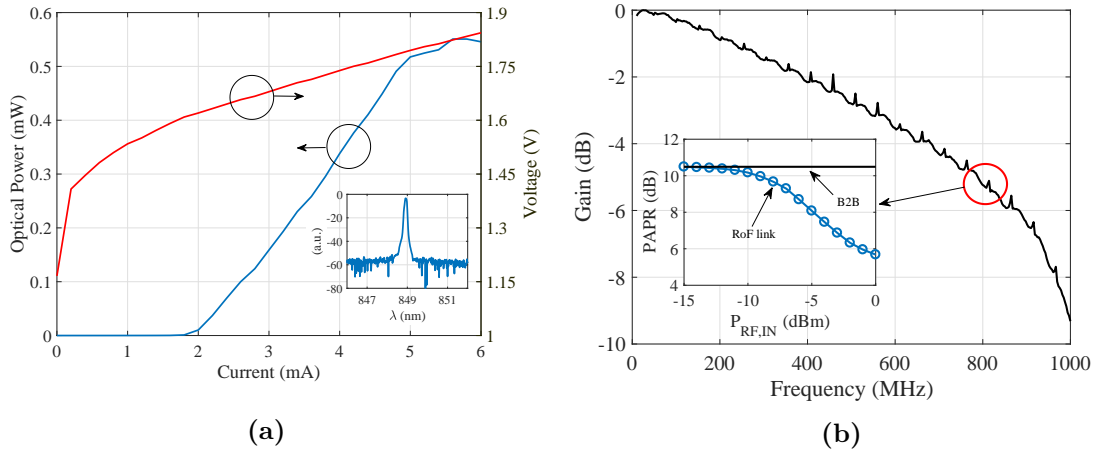


Figure 3.5: (a) L-I-V characterization and (inset) optical emission spectrum of the SM VCSEL utilized. (b) Normalized Modulation response and (inset) measured PAPR at 800 MHz of the described A-RoF system.

for different RF input powers is reported as inset in Figure 3.5b. However, its performance was also tested for other values of f_{RF} , ranging in the interval $f_{RF} \in [500, 1000] \text{ MHz}$. Indeed, this interval plays an important role in terms of applications, since it includes frequencies generally considered in LTE band 20 together with future frequencies for 5G [117, 118]. This analysis put into evidence the possible onset of critical working points of the system, and allowed to illustrate the use of the SMF_{5 μ m} pigtail represented in Fig. 3.1 as a possible solution. The SM VCSEL employed was furnished by Optowell[®]. As shown in Figure 3.5a, it presents a threshold current $I_{th} \simeq 2 \text{ mA}$ and a maximum current before the roll-off $I_s \simeq 5 \text{ mA}$. The slope-efficiency $\eta_{TX} \simeq 0.16 \text{ mW/mA}$ can be directly extracted from Fig. 3.5a.

The chosen value for the biasing current of the laser was $I_{bias} = 4.5 \text{ mA}$, since it showed to give the best EVM results in case of short distance transmission ($\simeq 1 \text{ m}$ of SSMF). Figure 3.5b shows the behavior of the SM VCSEL modulation response in correspondence to that working point. In line with the typical VCSEL characteristics, the series resistance (or differential resistance) in DC is around 50Ω for the chosen value of I_{bias} (see Figure 3.5a). This value was measured to be same also at the modulating frequencies considered, so no matching circuit was needed. Finally, the RIN of the SM VCSEL was also measured, resulting to be around -128 dB/Hz for $f_{RF} = 800 \text{ MHz}$.

As mentioned above, the usage of SSMF at 850 nm needs particular attention. In fact, it is well known that for wavelengths around 850 nm, both LP₀₁ and LP₁₁ modes propagate in the fiber in a well above cutoff fashion, exhibiting group delays per unit length respectively equal to $\tilde{\tau}_1$ and $\tilde{\tau}_2$, and giving rise to notches within the modulation bandwidth of the fiber channel, because of intermodal dispersion. Indeed, the modulation response of the fiber results to depend both on the frequency f_{RF} of the modulating RF carrier and on the length L of the SSMF span. Assuming for simplicity that the relative weight of the two modes is almost the same, taking into account the only effects of fiber attenuation and intermodal dispersion the

normalized RF power gain g is given by:

$$g = \frac{P_{RF,OUT}}{P_{RF,OUT}|_{L=0}} = 10^{-\frac{2\alpha}{10}L} \cdot \cos^2(2\pi f_{RF}\Delta\tilde{\tau}L) \quad (3.2)$$

where $\alpha = 2.4 \text{ dB/km}$ is the attenuation constant of the G.652 fiber utilized, while $P_{RF,OUT}$ is the RF power at the receiver-end of the system. The relationship expressed by Eq. 3.2 determines step reductions in the modulation response when f_{RF} and L are in the vicinity of the values which satisfy the relationship $f_{RF} \cdot L = (k + 1/2) 1/|\hat{\tau}_1 - \hat{\tau}_2|$ with $k = 0, 1, 2, \dots$

Fig. 3.6 visualizes the regions in the (f_{RF}, L) plane where, according to Eq. 3.2 and for the SSMF utilized in the present work, which features $|\hat{\tau}_1 - \hat{\tau}_2| = 2.38 \frac{\text{nsec}}{\text{km}}$, g is lower than the value of 10% taken as a reference.

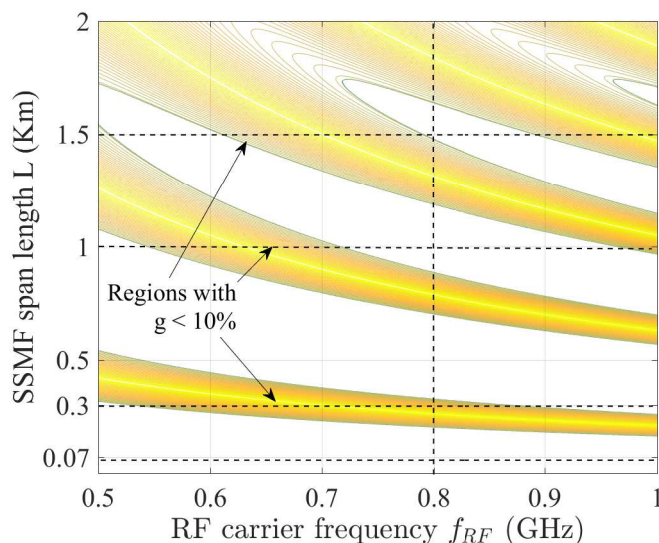


Figure 3.6: Regions where normalized RF gain g is equal or lower than 10%, as a function of frequency f_{RF} of the modulating RF carrier and length L of the SSMF span.

It can be there appreciated that in the interval $500 \text{ MHz} < f_{RF} < 1 \text{ GHz}$, for values of L sufficiently low (e. g. $L = 70 \text{ m}$) the region corresponding to the minima of g is not touched. On the contrary, for higher values of L it is possible to observe bandwidths where one or more regions are intersected. For example, for $L = 300 \text{ m}$ such bandwidth goes roughly from $f_{RF} = 550 \text{ MHz}$ to $f_{RF} = 850 \text{ MHz}$. This means that the main operating frequency here utilized ($f_{RF} = 800 \text{ MHz}$) is subjected for $L = 300 \text{ m}$ to the impairments related to the presence of a notch in the normalized RF power gain of the optical channel. These impairments actually result from a detrimental combination of intermodal dispersion and modal noise effect. Indeed, modal noise generates slow fluctuations of the received power, and, as shown in Fig. 2.7b of Chapter 2, the variance of the RF received signal due to modal noise reaches its maximum in the regions of minimum produced by intermodal dispersion.

Fig. 3.7a and Fig. 3.7b show EVM results for different values of the input RF power $P_{RF,IN}$ respectively for short range (up to 70 m) and for medium-range (from 300 m to 1500 m) link

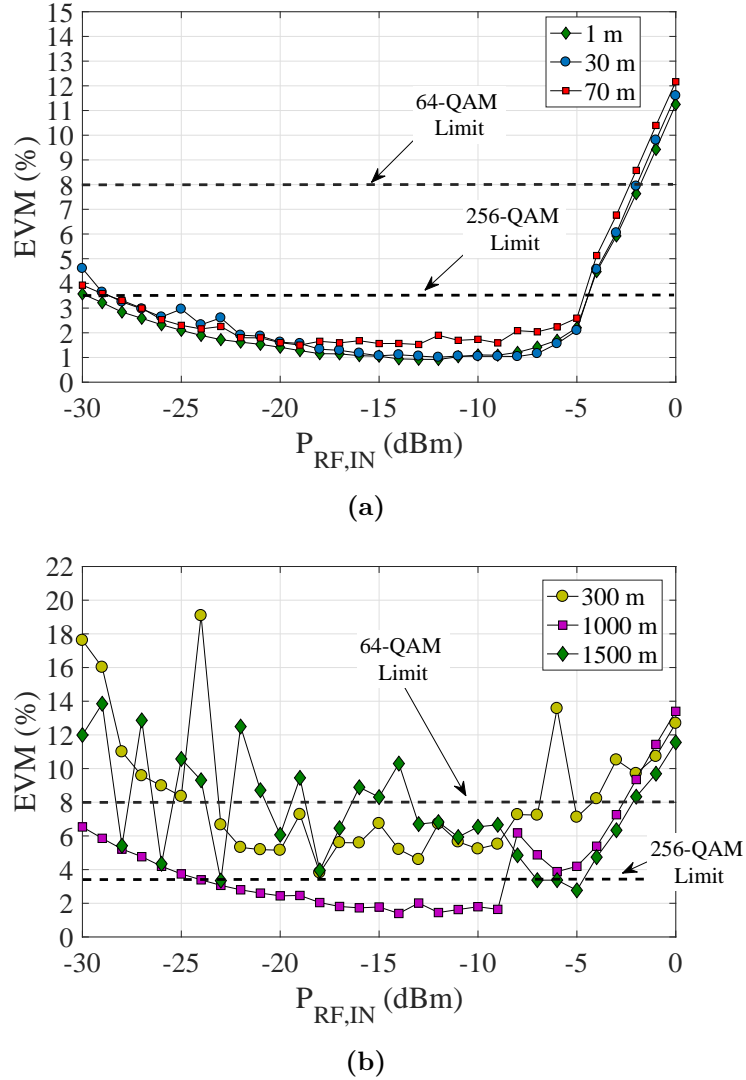


Figure 3.7: EVM Measurements of short-range (up to 70 m) (a) and medium-range (up to 1500 m) (b) A-RoF systems.

connections.

The A-RoF system utilized was the one depicted in Fig. 3.1 with the symbolical switches (S1) and (S2) in positions (A) and (C), respectively, i.e. only fiber of G.652 type is placed after the VCSEL source.

For all the lengths reported in Fig. 3.7a the performance required in [119] for 256-QAM transmission is satisfied for input RF powers up to about $P_{RF,IN} \simeq -5 \text{ dBm}$ (and up to $P_{RF,IN} \simeq -2 \text{ dBm}$ for 64-QAM). Among the medium-range distances a similar performance is observed for $L = 1 \text{ km}$, while this does not happen for $L = 300 \text{ m}$ because, as noted with reference to Fig. 3.6, at this distance the modulation frequency of 800 MHz is affected by the combined effect of intermodal dispersion and modal noise. For $L = 300 \text{ m}$ the EVM exhibits indeed an unstable behavior versus $P_{RF,IN}$ often exceeding the threshold value referred to 256-QAM and even 64-QAM transmission. Still from Figure 3.7b a similar behavior can be observed for $L = 1.5 \text{ km}$, and looking again at Figure 3.6 the behavior can be ascribed to the same physical reason adduced for $L = 300 \text{ m}$. Indeed, the point corresponding to $L = 1.5 \text{ km}$ and $f_{RF} = 800 \text{ MHz}$ results to be in the vicinity of the region where g exhibit very low values. Therefore the detriments due to the combined effect of modal dispersion and modal noise affect the received signal also in this case.

To observe the performance of the A-RoF system under environmental variations, a temperature change was forced into the climatic chamber depicted in Fig. 3.1. The input RF power was then set to $P_{RF,IN} = -9 \text{ dBm}$, since this value determined an average EVM belonging to the interval of minimum for all the lengths considered. The EVM resulting from the transmission through the A-RoF link of the 800 MHz LTE signal was monitored every 5 seconds for a total time of one hour. During this period the outage probability p_{outage_x} was computed, namely the percentage of time during which the threshold given by the LTE standard referred to the x -QAM modulation format was overtaken. For better readability of the plots, the probability of compliance $p_{comp_x} = (1 - p_{outage_x})$ will actually be represented in the corresponding figures.

Figure 3.8 confirms the good performance of the A-RoF system for short ($L = 70 \text{ m}$) link lengths, as well as the not acceptable quality of the received signal for the length $L = 300 \text{ m}$. In correspondence to $L = 70 \text{ m}$, and to $L = 300 \text{ m}$, it was respectively computed $p_{comp, 256} = 99.86\%$ and $p_{comp, 256} = 0\%$.

3.2 Performance of the A-RoF system adopting the pre-filtering technique

As already mentioned, the adoption of the pre-filtering technique in the present work corresponds to the one which results from Fig. 3.1 when the symbolical switches (S1) and (S2) are put in positions (A) and (D), respectively. As explained in Chapter 2, the main effect of this introduction is to excite within the G.652 fiber mostly the LP_{01} mode, reducing to a minimum the presence of the LP_{11} mode, and reducing consequently the combined effect of modal noise and intermodal dispersion as well.

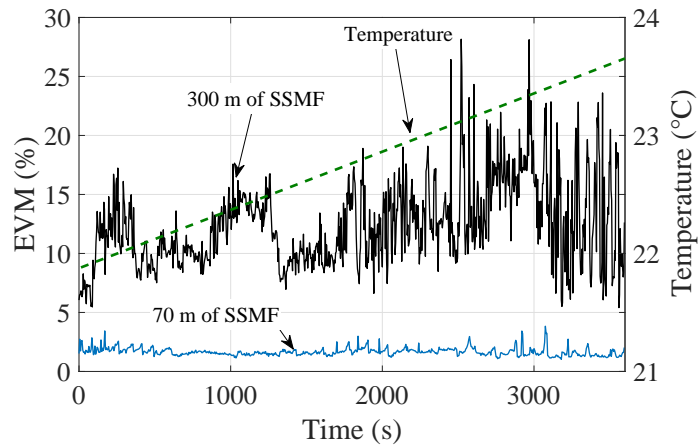


Figure 3.8: Time measurement of EVM for 70 m and for 300 m of SSMF with $P_{RF,IN} = -9 \text{ dBm}$ at 800 MHz, utilizing the A-RoF link depicted in Fig. 3.1 with the symbolical switches (S1) and (S2) in positions (A) and (C), respectively. This corresponds to the case in which only the SSMF is present along the link. The fiber has been inserted in the climatic chamber where the temperature changed with a linear ramp as indicated with the dashed line. The EVM was computed every 5 seconds within a total time interval of one hour.

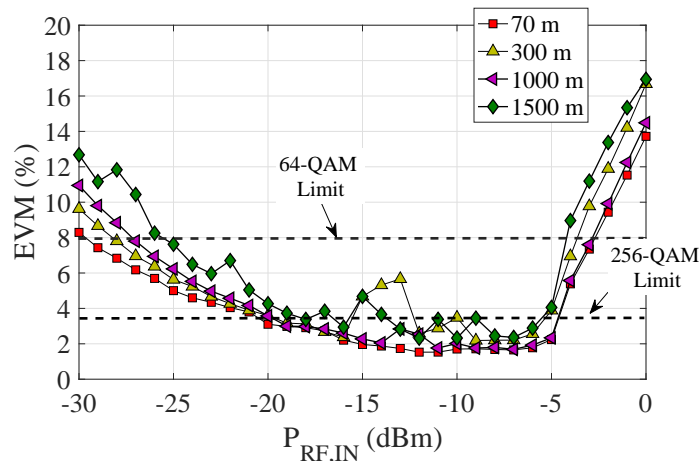


Figure 3.9: EVM Measurements for all the distances considered inserting the $\text{SMF}_{5\mu\text{m}}$ before each SSMF span.

Figure 3.9 allows to appreciate that, excluding a little increase ($\simeq 3$ dB of optical insertion loss) in the lower bound of $P_{RF,IN}$, due to the insertion loss of the $SMF_{5\mu m}$ patch, the performance of the links with $L = 70$ m (representative also for lower L values) and $L = 1$ km is substantially not changed. On the contrary, in the case when $L = 300$ m a great improvement can be observed, since a compliance with the LTE standard can be appreciated in almost all the range considered for $P_{RF,IN}$ at 64-QAM, and in the range -12 dBm $\leq P_{RF,IN} \leq -5$ dBm at 256-QAM.

Similar considerations can be taken also for $L = 1.5$ km, even if a less regular behavior seems to be present in this case with respect to the $L = 300$ m case. This is due to the fact that although the introduction of the $SMF_{5\mu m}$ patch leads to a reduction of the effects of intermodal dispersion and modal noise, fiber attenuation for $L = 1.5$ km (already taken into account in Fig. 3.6), and insertion loss of the $SMF_{5\mu m}$ patch reduce the signal to noise ratio to lower levels with respect to the $L = 300$ m case. Measurements performed over distances $L > 1.5$ km led to worse results, suggesting that $L \sim 1.5$ km can be taken as a reliable reference point for the upper limit of the possible distances to be covered.

Referring now to the 1-hour monitoring of the received LTE signal under forced temperature variations, Figure 3.10 allows to appreciate the improvement generated by the insertion of the $SMF_{5\mu m}$ for $L = 300$ m and $f_{RF} = 800$ MHz. The value of the quantity $p_{comp,64}$ passed from 8% to 100%, while $p_{comp,256}$ passed from 0% to 89%.

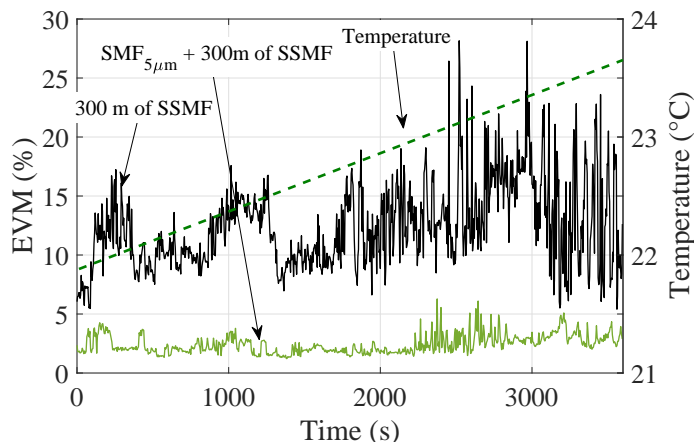
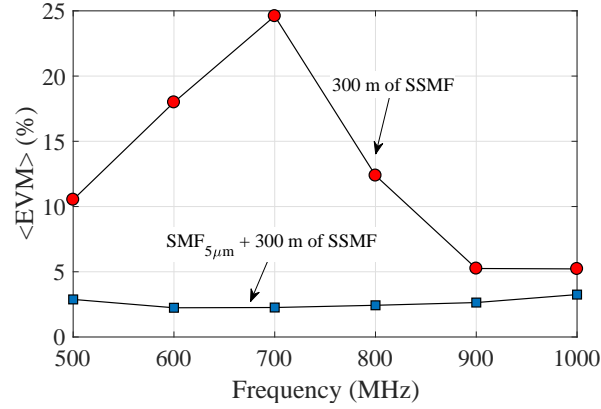


Figure 3.10: Example of EVM time measurements for 300 m of SSMF with $P_{RF,IN} = -9$ dBm at 800 MHz. Both cases in which the $SMF_{5\mu m}$ is present (green curve) and is not present (black curve) are shown. The temperature ramp is also indicated.

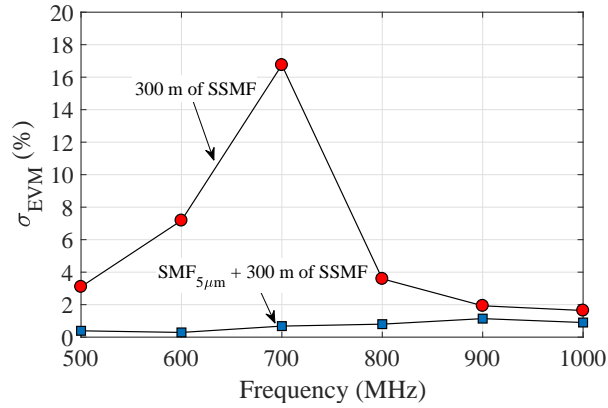
In line with what was observed above, for $L = 70$ m no particular performance variations were instead observed. Indeed, the values of $p_{comp,64}$ and $p_{comp,256}$ passed respectively from 100% and 99.86% to 100% and 100%.

As mentioned above, to better highlight the performance of the proposed A-RoF system for $L = 300$ m, frequencies ranging in the interval 500 MHz $\leq f_{RF} \leq 1$ GHz were considered. Figures 3.11a and 3.11b report respectively the mean value and the standard deviation of the

measured EVM within such interval.



(a)



(b)

Figure 3.11: (a) Average value of EVM for $L = 300\text{ m}$ and $P_{RF,IN} = -9\text{ dBm}$. The beneficial effect of inserting the $\text{SMF}_{5\mu\text{m}}$ patch is also shown. The same effect is shown for the EVM standard deviation (b).

The improved performance of the proposed system can be appreciated at 800 MHz , where the mean EVM goes from 12.38% to 2.43% , and is maximum at $f_{RF} = 700\text{ MHz}$ where the value goes from 24.6% to less than 2.26% . Figure 3.11b highlights that the maximum improvement of σ_{EVM} is obtained for 700 MHz , passing from 16.75% to 0.68% , while for 800 MHz σ_{EVM} reduces from 3.59% to 0.8% . Figure 3.12 allows to appreciate the performance of the proposed A-RoF system in terms of $p_{comp,256}$. It can be noted that for 800 MHz $p_{comp,256}$ goes from 0% to 89% , while for 600 MHz it exhibits the greatest improvement, going from 0% to 99.86% . Qualitatively similar results have been found for $p_{comp,64}$, which reaches in the proposed case the value of 100% for all the frequencies considered.

Although the present analysis has been focused on the case $L = 300\text{ m}$, note that the concept on which the presented solution is based has a general applicability, and can therefore be successfully utilized within different sets of frequency intervals and short-medium range link lengths, as can be desumed from Fig. 3.6 reported above.

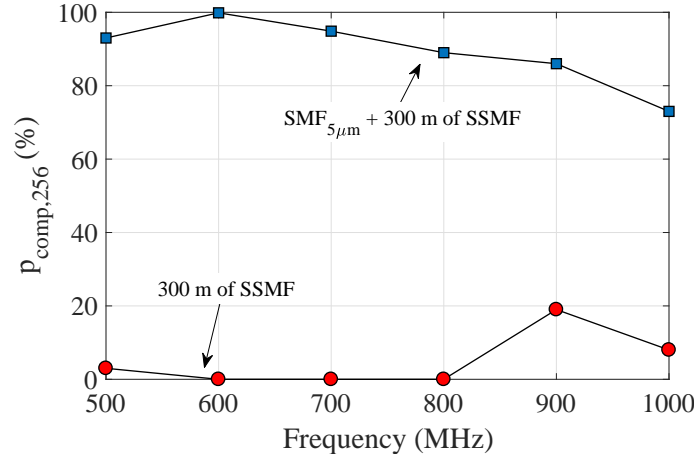


Figure 3.12: The graph represents the outage probability for 256-QAM transmission without (circles) and with (squares) the insertion of the SMF_{5μm}.

Comparison with GI-MMF A-RoF systems based on VCSELs

The purpose of this subsection is to give a whole view about the employment of 850 nm VCSELs in A-RoF systems for short and medium range MFH applications. The performances of the SSMF-based RoF system proposed have been compared with a system which employs the same SM VCSEL and GI-MMF instead of SSMF. Moreover, a further comparison using MTM VCSEL and GI-MMF is presented allowing to have a comparison with common systems employed in several short-medium range telecommunication links.

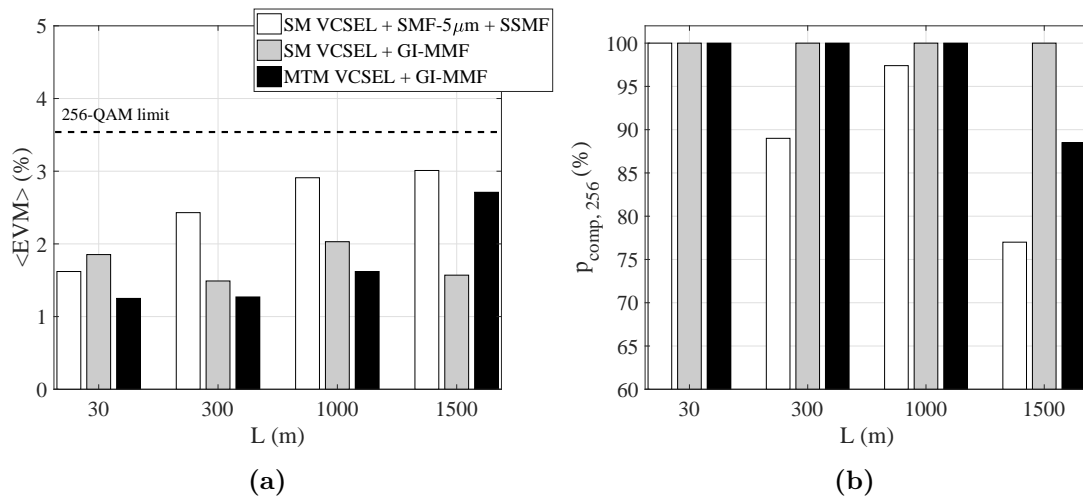


Figure 3.13: Average EVM (a) and 256-QAM compliance probability (b) for RoF link based on SM VCSEL, SMF_{5μm} and SSMF (white), SM VCSEL and GI-MMF (grey), MTM VCSEL and GI-MMF (black).

Figures 3.13a and 3.13b show the trend of average values of EVM and $p_{\text{comp},256}$ for the

three different configurations considered varying the link distances. Note that, the 20 MHz bandwidth LTE signal used in this work is the maximum admitted bandwidth for a single LTE channel. Indeed, due to the bandwidth size, this represents the worst case of Signal-to-Noise Ratio when a certain $P_{RF,IN}$ is fixed.

Focusing initially on the two systems based on GI-MMF, it can be noted that they practically exhibit the same performance for $L \leq 1000$ m. Indeed, the differences in the EVM values smaller than one percentage point can be easily met with either sign due to the not perfect reproducibility of the optical connections. However, for higher distances (such as 1500 m) the system composed by SM VCSEL + GI-MMF performs better than the one composed by MTM VCSEL + GI-MMF. This fact can be related to the effect of intermodal dispersion and chromatic dispersion which both become relevant in presence of multimode lasers such as the MTM VCSEL employed.

Note also that the proposed system (SM VCSEL + SMF_{5 μ m} + SSMF) exhibits slightly lower performances with respect to the other two based on GI-MMF. This is due to the fact that the MTM and SM VCSELs were commercially designed to be efficiently coupled respectively with a GI-MMF and with a 9 μ m-core SSMF (and consequently also with a GI-MMF). Therefore, while our proposed insertion of a smaller core diameter fiber (such as the SMF_{5 μ m}) right before the SSMF span gives the described advantages, it also produces an optical coupling loss, which increases the Noise Figure of few dB of the global system ending up in higher values of the average EVM/lower values of $p_{comp,256}$.

Indeed, the mis-coupling is not present in the other two cases where the VCSELs are directly coupled with fibers with diameter equal or higher than the one for which they are designed.

As a matter of fact, a further margin of improvement in the performance of the proposed solution (SM VCSEL + SMF_{5 μ m} + SSMF) can be reasonably envisaged, provided that a SM VCSEL source is utilized which features an optimized coupling with optical fibers with 5 μ m core diameter.

In this view from Figure 3.13a it can be concluded that the A-RoF system proposed allows the transmission of 256-QAM signals in compliance with the requirements of the LTE standard since the average value of EVM falls in all cases below the given upper limit. More in general, both Figures 3.13a and 3.13b demonstrate that the usage of G.652 fiber can lead to performances near to GI-MMF for both the quantities considered showing that the proposed solution can represent the optimal one in terms of performance-to-cost ratio in those cases where a SSMF infrastructure is already available.

3.3 Use of SiGe HPT in VCSEL-SSMF-based RoF link

This Section aims to introduce in the VCSEL-SSMF-based RoF link presented up to now the SiGe HPT as opto-electronic receiver. This fact constitutes a novelty for SiGe HPT, in fact since the wavelength bandwidth of the responsivity of this device is generally at low wavelength (because of the Silicon bandgap), the device has been characterized exclusively with 50 μm diameter MMF.

Therefore, a characterization of the SiGe HPT coupled with a 9 μm diameter fiber has been performed and it is shown hereafter, concluding with the performance evaluated in terms of EVM.

DC Characterization

The DC characterization presented here intends to show the behavior of the devices in terms of Responsivity. This quantity is defined as follows:

$$\mathcal{R} = \frac{I_c - I_{c,dark}}{P_{opt}} \quad (3.3)$$

in which P_{opt} is the optical power injected in the window surface of the HPT, I_c is the total collector current measured and $I_{c,dark}$ is the collector current measured in absence of light when it is biased.

To be able to measure this quantity, the experimental setup employed is shown in Figure 3.14.

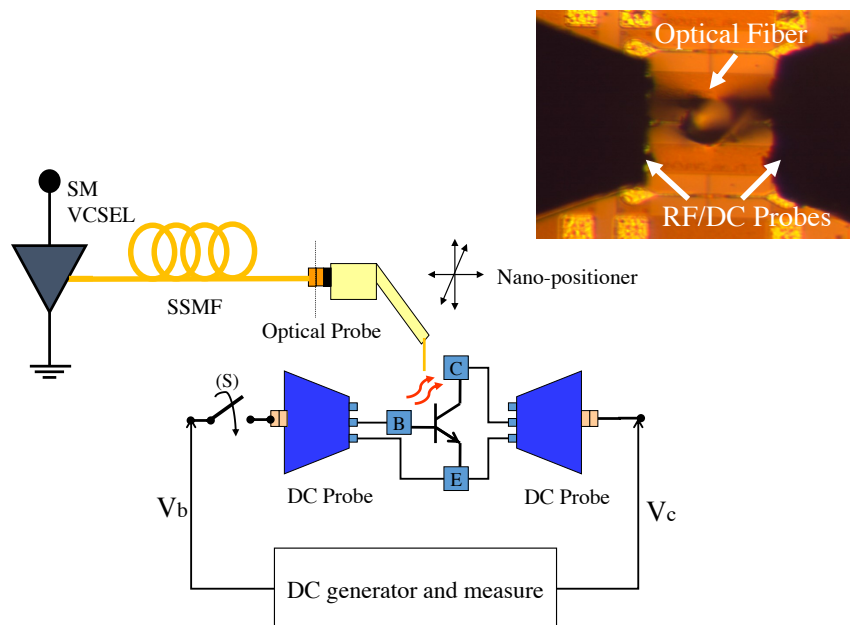


Figure 3.14: Experimental setup for HPT characterization.

The experimental setup consists in the single mode VCSEL operating at 850 nm employed also in previous part of the Chapter, coupled to a SSMF optical probe which injects directly

light to the top of HPT. The device is electrically biased using the Agilent B1500 DC current generator which is also able to measure the current/voltage when voltage/current is applied. As inset of Figure 3.14, the picture acquired by the microscope shows the RF/DC probes and the optical fiber from the top view. This setup allows also to scan the device in the spatial domain through a technique called SNOM. Figure 3.15 shows the Gummel plot together with the Responsivity as function of V_b . From this Figure it is possible to see that the responsivity increases with the same trend as β . For $V_b \leq 0.6$ the device acts as photo-detector, since the applied voltage is not enough to reach the transistor effect, and the device still performs as a diode. The maximum responsivity is found to be around $\mathcal{R} \simeq 0.4$ A/W which is in agreement with the measurements performed using MMF [80]. As mention in Section 1.3, these two conditions are called PD mode and HPT mode, respectively.

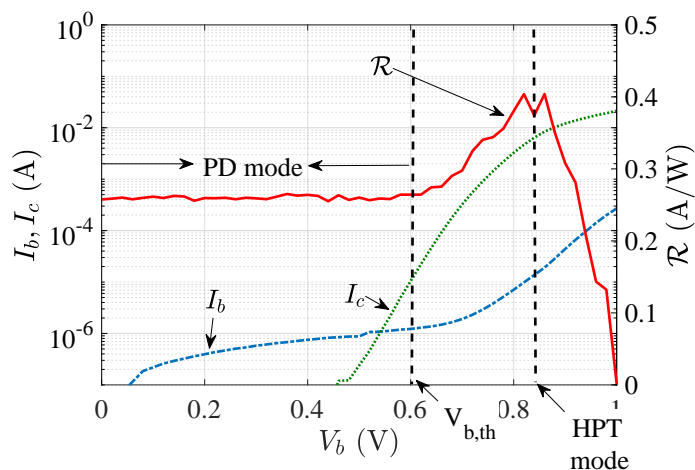


Figure 3.15: Gummel plot under dark condition and example of Responsivity of the considered SiGe HPT for $V_c = 2$ V and $P_{opt} = 0.34$ mW.

Interesting considerations can be drawn from the Gummel plot under light injection as shown in Figure 3.16. As expected the collector current I_c increases its value due to the photo-current created. Regarding I_b the absolute value is plotted since the negative current produced by the light injection.

Two important considerations can be made. Firstly, the value of the absolute current does not reach the same value of I_c . The reason, as mentioned in Chapter 1, is related to the substrate contribution in Silicon-based HPT. Secondly, $|I_b|$ presents a notch in correspondence of a particular value of base voltage V_b . In that point, the total current I_b pass from negative to positive values. This phenomenon is related to the self-biasing effect that is present in the device under light injection. This means that, depending on the power intensity, the base voltage for which there is current inversion $V_{b,inv}$ is expected to increase with the light intensity. However, as it is shown in Figure 3.17, $V_{b,inv}$ saturates at 0.8 V after $P_{opt} \simeq 0.2$ mW.

The curve of responsivity shown above refers to a specific value of optical power injected. It is therefore interesting to analyze the behavior for different power levels. To do that,

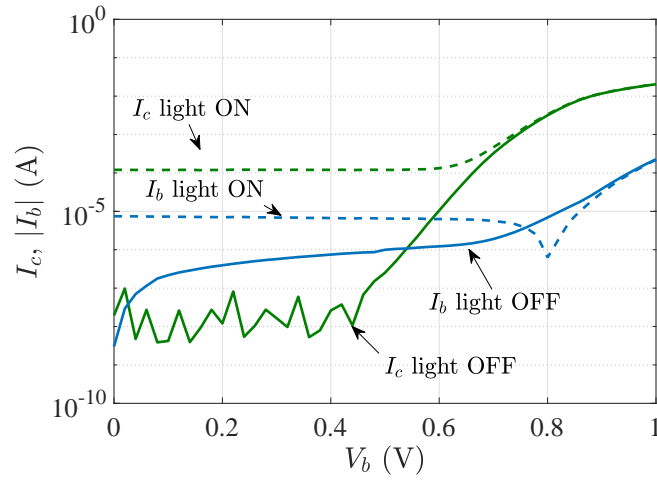


Figure 3.16: Gummel plot with light ON ($P_{opt} = 0.34$ mW) and light OFF of the considered SiGe HPT for $V_c = 2$ V.

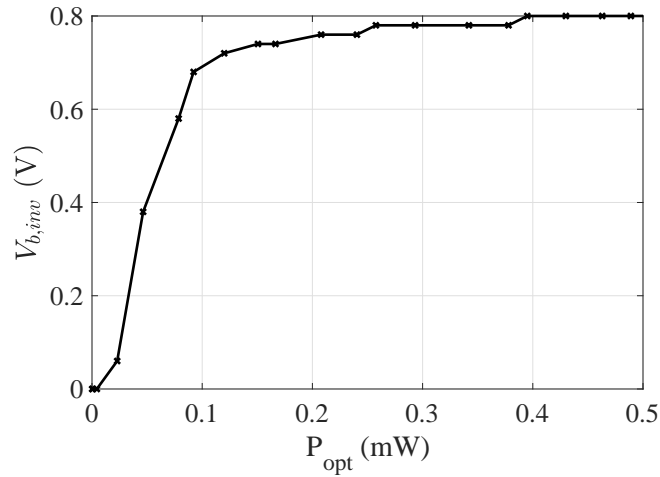


Figure 3.17: Computation of the values of $V_{b,inv}$ in which the base current is null ($I_b \simeq 0$ A).

the current bias of the single mode laser employed has been changed producing levels of optical power P_{opt} from 0.1 mW to 0.5 mW. This range of values is indeed intended to be related to the application study made in this chapter. Figure 3.18 shows the behavior of the responsivity varying the optical power for PD mode and HPT mode. It can be observed that the responsivity reaches its maximum around $P_{opt} = 0.15$ mW for both configurations, while for higher power the responsivity starts to decrease. This effect can be explained if we consider power saturation of the device.

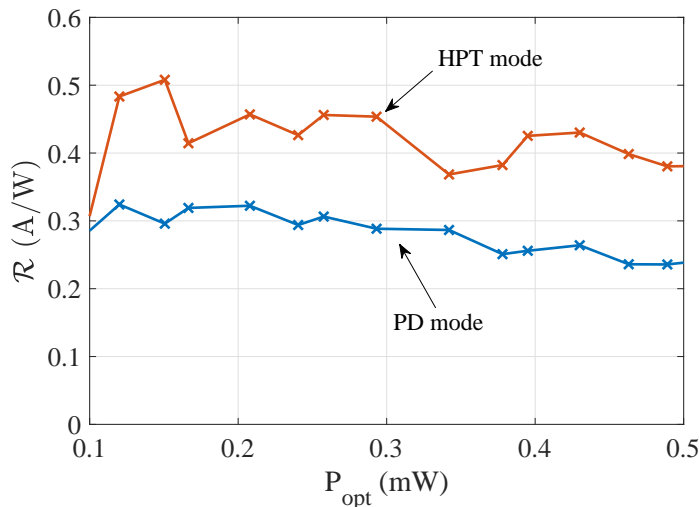


Figure 3.18: Responsivity as function of P_{opt} for HPT and PD mode

Similar characterization and consideration can be made for the device operating in 2T mode (i.e. unconnected base terminal). Figure 3.19 shows the behavior of the responsivity for different levels of V_c as function of optical injected power. This modality shows indeed much higher responsivity confirming the results obtained in [76].

Moreover, a SNOM measure has been performance in order to evaluate the effect of the substrate in case of light injection from SSMF of 9 micron diameter. In the Figure 3.20, the base and collector current on both PD and HPT mode are shown, together with the absolute responsivity in both configurations.

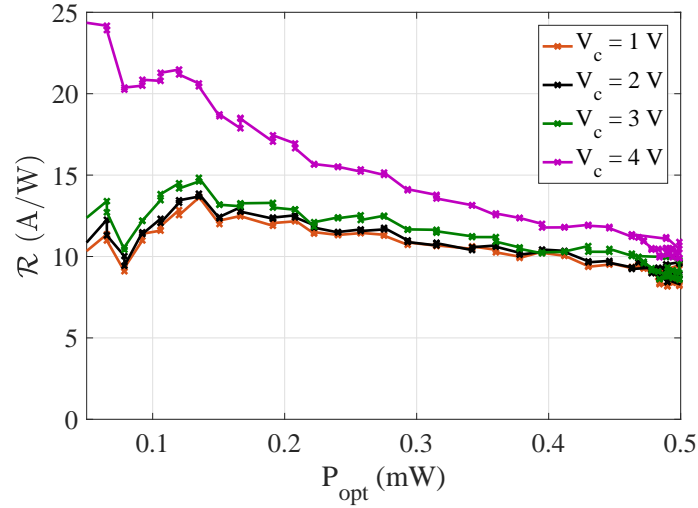


Figure 3.19: Responsivity as function of P_{opt} for 2T mode varying the collector voltage V_c .

The substrate effect is then computed. From Figures 3.21 it is possible to observe the effect of the substrate current which is present around the HPT but also in the center leading to a maximum value of $R_{sub} = 0.3$ A/W. The corresponding intrinsic responsivity of HPT and PD mode are also computed. This fact represents a difference with respect to the case of MMF shown in [76]. This fact can be related to the higher density of power provided by SSMF. However this assumption needs to be validated in future works.

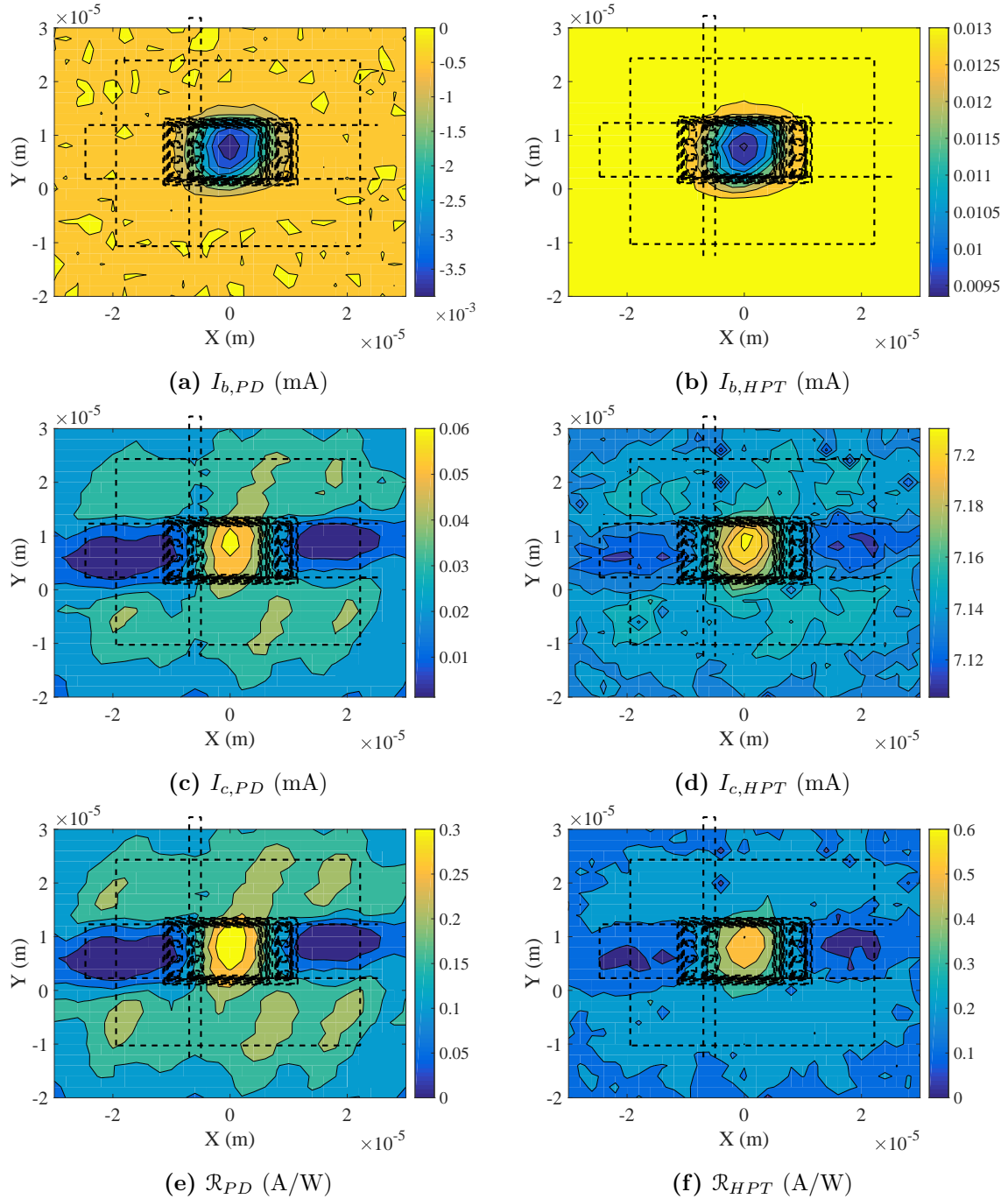


Figure 3.20: SNOM measurement of $I_{b,PD}$, $I_{b,HPT}$, $I_{c,PD}$, $I_{c,HPT}$ and computation of \mathcal{R}_{PD} , \mathcal{R}_{HPT} of the SiGe HPT with $P_{opt} \simeq 0.18$ mW.

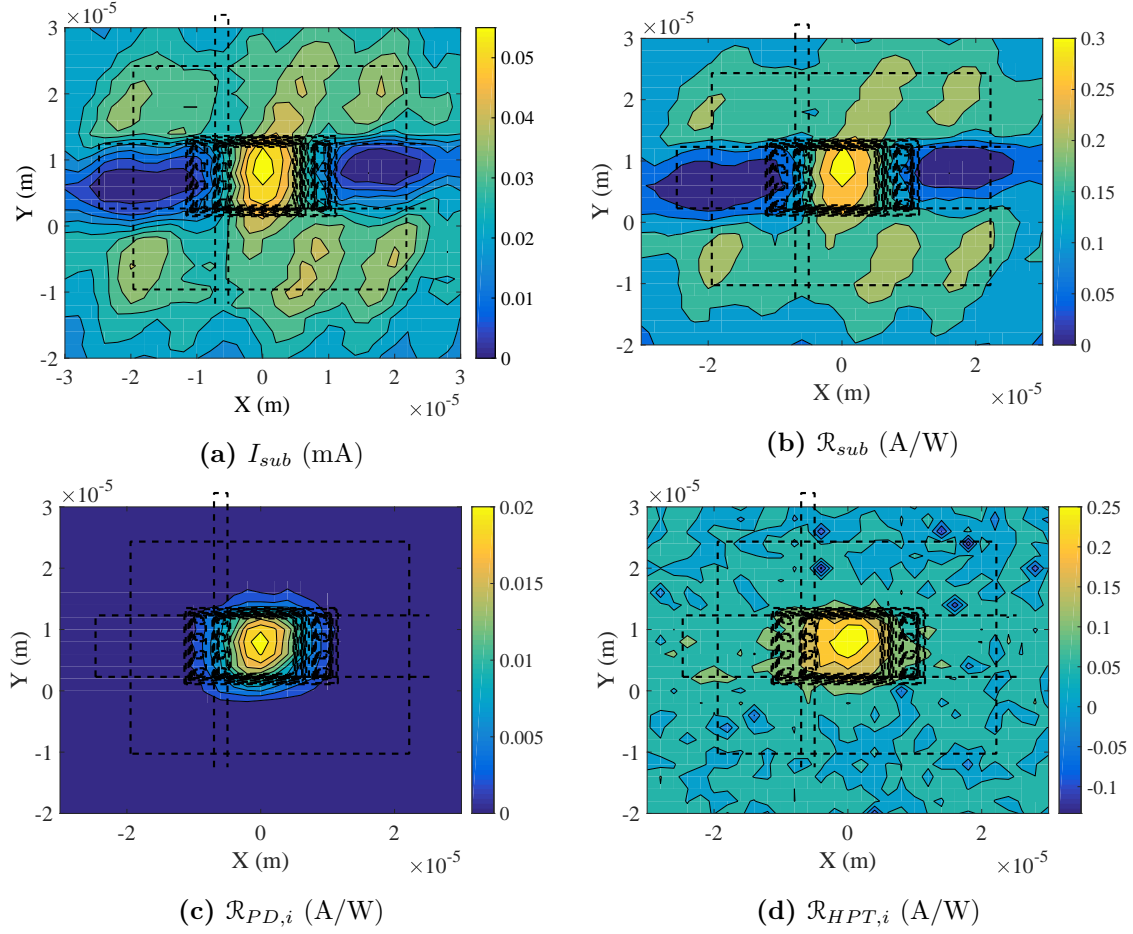


Figure 3.21: Computation of I_{sub} , \mathcal{R}_{sub} and $\mathcal{R}_{PD,i}$, $\mathcal{R}_{HPT,i}$ with $P_{opt} \simeq 0.18$ mW

RF characterization

To characterize the HPT in RF domain the experimental setup utilized is shown in Figure 3.22. The switch (S) enables the transition between 2T and 3T modes. The radio frequencies vary from 10 MHz to 2.5 GHz since they are of interest for the target applications (e.g. LTE and 5G). The HPT is on chip and is utilized exploiting a probe station.

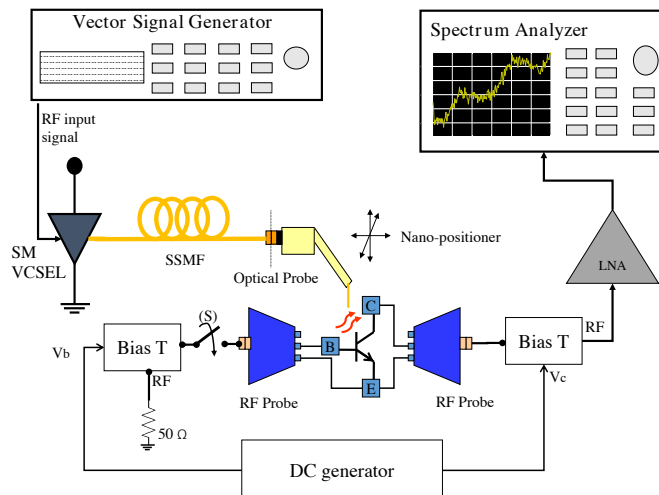


Figure 3.22: RF measurement experimental bench.

The RF characterization consisted in both gain and noise measurements. Note that in order to perform noise measurements, a 40 dB Gain LNA has been utilized right before the VSA in order to decrease the high noise figure at the receiver side NF_{RX} given by the VSA. In particular exploiting the Friis formula it becomes:

$$NF_{RX} = NF_{LNA} + \frac{NF_{VSA} - 1}{G_{LNA}} \quad (3.4)$$

The 40 dB gain of the LNA makes the contribution of NF_{VSA} (which is measured to be around 20 dB) negligible leading to $NF_{RX} \simeq NF_{LNA} \simeq 3$ dB. The noise figure and the gain of the LNA have been first measured for all the frequency range and a subsequent de-embedding of the observed results has been performed to finally extrapolate the noise of the optical link. As explained in detail in [120], for an opto-microwave metrics, in order to design properly the system and understand the contribution of each component on the performances. In particular, it is possible to define the Opto-Microwave Gain G_{OM}^{HPT} of the HPT as

$$G_{OM}^{HPT} (dB) = 20 \log_{10}(\mathcal{R}) \quad (3.5)$$

This value represents the contribution in terms of RF gain of the HPT on the link. In fact, considering perfect matching, the RF gain of the opto-electronic link can be expressed as:

$$\begin{aligned}
 G_{OM}^{link}(dB) &= 20 \log_{10} \left(\frac{\eta_{TX} \mathcal{R}}{2A_{opt}} \right) = \\
 &= 20 \log_{10}(\eta_{TX}) + 20 \log_{10}(\mathcal{R}) + 20 \log_{10} \left(\frac{1}{2A_{opt}} \right) \\
 &= G_{OM}^{LD}(dB) + G_{OM}^{HPT}(dB) + G_{OM}^{Fiber}(dB)
 \end{aligned} \tag{3.6}$$

in which the opto-microwave quantities related also to laser and fiber have been defined.

Figure 3.23 shows the comparison of the opto-microwave gain as a function of frequency of the HPT under its three configuration modes and the reference PIN photo-detector. The level of the injected optical power is the same in all cases, and the value of the base-collector voltage in the three modes of the HPT is also the same. It can be observed that in 2T mode G_{OM}^{HPT} decreases rapidly crossing the HPT mode curve around 800 MHz. In the other two operating modes, instead, the curves decrease less sharply in frequency. This fact lets the use of phototransistor be dependent on the application frequency band considered, suggesting that different operating modes must be chosen depending on the operating RF frequency.

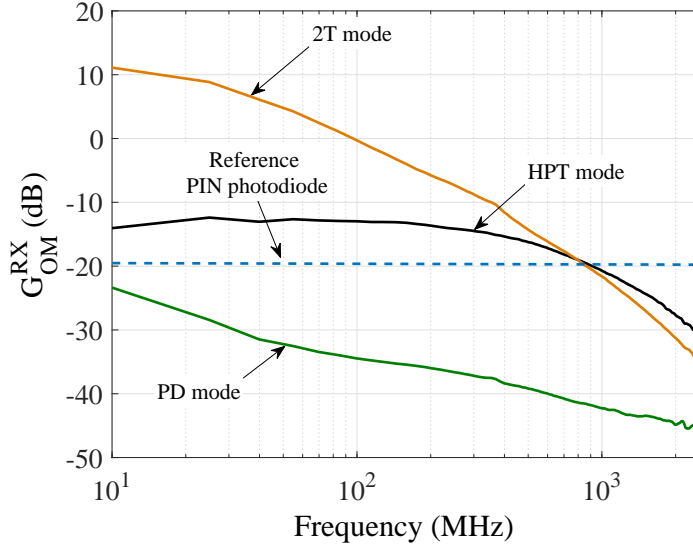


Figure 3.23: Opto-Microwave Gain (G_{OM}^{HPT}) of the three configurations of HPT and of the reference PIN photodiode.

In optical communication links the Noise Spectral Density (NSD) can be expressed as function of the parameters of the optical components involved. In particular, in absence of amplifiers, neglecting the fiber attenuation and considering a perfect matching network, the NSD can be written as:

$$NSD = R_L \left[RIN \cdot \frac{P_{opt}^2 \mathcal{R}^2(f_{RF})}{4} + 2q \frac{P_{opt} \mathcal{R}}{4} + \frac{kTF}{R_L} \right] \tag{3.7}$$

in which R_L is the impedance load (50Ω), q is the electron charge, RIN is the Relative Intensity Noise, $\mathcal{R}(f_{RF})$ is the frequency response of the detector responsivity, k is the Boltzmann's constant, $T = 290 \text{ K}$ is the reference temperature and F is the noise figure of the LNA. This equation put in evidence the dependence of the noise on frequency and optical power received for which regards the first term of the right side of equation (3.7). Note that, instead, the second term on the same side (shot noise term) is independent on frequency.

NSD of the three operating modes is shown in Figure 3.24 with respect to frequency. The NSD is lower in PD mode than the other two modes i.e. HPT and 2T mode of operation. This can be explained by the internal amplification behavior of the HPT in HPT and 2T mode operation that can also amplifies the noise level of the device. Whereas in PD mode, as there is no internal amplification of the device, the noise level is very low, resulting in only shot noise contribution. The NSD is very high at lower frequency due to typical effects present in HBT such as $1/f_{RF}$ and generation recombination noise [121] and decreases as the frequency increases in the three operation configurations. The NSD in 2T configuration is the highest at low frequency compared with 3T configurations (HPT and PD mode). This is because the base terminal is open (i.e. infinite resistance) in a 2T configuration and hence the photo-generated holes are blocked at the base-emitter junction as the recombination process is dominating compared to other configurations. Therefore, at low frequency, the generation-recombination noise is dominating in 2T mode. However, at high frequency this influence is filtered out and the impact of internal amplification on the NSD in HPT mode becomes visible and dominant on the NSD produced in 2T mode.

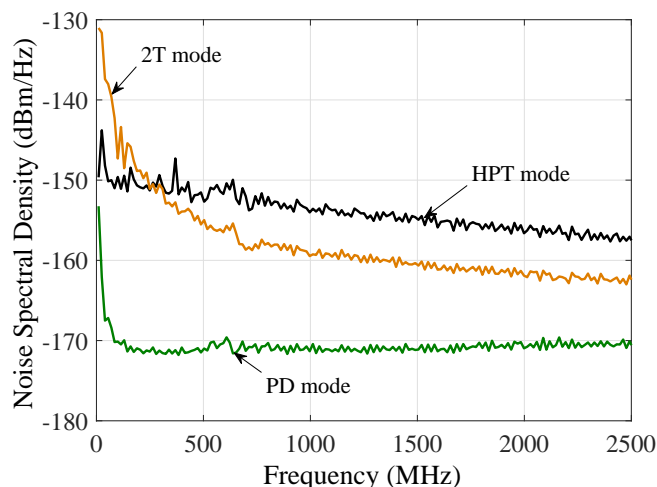


Figure 3.24: Comparison of NSD of the three different configurations for a fixed level of $P_{opt} = 0.34 \text{ mW}$ and $V_c = 2 \text{ V}$.

From the NSD of the link and G_{OM}^{HPT} it is possible to extrapolate the noise figure of the HPT and evaluate the impact of the HPT on the system. To be able to do this, the opto-microwave noise figure concept defined in [120] will be exploited. In this way, it is possible to separate the noise contributions of each component of the link: laser, fiber and photo-

detector, considering them as equivalent microwave components. In particular, defining the relative opto-microwave noise figure NF_{OM}^{LD} as follows:

$$NF_{OM}^{LD}(f) = 1 + \frac{P_{opt,RX}^2 \cdot RIN \cdot R_L}{G_{OM}^{LD}(f) \cdot kT} \quad (3.8)$$

it is possible to exploit the following formula to extract the contribution of the HPT in terms of opto-microwave noise figure NF_{OM}^{HPT} [120]:

$$NF_{OM}^{HPT} = \left(NF_{OM}^{link} - NF_{OM}^{LD} \right) G_{OM}^{LD} + 1 \quad (3.9)$$

in which NF_{OM}^{link} is the total noise figure of the optical link (without considering the amplifier) defined as:

$$NF_{OM}^{link} = \frac{NSD}{kTG_{OM}^{link}} \quad (3.10)$$

Equation 3.9 is applied assuming that the attenuation produced by the optical fiber is negligible in the case considered. To measure G_{OM}^{LD} the reference PIN photo-detector has been used. Figure 3.25 shows the computed curves of NF_{OM}^{HPT} in the three configurations and the opto-microwave noise figure of the PIN photodiode NF_{OM}^{PIN} , from measurements.

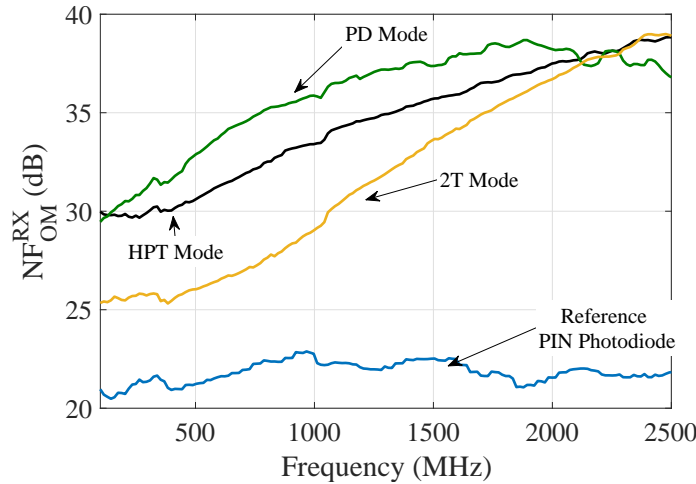


Figure 3.25: Opto-microwave noise figure of the HPT detector in the three operating modes compared with the opto-microwave noise figure of the reference PIN photo-detector, from measurements.

The results put in evidence the real impact on the SNR of the SiGe HPT. 2T mode results to be the best configuration in terms of noise figure up to about 2.3 GHz. The higher gain of 2T compensates the high NSD (see Figure 3.24) since increases the gain at low frequency. However, increasing the frequency the gain diminished, due to crowding effects in the active region which slow down the time for the holes to reach the emitter and electrons to reach the

collector [122].

This crowding effect is much reduced when a voltage base is applied as in 3T HPT mode and reducing the RC time constant of the emitter-base junction [122]. However in this case, contrary on what happens for HBT, the gain produced by the transistor effect (on the generated carrier induced by the light injected) is not enough to compensate the high NSD produced by the same phenomenon, leading to high value of noise figure.

Finally in PD mode, the devices has low NSD but also very low gain, provided by the low value of responsivity. However, note that beside the high differences in terms of NSD and G_{OM}^{HPT} , PD and HPT modes results to have similar noise figure.

Figure 3.26 shows the behavior of the NSD measured for the operating frequency considered (750 MHz) in all the three operating modes as function of the optical power.

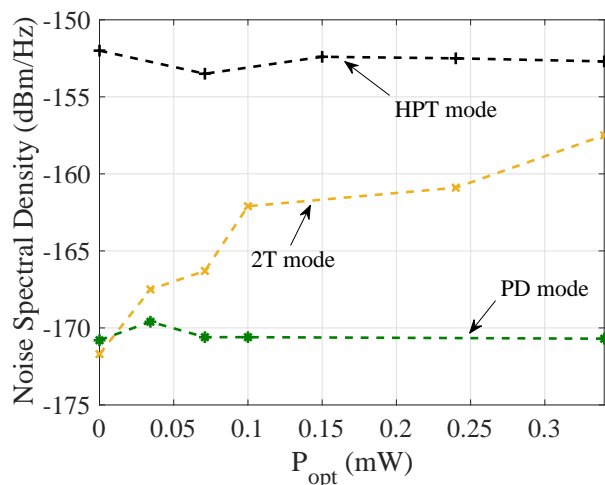


Figure 3.26: Noise Spectral Density of all three operating conditions as function of the optical power received for $f_{RF} = 750$ MHz fixing $V_c = 2$ V.

The first consideration is that the noise produced in presence of HPT mode results to be constant with respect to optical power. Indeed, this means that this is purely electrical noise produced by the HPT and the photocurrent generated does not contribute to the noise. The reason lies in the fact that in such condition the phototransistor has a high level of β (see Figure 3.15) which produces a high electrical gain, but also high electrical noise. This noise has then to be considered as the one produced by the relative HBT technology on which the HPT employed is based. In HBT indeed, this noise is still present but the gain is so high that a very low noise figure of few dB is generally measured. Instead, in case of HPT, this high noise is not compensated by the gain which in this case is also negative (see Figure 3.23) and therefore this fact produces a higher value of noise figure compared to typical values of HBT [121].

A very small variation, with respect to optical power, appears also for PD mode at very low value around -170 dBm/Hz. In this case, since the device operates now as photodiode,

only thermal noise and shot noise are present. However, since the responsivity of the photo-detector and gain (see Figure 3.15 and Figure 3.23) are quite low in such condition, the noise produced by the optical power is still very low, and thus the noise is mostly of thermal nature. In particular, the shot noise is about -184 dBm/Hz for $P_{opt} = 0.34$ mW and $f_{RF} = 750$ MHz (see (3.7)).

Finally for 2T mode there is an evident increase of NSD with respect to the optical power. This phenomenon is related to the very high DC responsivity of the photo-detector (see Figure 3.19) compared to the opto-microwave gain at the considered frequency (see Figure 3.23). This contributes to let the shot noise term be dominant on the laser noise one, which, differently from the shot noise, depends on the frequency behavior of both laser and HPT (see (3.7)). This fact is also confirmed by the linear increment of NSD with the optical power (logarithmic in figure 3.26). In the case of frequency considered ($f_{RF} \in [10 - 2500]$ MHz) and the optical power range ($P_{opt} \in [0 - 0.35]$ mW) the noise is always lower than HPT mode. However this fact can change for different frequencies in which the noise can be higher (see figure 3.24).

Figure 3.27 shows the observed noise spectral density considering V_b as a parameter and fixing the optical power at 0.34 mW and $V_c = 2$ V. This condition indeed includes only HPT and PD mode.

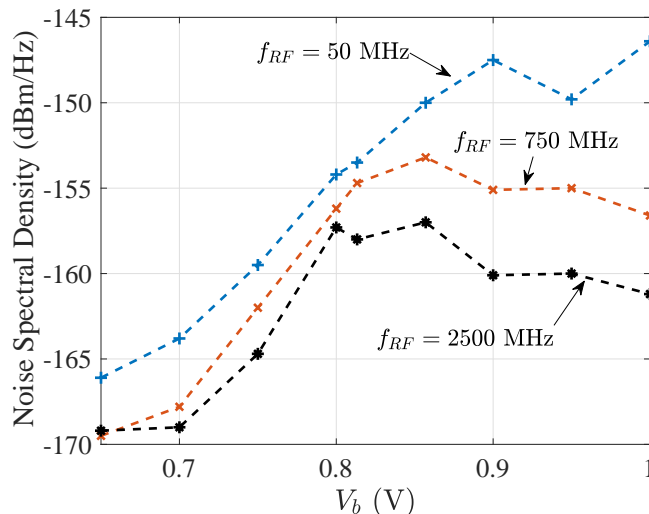


Figure 3.27: Noise spectral density of HPT mode varying V_b fixing $p_{opt} = 0.34$ mW.

It can be noted that for a given value of the frequency (greater than a few hundred MHz) the trend of the noise spectral density for varying values of V_b is very similar to the behavior of the HPT β factor. This is in agreement with the fact that the noise is purely electrical and that it behaves following the trend of the β factor. Moreover, the level of noise density indeed decreases with frequency because of the decreasing of the electrical gain, as happens also for HBT [121].

Evaluation of performance for LTE applications

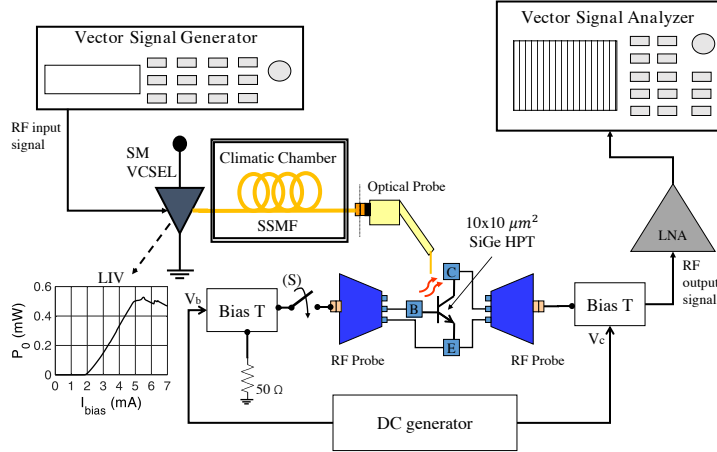


Figure 3.28: Experimental Setup for LTE measurements.

The results obtained in terms of EVM for the three different operating conditions of the HPT are shown in Figure 3.29. The measurements have been obtained with the setup shown in Figure 3.28. In particular, the effect produced by the HPT in terms of gain can be estimated through a de-embedding process which removes the frequency characteristic of the laser exploiting a previous measurement performed with a reference PIN photo-diode. The results are compared with the ones obtained by using the reference photo-diode.

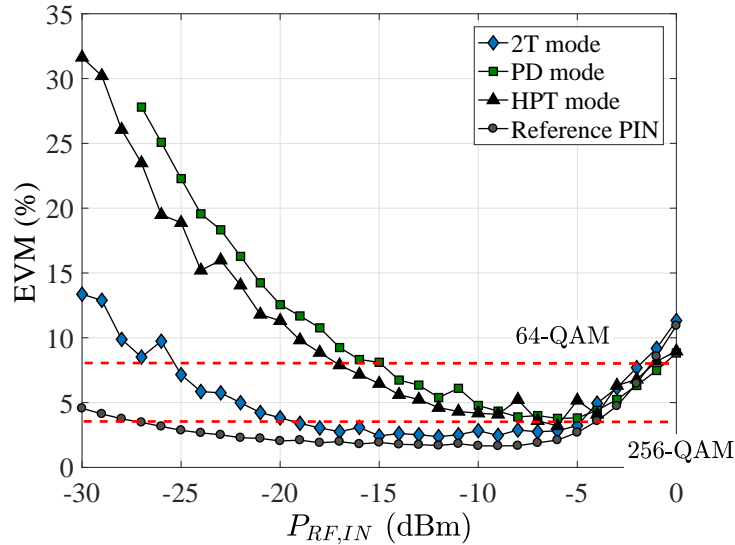
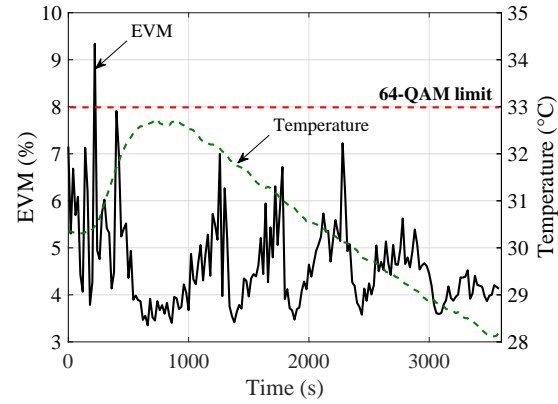


Figure 3.29: EVM result for different operating modes of the SiGe HPT and for the reference PIN photodiode for $f_{RF} = 750$ MHz, $V_c = 2$ V and $P_{opt} = 0.34$ mW.

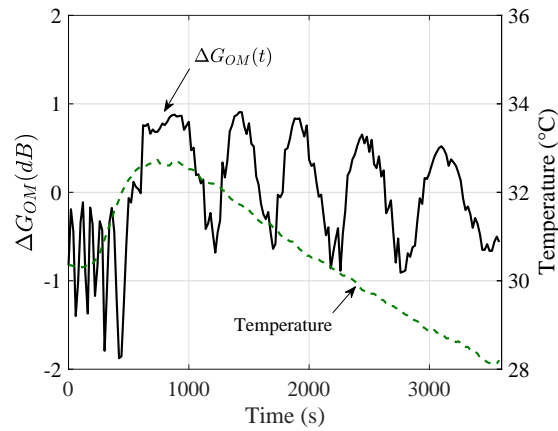
It can be observed that when the HPT works in 2T mode the curve of EVM reaches almost the same level of the curve measured using the reference PIN photo-diode, resulting in the best operating mode of HPT for this type of application. In fact the value of EVM is lower than 8% which fulfills the requirements of the LTE standard for 64-QAM modulation. Moreover, although PD mode presents a lower gain at 750 MHz than HPT mode, and in general up to 2.5 GHz (see Figure 3.23) the EVM curves have almost the same behavior. This is due to the fact that in HPT mode a higher electrical noise is present compared to the one produced in the PD mode, which compensates the lack of gain. This fact is explained by the same noise figure behavior of HPT and PD mode (see Figure 3.25).

Moreover, the presence of two modes within the SSMF together with the small receiving area of the HPT can produce modal noise even for short lengths, resulting in fluctuations of the received power. Mathematically, this means having high values of b_{12} . This type of phenomenon has been already characterized with an accurate theoretical model in Chapter 2, where it was shown the dependence of the fluctuations of RF gain and received optical power on the dimensions of the receiver collecting area. In particular, in presence of a coherent optical source, if the fiber is subjected to mechanical stress or temperature variations, the propagation constant of the modes changes, producing spatial fluctuations which vary the modes configuration on the photodiode surface. These variations lead to power and gain fluctuations related to the strength of the stress produced. In the present case the environment temperature T has been changed with a maximum slope $\frac{dT}{dt} \simeq 0.3^\circ\text{C}/\text{min}$. An example of this phenomenon is shown for 2T mode in Figures 3.30 for 50 meters of SSMF for input RF power of $P_{RF,IN} = -7$ dBm. Note that the behavior of EVM is most of the time below the 64-QAM requirements by the LTE standard ($\text{EVM} < 8\%$) [119]. The same variations are present also for PD and HPT mode since the area of the collecting surface is the same. To decrease further the fluctuations and standard deviations of EVM and RF Gain the technique proposed and validated in previous sections can be exploited.

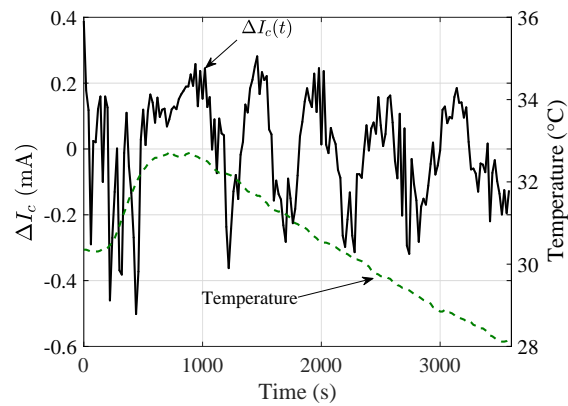
Note that the presence of modal noise is confirmed by gain and collector current fluctuations around the mean value, named ΔG_{OM}^{HPT} and ΔI_c respectively, as presented in Figures 3.30b and 3.30c. These last two quantities vary accordingly to each other, while EVM presents an opposite behavior. This is indeed related to the dependence of SNR on G_{OM}^{HPT} .



(a)



(b)



(c)

Figure 3.30: The influence of environment temperature variations on (a) EVM, (b) Opto-Microwave gain variation ΔG_{OM}^{HPT} and (c) collector current variation ΔI_c .

3.4 Summary and Discussion

This Chapter presented the performance evaluation of the low cost and consumption system based on VCSEL and SSMF. The pre-filtering technique described in Chapter 2 has been usefully adopted to improve the performances in terms of EVM being able of reaching values that allow a LTE 256-QAM transmission of 20 MHz bandwidth. Moreover, the EVM measurements have confirmed that thanks to the pre-filtering technique the RF signals transmission can be performed also in such regions considered critical for transmission. These regions correspond to the case in which values of frequency and length adopted are such that the effect of intermodal dispersion and modal noise are dominant, leading to low average gain and high time fluctuations. The carrier frequencies adopted were in the interval [500-1000] MHz, which represents a possible frequency bands for LTE and future 5G systems. The adoption of the pre-filtering technique allows the VCSEL-SSMF-based link to reach the same performances of the case VCSEL-MMF case with lower cost, especially for such environments in which the SSMF is already installed.

In the second part of the Chapter, the use of SiGe HPT as photo-receiver is investigated. First, a static and dynamic analysis has been performed using for the first time the $9\mu\text{m}$ -core fiber (SSMF). This allowed to measure substrate effects, and intrinsic behavior for PD mode, HPT mode and 2T mode. Moreover, an analysis of the opto-microwave quantities have been performed focusing on gain and noise figure. It has been put in evidence that the 2T mode results to be the best configuration in terms of opto-microwave noise figure, while HPT mode and PD mode result to have the same behavior beside the high gain level difference. This evaluation is also confirmed by the EVM evaluation for the same LTE system tested using a PIN photodiode, in which the HPT in 2T mode reach the same performances as PIN photodiode. It was noted also that the small area of the detector is responsible for important fluctuations of gain and consequently EVM which are due to modal noise, even for short-range SSMF. However, this problem can be theoretically solved using the pre-filtering technique adopted in the first part of the Chapter. The experimental validation of this assumption is considered as future test.

Experimental study of polymer structure for collective and passive optical coupling

This Chapter shows the study and analysis performed on a polymer-based collective passive optical coupling structure realized by ICON Photonics[®] in order to improve the optical coupling between fiber and photodetector (fiber-to-PD) and vertical emitting lasers and fiber (VCSEL-to-fiber).

Section 4.1 presents a description of the structure realized.

Section 4.2 describes the results obtained for fiber-to-PD coupling in case of SSMF coupled with $10\mu\text{m}$ photodetector operating at 1550 nm while Section 4.3 describes the results obtained for the same fiber and photodetector at 850 nm.

Section 4.4 finally describes the results obtained in case of VCSEL-to-fiber coupling, in particular focusing on MTM VCSEL and MMF.

Finally in Section 4.5 discussion and summary of the Chapter are given.

4.1 State of the art and description of the passive coupling structure

Nowadays, one of the key challenges for optical connections and interconnections technology is the optical coupling of top-illuminated/emitting devices such as top-illuminated photodiodes, VCSEL or edge-emitting lasers with Vertical Grating Coupler (VGC) [123–126]. In particular the main challenges of the vertical optical interconnects are the optical coupling efficiency, the alignment tolerance and the fabrication compatibility to the different system elements such as pads, RF lines, fiber contact, etc. The basic coupling solution is a simple butt-coupling which consists on coupling directly the fiber touching the device. This solution is simple but is however dependent on fiber alignment, especially for low diameter devices. An alternative solution is to use micro optical elements such as lenses and ball-lens [127–129] which add however an extra cost and complexity since one more element must be placed and

This chapter is based on the results published in P.5

aligned to the device. When coupling $10 \times 10 \mu\text{m}^2$ active area photodetector with multimode fibre (MMF) at 850nm, a coupling efficiency as low as to 35% is expected as in [25]. VCSEL butt-coupling to a MMF (SSMF) respectively can be found up to 80% (47%) with respect to its lateral tolerances for 1 dB alignment tolerance of $\pm 5 \mu\text{m}$ ($2 \mu\text{m}$) resp. [25]. The use of microlenses or other complex light guiding or confinement system is also considered to improve the coupling efficiency [127, 128], which adds however extra cost and complexity since one more element must be placed and aligned between the device and the fiber. Direct integration techniques have been also developed in order to explore the collective fabrication and integration at the chip/wafer level. An example for such approach is a vertical optical coupler to planar photodiode using an amorphous Silicon waveguide grating coupler with SSMF of 850 nm, which is presented in [130] with the coupling efficiency of 80%. Another example is the monolithic lenses fabricated in the back of the VCSEL/PD substrate [129]. The main drawback of the latter solution is that it is restricted to transparency of substrate and also puts constraints on the substrate thickness which limits the active area and the device bandwidth. Recently, direct integration of polymer materials fabricated on the top of devices got a great interest regarding potential on the cost-performance trade-off point of view [124, 131–133]. Those techniques are based on Ultraviolet (UV) light with a photomask transfer method (at a wafer level scale process) to create polymer pillars on the top of the active devices with precision better than $1 \mu\text{m}$. Although these are promising techniques, the dimensions are still high compared to active areas of the high speed photodetectors when the side is shrinking down to less than $10 \mu\text{m}$.

The optical coupling structure studied is based on of SU-8 polymer and is called ICON technology [134]. This structure is placed between the optical fiber and the optoelectronic component as presented in Figure 4.1. The structure is divided into three parts: The first part is the core of the structure realized in SU-8, that consists of a conical-shape for mode adaptation (see Figure 4.1c), called taper, which couples and guides the light in a controlled way. The second part of the structure is the mechanical support of the fiber. It is made from silicon and consists in an opening (hole) for the placement and fixture of the fiber (see Figure 4.1b). The third part consists in anchoring structures called taper-arms which are made at the top sides of the cone to firmly maintain the taper structure at its vertical position as shown in Figure 4.1a. These arms are made from SU-8 and play an essential role especially when the cone angle is large (i.e. when the photodiode active area is smaller compared with the fiber core dimension).

For both cases, VCSEL-to-fiber and fiber-to-PD, to realize the taper structure the wafer is spin-coated with SU-8 based on the SU-8 2025 series from Microchem Corporation [135]. The spinning of 500 *rpm* with an acceleration of 100 *rpm/s* for 5 seconds, followed by a spinning cycle at 2100 *rpm* with an acceleration of 300 *rpm/s* for 30 seconds is performed. Then the wafer samples are soft baked in a hotplate of 65°C and 95°C for 60 and 300 seconds respectively. Before the UV light exposure, the edge bead created during the spin coating is removed in order to achieve better pattern definition by approaching the photomask to the photoresist. Then the UV light exposure is performed using a Karl Suss MA150 mask aligner where an alignment procedure to the first photolithography is implemented through the masks

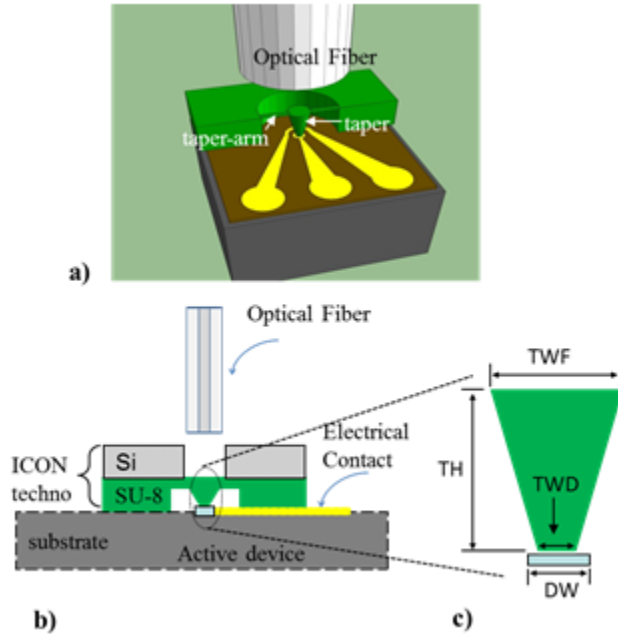


Figure 4.1: a) The 3D illustration of our technology b) Diagram of the coupling system proposed in profile mode; c) the optical taper structure where TH: Taper height, TWF: Taper width in contact with the fiber, TWD: Taper width in contact with the photodiode, WD: the width of the detector.

layout design. The absence of the wavelength filter is applied to help the taper angle feature. The UV energy dose is controlled and it is a key parameter to optimize the taper angle (the cone-shape) [134]. Different energy doses were studied 63-210 mJ/cm² (considering an Aluminum substrate relative dose). The partial isotropy of the photolithographic process under exposure of the resist is privileged that makes possible for the fabrication of suspended arms to maintain the optical structure vertical, without altering the optical propagation within the structure. The post exposure bake is then implemented with a hotplate at 65°C and 95°C for 60 and 300 seconds respectively once again. Finally, the SU-8 layers were developed for 7 minutes then followed by rinsing and final drying at 50 °C.

A Scanning Electron Microscopic (SEM) view of the resulting structure is given in Figure 4.2. Figure 4.2a shows the realization of the taper without anchoring structure and Figure 4.2b shows the fabricated taper structure with anchoring structure with two holding arms. Without any supporting structure, the taper could fall down as shown in Figure 4.2a. Finally, conical-shaped taper structures with upper and lower diameters of 25μm and 10μm, respectively, and with a height of 100μm were fabricated as the one shown in Figure 4.2b.

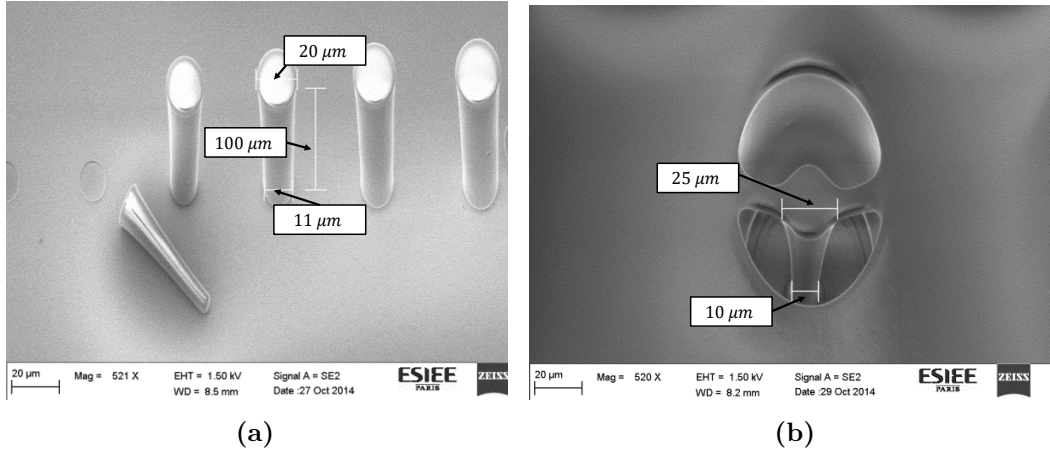


Figure 4.2: a) SEM photograph of the SU-8 cone without suspension arms with different base diameters; b) SEM photograph of the cone with two suspension arms.

4.2 Case at 1550 nm SSMF-to-PD

The top side of the taper (cone) structure is designed to have larger diameter with respect to the core of the optical fiber to easily collect the light beam. However, the lower side is designed to fit with the size of the photodiode. As a result, the SU-8 conical-shape taper guides the light and reduces the mode size from the fiber to the photodetector. This taper structure reduces fiber-to-air /air-to-fiber and air-to-photodiode reflections as it is made directly in contact with the fiber and the photodiode.

For this case the optimization of the structure has been performed exploiting a RSoft[®] commercial simulator. In particular, the simulation has been performed in order to maximize the coupling efficiency between a SSMF with a core diameter of $9 \mu\text{m}$, operating at $1.55 \mu\text{m}$ wavelength, and a $10 \mu\text{m}$ diameter photodiode. One has to consider, although the fiber core diameter is less than the active area of the photodiode, the optical beam emitted from this core at $1.55 \mu\text{m}$ has mode field diameter of $10.6 \mu\text{m}$ [31] which is larger than the optical opening of the photodiode. In the simulation the taper is considered touching the photodiode and far from the fiber of $10 \mu\text{m}$. This distance is set to better fit the experimental measurements. The simulations have indicated that it is possible to obtain a coupling efficiency greater than 90% for resin thickness, TH, greater than $35 \mu\text{m}$ for a top side cone diameters, TWF, greater than $15 \mu\text{m}$. For the same configuration, the Full Width Half Maximum (FWHM) (in μm) is also extracted via RSoft[®] simulation showing that it can be greater than $20 \mu\text{m}$ for TWF greater than $20 \mu\text{m}$ and TH of $40 \mu\text{m}$.

To validate the proposed concept, the conical-shaped taper structure is fabricated on glass wafer with diaphragm approach to be tested with a wide active area optical power meter detector (PIN PD), as illustrated in Figure 4.3b.

The diaphragm structure is fabricated based on the processes shown in Figure 4.3a. A 4 inches glass wafer of $500 \mu\text{m}$ thickness is sputtered with a 300 nm layer of aluminum. Then, photolithography process followed by chemical etching is performed to etch the deposited

metal so as to create an optical opening of the diaphragm (as in Figure 4.3a - G-3).

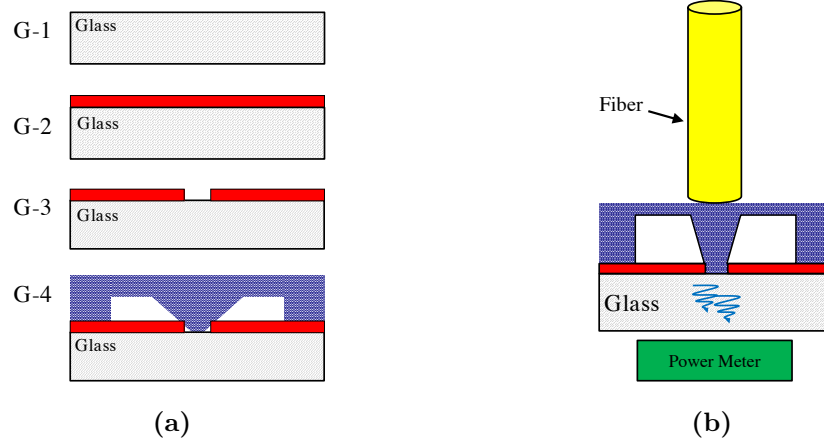


Figure 4.3: a) Technological manufacturing process illustration for the fabrication of the proposed taper structure over a glass wafer: G-1: clean glass wafer, G-2: the glass wafer after metal sputtering, G-3: the glass wafer after metal etching to create an optical opening of the diaphragm, G-4: the taper structure fabricated on the glass wafer. b) The schematic profile view of the proposed diaphragm structure.

The fabricated taper and butt coupling structures are tested with a G.652 single mode optical fiber excited by a 1550 nm laser by the test bench shown in Figure 4.4 considering the switch (S) in case (A) in which the climatic chamber represented is switched off.

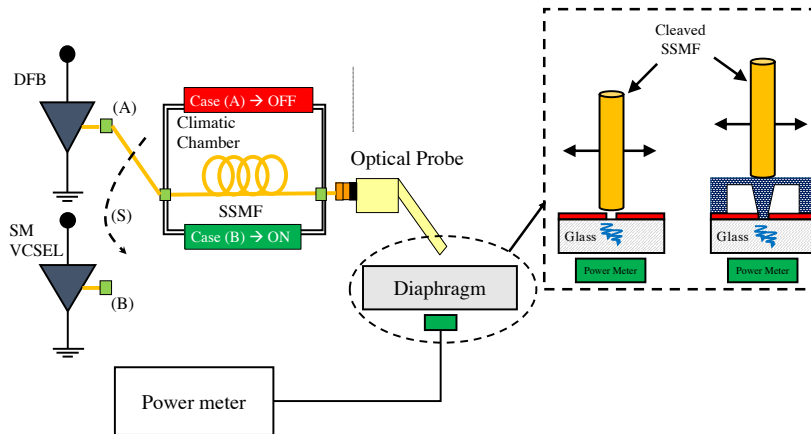


Figure 4.4: Experimental setup for testing in case of simple butt-coupling and using the polymer-based structure.

The schematic figure of the butt-coupling (reference) and taper structure along with the optical fiber are shown as inset. The end tip of the fiber is cleaved and placed vertically to the structure. Its position is controlled by a nano-positioner to scan over the surface of the cone with an accuracy of 20 nm. A 10 μm air gap between the fiber and the taper is considered to scan the fiber over the top of the device under test. The optical power meter head is placed

beneath the structure under test as shown in the schematic picture in Figure 4.4. A SNOM is then performed by moving the fiber on the top of the taper. The same mapping is performed for the reference structure that is not covered by the polymer (without taper structure). The coupling efficiency is then experimentally extracted in both cases and thus compared as shown in Figure 4.5. The fitting between the experimental and simulation results are also presented in the same figure.

A coupling efficiency of 86% and 94% is measured for butt coupling and the taper structure respectively. This peak value is obtained when the fiber is exactly aligned with the taper structure (i.e. X position equal to $0 \mu\text{m}$). An improvement of 8% is measured compared to the butt coupling structure. This improvement is due to the fact that the upper cone diameter of the taper is wide enough to collect all the light coming from the standard single mode fiber while the conical polymer taper structure is good enough to confine the light into the smaller diameter of the cone. This coupling ratio could increase if the fiber comes into contact with the structure.

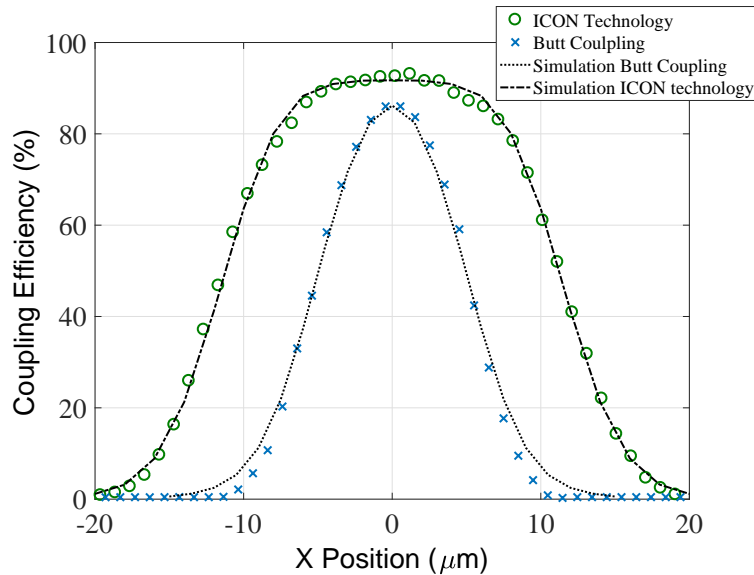


Figure 4.5: Experimental and simulated results of coupling efficiency versus optical fiber position for butt coupling and conical optical taper structure with an expected photodetector diameter of $10 \mu\text{m}$. The air gap between the fiber and the optical taper or reference structure is about $10 \mu\text{m}$. The simulation structure size: $\text{TH}=100 \mu\text{m}$; $\text{TWF}=25 \mu\text{m}$ and $\text{TWD}=10 \mu\text{m}$

A very good agreement between measurement and simulation is shown in Figure 4.5 for both butt and taper coupling structures. For this simulation, a Gaussian beam with mode field diameter of $10.6 \mu\text{m}$ is considered according to the standard single mode G.652 fiber. We also considered the reflection effect at the injection of light (i.e. the glass for butt coupling structure and the SU-8 for the taper structure). The 1 dB alignment tolerance of $\pm 9 \mu\text{m}$ is measured for the polymer-based structure while 1 dB alignment tolerance of the butt coupling is $\pm 3.5 \mu\text{m}$ which is less than a factor of 2.57 compared to the taper structure case.

4.3 Case at 850 nm SSMF-to-PD

The interesting results obtained for SSMF-to-PD case at 1550 nm can be extended to the same case operating at 850 nm using as source a SM VCSEL. As explained in detail in Chapter 2 the major problem of such type of link is related to the bi-modal propagation at 850 nm of SSMF which contributes to generate output power fluctuations on the receiver side, especially for low size photo-detector. The model developed in Chapter 2 shows the importance of having perfect alignment between connectors (if more than one long fiber is used) and between the final fiber pigtail and photo-detector. Especially for low size photo-detector this can be a serious problem, and optical power fluctuations, relative to the mean optical power, can be strong. In particular, the effects of modal noise in such case have been shown in detail in Section 2.3 of Chapter 3 when the $10 \times 10 \mu m^2$ SiGe HPT has been used as photo-detector for LTE transmissions. For this last case the fluctuation of the RF gain, for which the standard deviation σ_G can reach several dB, can lead to fluctuations of SNR and successively to fluctuations of EVM.

As described by the model shown in Sections 2.2 and 2.3 of Chapter 2, σ_G is directly proportional to the relative variation of the received RF modulating power, as happen also for the optical power. Indeed, reducing the fluctuation of the optical power the effect on the RF fluctuations reduces as well. The mean value and fluctuation of the optical power ΔP_{opt} in case of the two modes propagation in SSMF at 850 nm is expressed as follows:

$$\mu_{opt} = P_0 [A_1^2 b_{11} + A_2^2 b_{22}] \quad (4.1)$$

$$\Delta P_{opt}(t) = P_0 [2A_1 A_2 b_{12} \cos(\Delta\beta(t))] \quad (4.2)$$

where P_0 is the total initial optical power, A_i is weight of the i -th mode such that $\sum_i A_i^2 = 1$ and $\Delta\beta_{12}(t)$ is the difference in time of the phase of the two modes which is supposed varying in time. The expression of the standard deviation σ_{opt} can be then computed as:

$$\begin{aligned} \sigma_{opt} &= \sqrt{\text{var}(\Delta P_{opt})} = \sqrt{\langle \Delta P_{opt}^2 \rangle} = \\ &= 2P_0 A_1 A_2 b_{12} \end{aligned} \quad (4.3)$$

so that the expression of the relative optical power variation Γ_{opt} can be expressed as:

$$\Gamma_{opt} = \frac{\sigma_{opt}}{\mu_{opt}} = \frac{2A_1 A_2 b_{12}}{A_1^2 b_{11} + A_2^2 b_{22}} \quad (4.4)$$

which can be expressed as percentage of the average power value μ_{opt} . As explained in Chapter 2, b_{ii} represents the power loss of the i -th mode due to the finite area S_{PD} and its value contributes to the mean value μ_{opt} . The term b_{12} instead, represents the non-orthogonality of the modes generated by the finite area S_{PD} . Indeed, if $S_{PD} \rightarrow \infty$ then $b_{21} = 0$ because of the orthogonality property of modes in electromagnetic waveguide and because no

fluctuation is present (see Eq. (4.2)). However if S_{PD} assumes finite values, especially of the same order of the area occupied by the optical field within the optical fiber, then a minimum misalignment between the fiber and the center of symmetry of the photodiode surface will give $b_{21} > 0$ and consequently $\Delta P_{opt}(t) \neq 0$. A possible theoretical behavior for different sizes of photodiode is shown in Figure 4.6.

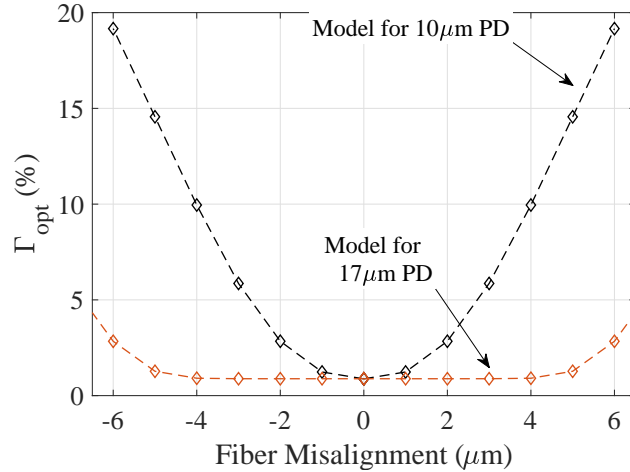


Figure 4.6: Example of theoretical behavior of Γ_{opt} for different PD diameter sizes.

To measure the optical power P_{opt} and its fluctuations due to modal noise the setup shown in Figure 4.4 has been utilized taking the switch (S) in position (B). For this case, the 850 nm SM VCSEL already coupled to a pigtail of 9 micron single mode fiber provided by Optowell[®] has been employed. Then, 30 meters of SSMF have been inserted in a climatic chamber to force controlled temperature variations of maximum slope of $\pm 1^\circ C/min$. The optical power is measured for a time period of one hour with a sampling period of one second. An example of measurement of $\Delta P_{opt}(t) = P_{opt}(t) - \mu_{opt}$, where $\mu_{opt} = \langle P_{opt}(t) \rangle$, is shown in Figure 4.7.

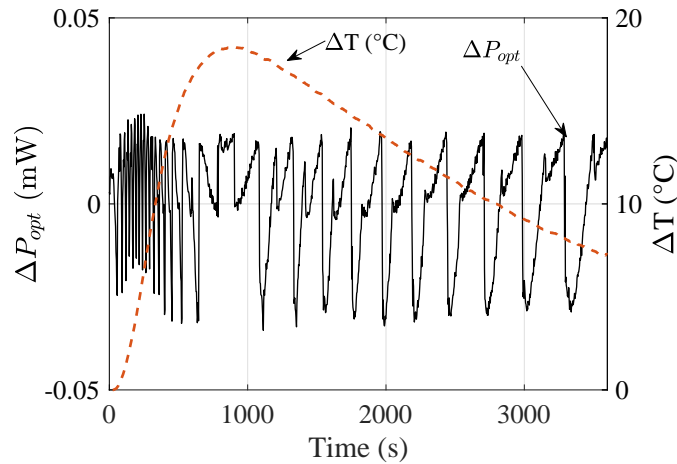


Figure 4.7: Example of Time measurements of ΔP_{opt} for 10 μm diameter photo-detector.

To evaluate the impact of fluctuations on optical power received, the parameter Γ_{opt} defined in Eq. (4.4) is considered. Figure 4.7 shows also the typical temperature behavior of each measurement performed. Both rise and fall slopes are tested in order to improve the statistical validation.

As first test, the 10 μm PD and the polymer-based structure have been tested at constant temperature and for different fiber positions. The result is presented in Figure 4.8.

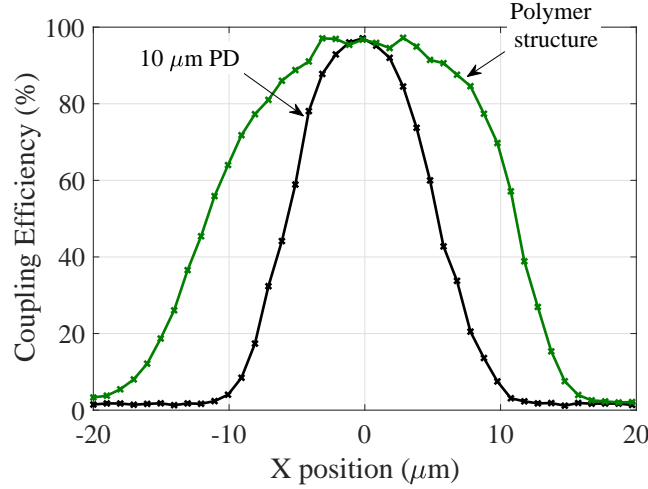


Figure 4.8: Coupling efficiency of 10 micron photodiode with and without the polymer coupling structure.

Therefore as first result, the polymer-based structure results to be stronger to misalignment than the simple butt-coupling of 10 micron PD confirming also in this case the results obtained in 1550 nm case.

Taking as reference the results obtained in Figure 4.8, the nanopositioner is used to locate the optical fiber and change the alignment with the structure tested. A maximum misalignment of $\pm 10\mu\text{m}$ has been considered for both situations. Figure 4.9 shows the behavior of Γ_{opt} measured in both conditions.

The theoretical model described above is used to fit the measurements. The parameters consider for the model are obtained considering the LP_{01} and LP_{11} modes of a SSMF and considering the respective amplitude coefficients having almost the same weight ($A_1 \simeq A_2$). Moreover a relative Γ_{opt} floor is considered which takes into account possible fluctuations due to connectors misalignment. For the case of the polymer structure, an equivalent diameter of 17 μm is considered. The results show a big tolerance of the polymer-based structure on fiber misalignment, together with an higher average optical coupling efficiency, confirming the measurements performed with $\Delta T \simeq 0^\circ\text{C}/\text{min}$ of Figure 4.8.

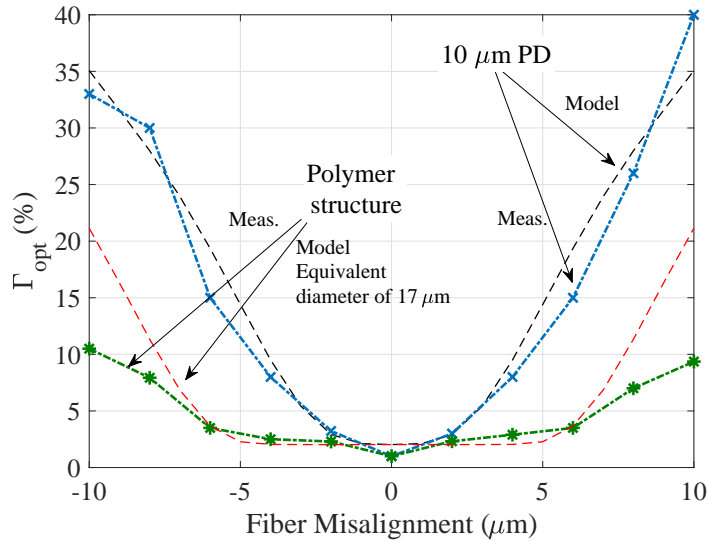


Figure 4.9: Relative optical power variation Γ for 10 μm diameter PD with and without the polymer-based coupling structure.

4.4 VCSEL-to-fiber case

This Section provides experimental and simulation results in case the same technology presented in the previous cases (ICON technology) is used for coupling a 850 nm VCSEL with MMF. In this case, the SU-8 polymer cone structure is formed directly on top of the VCSEL and has a conic shape that guides the light coming from the laser toward the optical fiber. The dimensions are designed in order to have the output size diameter of the taper lower than the diameter of the MMF (50 μm). The fiber is then put in contact with the taper which, thanks to its low diameter size, accommodates a possible misalignment of the fiber. As for the fiber-to-PD case, to maintain vertical and stable the structure suspended arms are also designed and fabricated.

The dimensions of the structure are optimized in order to maximize the fiber coupling taking into account the properties of the standard GI-MMF and the VCSEL emission field. A 4 inches Silicon substrate is used in which few cavities are etched through a Deep-Reactive-Ion-Etching (DRIE) process in order to avoid a real 4-inch full VCSEL wafer. As laser sources, 14 Gbps 7 μm diameter aperture VCSEL chips, from Philips-Ulm Photonics in 4x1 arrays are used and inserted in the cavities (see Figure 4.10a). The taper is designed to have TWF = 22 μm , TH = 60 μm and TWD = 10 μm with a tolerance of $\pm 2\mu\text{m}$.

Experimental Characterization

Similarly to the fiber-to-PD case, a characterization has been performed testing the structure with a cleaved GI-MMF of 50 μm diameter (see Fig 4.10a) and measuring the light with a power meter. The emitted light is measured in butt-coupling configuration and with ICON technology in order to compare the two situations (see Figure 4.10). The distance between the

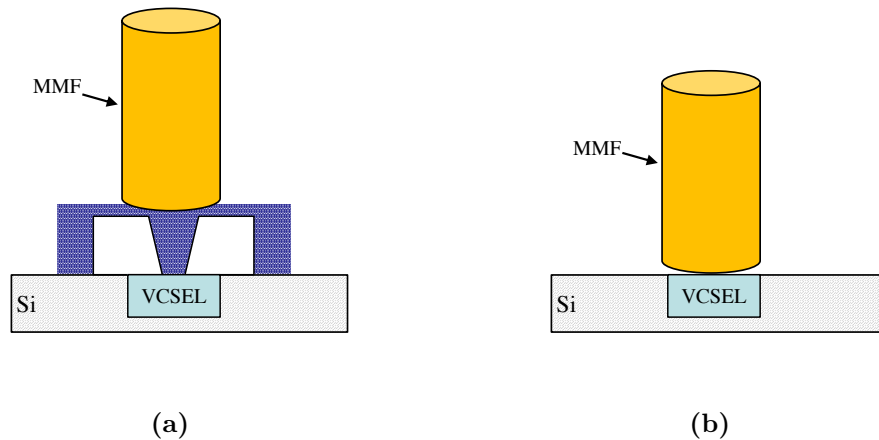


Figure 4.10: Schematic of the experimental characterization for VCSEL-to-Fiber case in which the effect of coupling structure (a) is compared with butt-coupling (b).

fiber and VCSEL (in case of butt-coupling) and the one between fiber and structure (in case of ICON technology), is computed to be around $10\mu\text{m}$. Moreover, the optical probe presents a fixed angle around 6° between the fiber and the right angle to the die, in order to avoid parasitic optical cavities.

Figure 4.11a shows the L-I curve reached with ICON Technology and with the simple butt-coupling. It is possible to observe that at high values of biasing currents, ICON technology keeps the linearity while butt-coupling tends to saturate. This can be explained with the better confinement of higher order VCSEL modes reached by ICON technology, which for high biasing current are stronger. In fact, as shown in Chapter 1, for high values of biasing current the emitted power of a VCSEL is distributed along different transverse modes, increasing the divergence of the device. For this reason it is reasonable to assume that the improvement reached at high levels of current is due to better confinement of ICON technology compared to simple butt-coupling. The relative power increment among the optical power in case of ICON Technology (P_{ICON}) and the optical power in case of butt-coupling (P_{butt}), defined as $\frac{P_{ICON}-P_{butt}}{P_{butt}}$, is shown in Figure 4.11b where a proportional improvement with the bias current can be observed.

Moreover, a SNOM measurement has been performed in order to test the behavior of the structure in case the alignment with the fiber is not perfect. Figure 4.12 shows the effect of the fiber misalignment on the optical power emitted for a bias current of 4.5 mA. The optical taper is shown to improve the tolerance to the optical fiber misalignment in terms of FWHM versus the fiber positioning, passing from $\pm 15\mu\text{m}$ to $\pm 20\mu\text{m}$.

In order to verify the effect of such structure on the RF behavior of the device, a measurement of modulation response is performed through the usage of a VNA. Figure 4.13 shows the behavior of modulation response of the VCSEL in the two cases. In particular, $G_{OM}^{LD} = 20 \log_{10}(\eta_{LD})$ is measured exploiting a photodetector with a frequency flat response up to 25 GHz having $G_{OM}^{PD} = 20 \log_{10}(\mathcal{R}) = -19\text{ dB}$ at 850 nm. The fiber length is less than 1 meter and its effect is considered negligible.

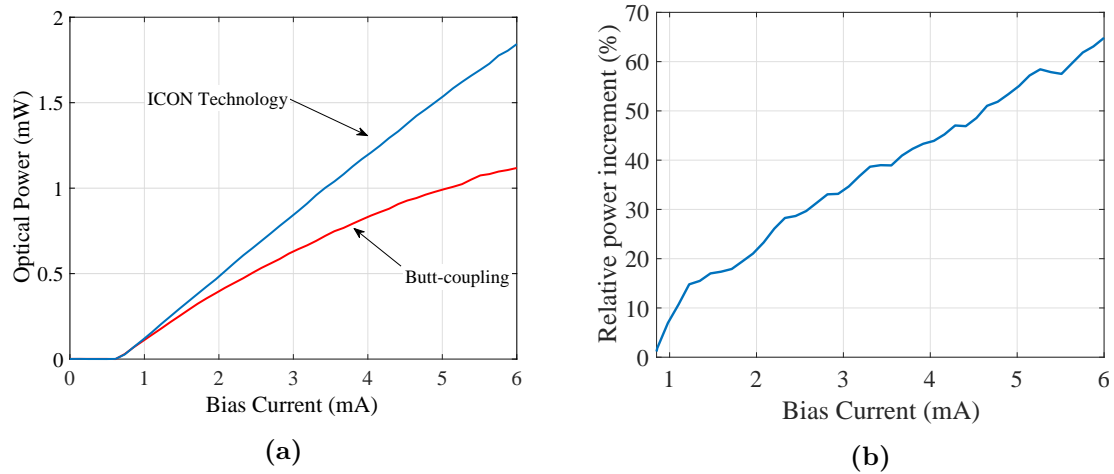


Figure 4.11: (a) L-I curve of the VCSEL under test using ICON Technology and using the butt-coupling technique. (b) Relative power increment produced by ICON technology.

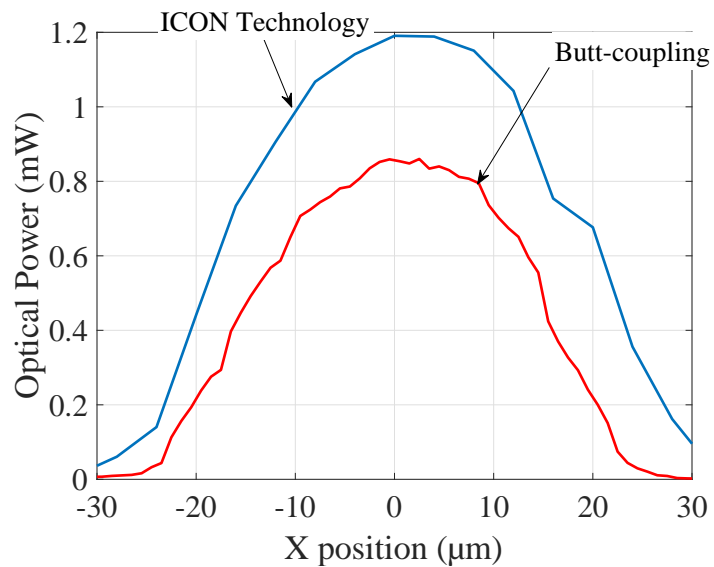


Figure 4.12: Optical power emitted as function of the relative fiber position with respect to the VCSEL with ICON technology and with simple butt-coupling. VCSEL is biased at 4.5 mA.

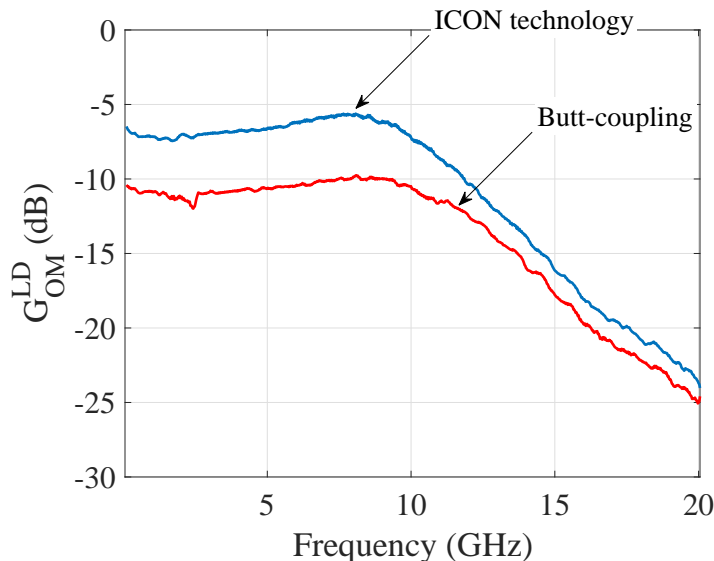


Figure 4.13: RF Gain measured with a VNA for the optical link composed by VCSEL, optical 1 meter of MMF probe and 25 GHz New Focus photodetector for both ICON technology and butt-coupling. The VCSEL is biased at 6 mA.

Firstly, an improvement of about 4.5 dB is evaluated which is in agreement with the relative power increment shown in Figure 4.11b. In fact for 6 mA of biasing current the relative power increment is about 65% which means $P_{opt,ICON} = 1.65P_{opt,Butt}$. This improvement in the efficiency produces an increment in the RF gain of about 4.5 dB. As second observation a slight change in the 3dB cut-off frequency of the laser is present. This quantity pass from 12.6 GHz of Butt-coupling case to 11.6 GHz produced by ICON technology. This fact can be related with a slight change in the cavity properties of the laser. This assumptions need anyway to be validated with further experiments

4.5 Summary and Discussion

In this Chapter a low cost passive and collective optical coupling structure based on SU-8 polymer realized by ICON photonics[®] has been described and characterized. Firstly, the coupling between optical fiber and photodetectors has been presented, showing the improvement that such structure brings in terms of optical coupling and tolerance in case the optical fiber works at 1550 nm and the photodetector has $10 \times 10 \mu m^2$ area. The improvement is of 8% on the coupling and from $\pm 3.5 \mu m$ to $\pm 9 \mu m$ on the 1dB tolerance. Moreover, the same structure is presented for the case of study presented in Chapter 2 and 3, in which the SSMF is excited at 850 nm through a SM VCSEL. In this case the structure gives a slight improvement in terms of coupling efficiency while for the 1dB tolerance the improvement results to be the same as for the case 1550 nm. Moreover, in case of 850 nm propagation the structure helps to reduce the relative fluctuations of the optical power due to modal noise. According to the model proposed, the 10 μm diameter PD is seen by the fiber with an equivalent diameter of

about $17\ \mu\text{m}$ thanks to the taper.

The Second part of the Chapter described the same technology to be used in order to improve the coupling efficiency between vertical emission lasers (VCSEL) and optical fiber. Using the same technology process, the structure helps to increase the optical power coupled to the fiber, bringing to a proportional increment with MMF. A bigger tolerance of $\pm 20\ \mu\text{m}$ and a slight change in the 3dB frequency response are observed giving overall much better performances with respect to butt-coupling. The light coupling improvement is hence explained by better VCSEL emitting modes confinement toward the MMF and by a material matching provided by SU-8.

Conclusions and Perspectives

Conclusions

The objective of this work was to show a possible RoF system in order to minimize cost and consumption within current and future applications which are now based on RoF, or for which RoF is the main solution in order to achieve the desired performances. In particular, the high network spreading (VDN) adopted by current and next cellular system standards (LTE, 5G) in order to increase the capacity of the network requires many connections within the access networks. Therefore, the high density of the network requires higher number of links between the access points and the centralized stations.

In Chapter 1 an introduction on RoF system has been presented, explaining in details what is RoF technology and what is its purpose. Different techniques are discussed, focusing on the advantages that they bring compared to the simple IM-DD solution. Cost and complexity are finally discussed, concluding that to realize low cost RoF systems the IM-DD solution is the best choice.

In order to contextualize the work, different applications of RoF are discussed. The low cost system which is proposed in this dissertation is intended to target all the applications in which RoF systems are currently present being possible candidates for future developments. In particular, these regards the current and next generation of telecommunication networks, Local Area Networks (LANs), Wireless Local Area Networks (WLANs), Home Area Networks (HANs) and Mobile Front-Haul (MFH) of Very Dense Networks (VDNs) deployed in fourth generation and to be deployed in future fifth generation of cellular systems. Moreover, the application target includes Radio Astronomic scenarios, which typically uses RoF for transmitting the signal from the antenna to processing-room.

The low cost RoF link studied in then composed of 850 nm Vertical Cavity Surface Emitting Laser (VCSEL), Standard Single-Mode Fiber (SSMF) and SiGe Hetero-junction bipolar Photo-Transistor (HPT). These three elements have in common to be low cost and, in case of transmitter and receiver, to be low consumption, leading to a suitable combination for the objective of this dissertation. A detailed description of those components was then presented showing what are the advantages of using such components, compared with other possible solutions.

Chapter 2 presented the propagation model at 850 nm of the SSMF and the relative results. The model description was necessary to understand deeply the major problems given by the two-modes propagation within SSMF at 850 nm: intermodal dispersion and modal noise. The two effects were described physically and the model was confirmed by experimental results. The main problems given by such effects are bandwidth limitations and time fluctuations of the optical power (and consequent gain on the useful signal) in presence of temperature variations. These fluctuations can bring important detrimental effects on the Signal-to-Noise Ratio of the system. It was recognized that this two phenomena are strictly related and their importance depends on the radio frequency carrier considered and the length of SSMF. Depending on those quantities it is possible to identify critical regions in which the signal propagation presents high distortion and low signal-to-noise ratio which does not allow a clear signal transmission.

Starting from the model, a technique to mitigate such problems was proposed. This technique consists on avoid the excitation of the higher order mode exciting the SSMF with a short span of 5 μm diameter fiber designed to be single mode at 850 nm. Because of this excitation the SSMF presents a quasi-single-mode propagation which mitigates intermodal dispersion and modal noise. This technique has been validated both theoretically and experimentally with an important improvement in the critical regions.

The model developed brought important information on the parameters that influence the propagation. In particular, it allowed to exploit the two-modes propagation to reversely compute the laser frequency chirp of the VCSEL source. In this case, the effect of modal noise has been enhanced in order to better measure the fluctuations of power and gain. Through the relative phase of such fluctuations it is possible to estimate the frequency chirp. The same approach was also extended to 1310 nm and 1550 nm DFB lasers through an interferometry-based technique realized ad-hoc which results to be a particular case of the model developed for the chirp evaluation of 850 nm VCSEL.

In Chapter 3 the system studied was tested in a real application of 256-QAM LTE data transmission of 20 MHz bandwidth. Firstly the system employed a SM VCSEL operating at 850 nm, a SSMF and a PIN photodiode. The system was then evaluated in terms of Error Vector Magnitude (EVM) for different fiber lengths and frequency carriers in order to evaluate the performances inside and outside the critical regions identified in Chapter 2. In compliance with the LTE standard, a possible 256-QAM transmission has been reached outside the critical regions, while for critical regions the solution proposed in Chapter 2 is tested. Important improvements was reached in terms of Error Vector Magnitude for which the pre-filtering technique made the system reached the 256-QAM transmission also within the critical regions. Because of modal noise fluctuations, a statistic of EVM was evaluated in order to identify the average value reached, its standard deviation and the compliance probability of having clear 256-QAM LTE transmission. A huge improvement in critical regions was reached for this last quantity, moving from 0% to 90%, improving drastically the transmission.

After having validate the proposed system and technique, the Chapter presented the per-

formance evaluation for the systems proposed replacing the PIN photo-detector with a SiGe HPT presented in Chapter 1. Firstly a DC and RF characterization of the device illuminated with a $9\ \mu\text{m}$ diameter fiber has been presented, analyzing all the possible operating modes of the device. Then, the performance of the overall link composed of 850 nm VCSEL, SSMF and SiGe HPT receiver was evaluated and compared with PIN photodiode receiver performances. Since the objective was to compare the system performances with two different detectors the system has operated outside the critical regions. These regions are in fact related only to the propagation within the fiber and are independent on the receiver. It was found that the best configuration for SiGe HPT was the two-terminal mode, which means keeping floating the base contact. For this configuration, the 256-Quadrature Amplitude Modulation (QAM) transmission is achievable without any temperature stress on the fiber. However, due to the small area of the photo-detector, important fluctuations of EVM are present when the temperature varies, leading to an EVM such that only the 64-QAM transmission is achievable. However, this value could be theoretically improved with the technique proposed in Chapter 2. This will be tested in future validation.

Finally Chapter 4 aimed to analyze the possibility of further improving the system with a low cost optical coupling structures. In particular, this Chapter showed some experimental results obtained with a particular coupling structure realized for both VCSEL-to-fiber and fiber-to-PD optical coupling. This structure is based on a wafer-level fabrication process which is able to create a collective and passive optical coupling structure improving efficiency and tolerance while keeping the cost low. Three coupling structure cases have been presented. In the first case the structure was realized for high speed applications that requires 1550 nm DFB transmission with SSMF coupled with a small area photo-detector (in this case $10\ \mu\text{m}$ diameter). The use of this structure was compared with the simple butt-coupling, showing an improvement of 8% in terms of coupling efficiency. Moreover, the 1 dB alignment tolerance reached by ICON technology is $\pm 9\ \mu\text{m}$, while for butt-coupling is measured to be $\pm 3.5\ \mu\text{m}$. After having validated this case, the structure was tested for the RoF link studied in this dissertation, composed of SM VCSEL and SSMF. It was shown that also in this case an improvement in terms of efficiency and tolerance can be reached, even if those values are lower than the previous case. However, a big improvement is achieved regarding the fluctuations of optical power due modal noise produced by the small area photo-detector. The mathematical model developed is also confirmed by the experimental behavior.

Finally, the same coupling structure technology was used for coupling VCSEL (MTM) to the fiber (MMF in this case). Also in this case, important improvement was reached, in particular a constant improvement for different biasing current of the laser is present. It was note that higher the biasing current higher the improvement, reaching 65% of relative improvement between ICON technology and butt-coupling for 6 mA of biasing current.

Future perspectives of the work

The future perspectives of the presented work can be summarized as follows:

- Only a single LTE 20 MHz channel transmission has been modeled and experimentally tested. Indeed, multi-channel transmission represents a more realistic case which takes into account a possible interference between the channels and consequent detrimental of the performances. A possible future work might consist on testing and modeling the multi-channel propagation and quantifying the effect of the channel interference produced mainly by the non linearity of the RoF system.
- The application target of the system includes also the new generation of cellular system standard, the 5G. This technology , which has been officially standardized for the first time in July 2018 [118], allows the transmission of high bandwidth signals (around 100 MHz). A possible future work can be the validation of the pre-filtering technique proposed in order to transmit larger bandwidth signals understanding also the limitations of such RoF system.
- After the important results obtained with ICON technology a possible future work can consist in designing and realizing a coupling structure to couple 850 nm VCSEL with a small patch-cord of 5 μm diameter fiber. In this way this device could be directly used with SSMF in any RoF applications.

References

- [1] M. L. M. Larry A. Coldren, Scott W. Corzine, *Diode Lasers and Photonic Integrated Circuits*, 2nd ed., K. Chang, Ed. Hoboken, New Jersey: John Wiley & Sons, April 2012.
- [2] G. L. Li and P. K. L. Yu, “Optical intensity modulators for digital and analog applications,” *IEEE/OSA Journal of Lightwave Technology*, vol. 21, no. 9, pp. 2010–2030, Sept 2003.
- [3] J. Ma, J. Yu, C. Yu, X. Xin, J. Zeng, and L. Chen, “Fiber Dispersion Influence on Transmission of the Optical Millimeter-Waves Generated Using LN-MZM Intensity Modulation,” *IEEE/OSA Journal of Lightwave Technology*, vol. 25, no. 11, pp. 3244–3256, Nov 2007.
- [4] R. F. Kalman, J. C. Fan, and L. G. Kazovsky, “Dynamic range of coherent analog fiber-optic links,” *IEEE/OSA Journal of Lightwave Technology*, vol. 12, no. 7, pp. 1263–1277, Jul 1994.
- [5] L. V.A. Thomas, M.E. Hajjar, “Performance Improvement and Cost Reduction Techniques for Radio Over Fiber Communications,” *IEEE Communications, Surveys and Tutorials*, 2015.
- [6] G. Meslener, “Chromatic dispersion induced distortion of modulated monochromatic light employing direct detection,” *IEEE Journal of Quantum Electronics*, vol. 20, pp. 1208–1216, 1984.
- [7] F. Favre and D. le Guen, “High frequency stability of laser diode for heterodyne communication systems,” *Electronics Letters*, vol. 16, no. 18, pp. 709–710, August 1980.
- [8] T. Okoshi and K. Kikuchi, “Frequency stabilisation of semiconductor lasers for heterodyne-type optical communication systems,” *Electronics Letters*, vol. 16, no. 5, pp. 179–181, February 1980.

- [9] A. Nirmalathas, P. A. Gamage, C. Lim, D. Novak, R. Waterhouse, and Y. Yang, “Digitized RF transmission over fiber,” *IEEE Microwave Magazine*, vol. 10, no. 4, pp. 75–81, June 2009.
- [10] R. G. Vaughan, N. L. Scott, and D. R. White, “The theory of bandpass sampling,” *IEEE Transactions on Signal Processing*, vol. 39, no. 9, pp. 1973–1984, Sep 1991.
- [11] C. Liu, L. Zhang, M. Zhu, J. Wang, L. Cheng, and G. K. Chang, “A Novel Multi-Service Small-Cell Cloud Radio Access Network for Mobile Backhaul and Computing Based on Radio-Over-Fiber Technologies,” *IEEE/OSA Journal of Lightwave Technology*, vol. 31, no. 17, pp. 2869–2875, Sept 2013.
- [12] I. Chih-Lin and J. Huang, “RAN revolution with NGFI (xHaul) for 5G,” in *Proceedings of Optical Fiber Communications Conference and Exhibition (OFC)*, March 2017, pp. 1–4.
- [13] Cisco, “Cisco 5G Vision Series: Small Cell Evolution,” Cisco, Tech. Rep., 2015.
- [14] T. Pfeiffer, “Next generation mobile fronthaul and midhaul architectures [Invited],” *IEEE/OSA J. Optical Commun. and Networking*, vol. 7, no. 11, pp. B38–B45, November 2015.
- [15] NOKIA, “Ultra Dense Network (UDN) White Paper,” NOKIA, Tech. Rep., 2016.
- [16] Ericsson, Ed., *Ericsson Review: Connecting the dots: small cells shape up for high-performance indoor radio*, vol. 91, December 2014.
- [17] D. Wake, A. Nkansah, and N. J. Gomes, “Radio Over Fiber Link Design for Next Generation Wireless Systems,” *IEEE/OSA Journal of Lightwave Technology*, vol. 28, no. 16, pp. 2456–2464, Aug 2010.
- [18] N. J. Gomes, P. Assimakopoulos, M. K. Al-Hares, U. Habib, and S. Noor, “The new flexible mobile fronthaul: Digital or analog, or both?” in *Proceedings of 18th International Conference on Transparent Optical Networks (ICTON)*, July 2016, pp. 1–4.
- [19] A. Pizzinat, P. Chanclou, T. Diallo, and F. Saliou, “Things you should know about fronthaul,” in *Proceedings of the European Conference on Optical Communications (ECOC)*, Sept 2014, pp. 1–3.
- [20] C. T. Tsai, C.-H. Lin, C.-T. Lin, Y.-C. Chi, and G.-R. Lin, “60-GHz Millimeter-wave Over Fiber with Directly Modulated Dual-mode Laser Diode,” *Science Reports*, vol. 9, 2016.
- [21] C. Y. Lin, Y. C. Chi, C. T. Tsai, H. Y. Wang, and G. R. Lin, “39-GHz Millimeter-Wave Carrier Generation in Dual-Mode Colorless Laser Diode for OFDM-MMWoF Transmission,” *IEEE Journal of Selected Topics in Quantum Electronics*, vol. 21, no. 6, pp. 609–618, Nov 2015.

-
- [22] P. Li, W. Pan, X. Zou, B. Lu, L. Yan, and B. Luo, "Image-Free Microwave Photonic Down-Conversion Approach for Fiber-Optic Antenna Remoting," *IEEE Journal of Quantum Electronics*, vol. 53, no. 4, pp. 1–8, Aug 2017.
- [23] Z. Tayq, L. A. Neto, F. Saliou, C. A. Berthelemot, J. Gomes, T. Hausteijn, M. Lacouche, J. Plumecoq, L. Bellot, and P. Chanclou, "Real time demonstration of fronthaul transport over a mix of analog and digital RoF," in *Proceedings of 19th International Conference on Transparent Optical Networks (ICTON)*, July 2017, pp. 1–4.
- [24] "ISO/IEC/IEEE International Standard for Information technology—Telecommunications and information exchange between systems—Local and metropolitan area networks—Specific requirements—Part 11: Wireless LAN Medium Access Control (MAC) and Physical Layer (PHY) Specifications Amendment 3: Enhancements for Very High Throughput in the 60 GHz Band (adoption of IEEE Std 802.11ad-2012)," *ISO/IEC/IEEE 8802-11:2012/Amd.3:2014(E)*, pp. 1–634, March 2014.
- [25] C. Viana, "Technological development and system integration of VCSELs and SiGe HPT receivers for 60 GHz low cost Radio-over-Fiber applications," Ph.D. dissertation, ESIEE, 2014.
- [26] F. Forni, Y. Shi, H. P. A. van den Boom, E. Tangdiongga, and A. M. J. Koonen, "Multiband LTE-A, WiFi ac, and 4-PAM baseband simultaneous transmission over 50 m thick-core POF for in-home network," in *Proceedings of 19th International Conference on Transparent Optical Networks (ICTON)*, July 2017, pp. 1–4.
- [27] A. El-Makadema, N. Razavi-Ghods, and A. Brown, "Scanning performance of SKA-low sparse array configurations incorporating realistic element patterns and sky noise contributions," in *Proceedings of IEEE International Conference on Electromagnetics in Advanced Applications (ICEEA)*, Sept 2012, pp. 844–847.
- [28] A. J. Faulkner and J. G. B. de Vaate, "SKA low frequency aperture array," in *Proceedings of IEEE International Symposium on Antennas and Propagation USNC/URSI National Radio Science Meeting*, July 2015, pp. 1368–1369.
- [29] R. Beresford, W. Cheng, and P. Roberts, "Low cost RF over fiber distribution for radio astronomy phased arrays," in *XXXII General Assembly and Scientific Symposium of the International Union of Radio Science (URSI GASS)*, Aug 2017, pp. 1–4.
- [30] B. Elliot and M. Gilmore, *Fiber Optic Cabling*, 2nd ed., Newnes, Ed. Linacre House, Jordan Hill, Oxford: Newnes, 2002.
- [31] *Recommendation ITU-T G.652*, Std., 2017. [Online]. Available: <http://www.itu.int/rec/T-REC-G.652-200911-I/en>
- [32] *Recommendation ITU-T G.651*, Std., 2008. [Online]. Available: <http://www.itu.int/rec/T-REC-G.651-200911-I/en>

- [33] Corning. (2014, November) Corning SMF-28 Ultra Optical Fiber-Product Information. [Online]. Available: <https://www.corning.com/media/worldwide/coc/documents/Fiber/SMF-28%20Ultra.pdf>
- [34] Thorlabs. (2015, November) Thorlabs SMF-28-J9 Specifications. [Online]. Available: <https://www.thorlabs.com/drawings/bac98901a5966951-CD3901DF-B6F5-A42D-B2298FA50847B554/SMF-28-J9-SpecSheet.pdf>
- [35] *Recommendation ITU-T G.657*, Std., 2017. [Online]. Available: <https://www.itu.int/rec/T-REC-G.657-201611-I/en>
- [36] D. Vez, S. G. Hunziker, R. Kohler, P. Royo, M. Moser, and W. Bachtold, “850 nm vertical-cavity laser pigtailed to standard singlemode fibre for radio over fibre transmission,” *Electronics Letters*, vol. 40, no. 19, pp. 1210–1211, Sept 2004.
- [37] Z. Tian, C. Chen, and D. V. Plant, “850-nm VCSEL Transmission Over Standard Single-Mode Fiber Using Fiber Mode Filter,” *IEEE Photonics Technology Letters*, vol. 24, no. 5, pp. 368–370, March 2012.
- [38] I. Papakonstantinou, S. Papadopoulos, C. Soos, J. Troska, F. Vasey, and P. Vichoudis, “Modal Dispersion Mitigation in Standard Single-Mode Fibers at 850 nm With Fiber Mode Filters,” *IEEE Photonics Technology Letters*, vol. 22, no. 20, pp. 1476–1478, Oct 2010.
- [39] K. M., S. G., M. L., and S. J., “Transmission in single mode telecom fiber below the cut-off wavelength,” *Microwave and Optical Technology Letters*, vol. 59, no. 8, pp. 2033–2038, 2017.
- [40] P. M. Sevila, V. Almenar, and J. L. Corral, “Transmission Over SSMF at 850 nm: Bimodal Propagation and Equalization,” *IEEE/OSA Journal of Lightwave Technology*, vol. 35, no. 19, pp. 4125–4136, Oct 2017.
- [41] SWDM Alliance. [Online]. Available: <http://www.swdm.org/>
- [42] Q. Xu, “OM5 and SWDM: Are We Ready?” Belden, Tech. Rep., 2017.
- [43] H. Soda, K. ichi Iga, C. Kitahara, and Y. Suematsu, “GaInAsP/InP Surface Emitting Injection Lasers,” *Japanese Journal of Applied Physics*, vol. 18, no. 12, p. 2329, 1979.
- [44] K. Iga, F. Koyama, and S. Kinoshita, “Surface emitting semiconductor lasers,” *IEEE Journal of Quantum Electronics*, vol. 24, no. 9, pp. 1845–1855, Sept 1988.
- [45] J. L. Jewell, A. Scherer, S. L. McCall, Y. H. Lee, S. Walker, J. P. Harbison, and L. T. Florez, “Low-threshold electrically pumped vertical-cavity surface-emitting microlasers,” *Electronics Letters*, vol. 25, no. 17, pp. 1123–1124, Aug 1989.

-
- [46] N. K. Dutta, T. Wessel, N. A. Olsson, R. A. Logan, R. Yen, and P. J. Anthony, "Fabrication and performance characteristics of InGaAsP ridge-guide distributed-feedback multiquantum-well lasers," *Electronics Letters*, vol. 21, no. 13, pp. 571–573, June 1985.
- [47] T. Tadokoro, W. Kobayashi, T. Fujisawa, T. Yamanaka, and F. Kano, "43 Gb/s 1.3 μm DFB Laser for 40 km Transmission," *IEEE/OSA Journal of Lightwave Technology*, vol. 30, no. 15, pp. 2520–2524, Aug 2012.
- [48] R. Michalzik, Ed., *VCSELs Fundamentals, Technology and Applications of Vertical-Cavity Surface-Emitting Lasers*. Springer, 2013.
- [49] J. A. Tatum, D. Gazula, L. A. Graham, J. K. Guenter, R. H. Johnson, J. King, C. Kocot, G. D. Landry, I. Lyubomirsky, A. N. MacInnes, E. M. Shaw, K. Balemarchy, R. Shubochkin, D. Vaidya, M. Yan, and F. Tang, "VCSEL-Based Interconnects for Current and Future Data Centers," *IEEE/OSA Journal of Lightwave Technology*, vol. 33, no. 4, pp. 727–732, Feb 2015.
- [50] H. Y. Kao *et al.*, "Comparison of single-/few-/multi-mode 850 nm VCSELs for optical OFDM transmission," *OSA Optics Express*, vol. 25, no. 14, pp. 16 347–16 363, Jul 2017.
- [51] C. T. Tsai *et al.*, "Multi-Mode VCSEL Chip with High-Indium-Density InGaAs/AlGaAs Quantum-Well Pairs for QAM-OFDM in Multi-Mode Fiber," *IEEE Journal of Quantum Electronics*, vol. PP, no. 99, pp. 1–1, 2017.
- [52] J.-F. Seurin, D. Zhou, G. Xu, A. Miglo, D. Li, T. Chen, B. Guo, and C. Ghosh, "High-efficiency VCSEL arrays for illumination and sensing in consumer applications," in *Proceedings of SPIE*, 2016, pp. 9766 – 9775.
- [53] P. S. S. Holenarsipur, "Proximity sensors with smudge detection capabilities," U.S. Patent no. US9 098 124B2, 2013-01-10.
- [54] A. Yariv and P. Yeh, *Photonics: Optical Electronics in Modern Communications*, 6th ed., S. Adel S. Sedra, Ed. 198 Madison Avenue, New York, New York 10016: Oxford University Press, 2006.
- [55] G. Reiner, E. Zeeb, B. Moller, M. Ries, and K. J. Ebeling, "Optimization of planar be-doped ingaas vcsel's with two-sided output," *IEEE Photonics Technology Letters*, vol. 7, no. 7, pp. 730–732, July 1995.
- [56] K. Lear, K. Choquette, R. Schneider, S. Kilcoyne, and K. Geib, "Selectively oxidised vertical cavity surface emitting lasers with 50% power conversion efficiency," *Electronics Letters*, vol. 31, no. 3, pp. 208–209, Feb 1995.
- [57] K. Choquette and H. Q. Hou, "Vertical-cavity surface emitting lasers: moving from research to manufacturing," *Proceedings of the IEEE*, vol. 85, no. 11, pp. 1730–1739, Nov 1997.

- [58] R. P. Sarzała and Ł. Piskorski, “Comparative analysis of lasing performance of oxide-confined and proton-implanted vertical-cavity surface-emitting diode lasers,” *Applied Physics A*, vol. 102, no. 2, pp. 359–366, Feb 2011.
- [59] K. Ebeling, *Semiconductor Quantum Optoelectronics: From Quantum Physics to Smart Devices*, 1st ed., M. E. A. Miller, D Finlayson, Ed. Scottish Universities Summer School in Physics and Institute of Physics Publishing, Bristol and Philadelphia, Jan 1999.
- [60] F. Kish, S. Carraci, N. H. Jr., J. Dallesasse, K. Hsieh, M. Ries, S. Smith, and R. Burnham, “Planar native oxide index guided AlGaAs-GaAs quantum well heterostructure lasers,” *Applied Physics Letters*, vol. 59, no. 14, p. 1755, 1991.
- [61] G. Hadley, “Effective index model for vertical cavity surface emitting lasers,” *Optics Letters*, vol. 20, no. 13, pp. 1483–1484, 1995.
- [62] G. P. Bava, P. Debernardi, and L. Fratta, “Three-dimensional model for vectorial fields in vertical-cavity surface-emitting lasers,” *Physical Review A*, vol. 63, p. 023816, Jan 2001.
- [63] P. Debernardi, A. Pisoni, and G. P. Bava, “Quantum-well nonlinear optical response, including valence-band mixing and coulomb effects,” *IEEE Journal of Quantum Electronics*, vol. 30, no. 1, pp. 93–107, Jan 1994.
- [64] P. Debernardi, “HOT-VELM: A Comprehensive and Efficient Code for Fully Vectorial and 3-D Hot-Cavity VCSEL Simulation,” *IEEE Journal of Quantum Electronics*, vol. 45, no. 8, pp. 979–992, Aug 2009.
- [65] S. Sze and K. K. Ng, *Physics of Semiconductor Devices*, 3rd ed. Hoboken, New Jersey: John Wiley & Sons, 2007.
- [66] N. B. Lukyanchikova, N. P. Garbar, M. V. Petrichuk, A. A. Rezazadeh, and S. A. Bashar, “Noise properties of AlGaAs/GaAs HPTs with transparent ITO emitter contacts,” in *Proceedings of High Performance Electron Devices for Microwave and Optoelectronic (EDMO) Applications Workshop*, Nov 1996, pp. 50–55.
- [67] H. R. Chen, S. W. Tan, W. T. Chen, T. S. Lin, and S. Lour, “The Effect on Base Bias for InGaP/GaAs Heterojunction Phototransistors,” in *Proceedings of Conference on Optoelectronic and Microelectronic Materials and Devices (COMMAD)*, Dec 2004, pp. 241–244.
- [68] Z. Pei, C. S. Liang, L. S. Lai, Y. T. Tseng, Y. M. Hsu, P. S. Chen, S. C. Lu, M. J. Tsai, and C. W. Liu, “A high-performance SiGe-Si multiple-quantum-well heterojunction phototransistor,” *IEEE Electron Device Letters*, vol. 24, no. 10, pp. 643–645, Oct 2003.
- [69] Y. Zhu, Q. Yang, and Q. Wang, “Resonant cavity SiGe/Si MQW heterojunction phototransistor grown on the SIMOX substrate for 1.3 μm operation,” in *Proceedings of 47th Electronic Components and Technology Conference*, May 1997, pp. 1199–1204.

-
- [70] J. Schiellein, M. Rosales, J. L. Polleux, C. Algani, T. Merlet, M. Riet, J. Godin, and A. Scavenec, "Analysis of opto-microwave paths into a InP/InGaAs UTC-HPT," in *Proceedings of 41st European Microwave Conference*, Oct 2011, pp. 949–952.
- [71] J. L. Polleux, F. Moutier, A. L. Billabert, C. Rumelhard, E. Sönmez, and H. Schumacher, "A strained SiGe layer heterojunction bipolar phototransistor for short-range opto-microwave applications," in *Proceedings of International Topical Meeting on Microwave Photonics (MWP)*, Sept 2003, pp. 113–116.
- [72] J. L. Polleux, F. Moutierand, A. L. Billabert, C. Rumelhard, E. Sönmez, and H. Schumacher, "An SiGe/Si heterojunction phototransistor for opto-microwave applications: modeling and first experimental results," in *Proceedings of Gallium Arsenide Applications Symposium (GAAS)*, Munich, Oct 2003, pp. 231–234.
- [73] Z. Pei, J. W. Shi, Y. M. Hsu, F. Yuan, C. S. Liang, S. C. Lu, W. Y. Hsieh, M. J. Tsai, and C. W. Liu, "Bandwidth enhancement in an integratable SiGe phototransistor by removal of excess carriers," *IEEE Electron Device Letters*, vol. 25, no. 5, pp. 286–288, May 2004.
- [74] T. Yin, A. M. Pappu, and A. B. Apsel, "Low-cost, high-efficiency, and high-speed SiGe phototransistors in commercial BiCMOS," *IEEE Photonics Technology Letters*, vol. 18, no. 1, pp. 55–57, Jan 2006.
- [75] M. Egels, B. Delacressonnière, Y. Sahabun, and P. Lecoy, "Design of an optically frequency or phase-controlled oscillator for hybrid fiber-radio LAN at 5.2 GHz," *Microw. Optical Technol. Lett.*, vol. 45, no. 2, pp. 104–107, 2005.
- [76] Z. G. Tegegne, "SiGe/Si Microwave Photonic Phototransistors and Interconnects toward Silicon-based full Optical Links," Ph.D. dissertation, Université Paris-Est, ESYCOM, ESIEE Paris, UPEM, Le Cnam, June 2016.
- [77] Z. G. Tegegne, C. Viana, J. L. Polleux, M. Grzeskowiak, and E. Richalot, "Study of Lateral Scaling Impact on the Frequency Performance of SiGe Heterojunction Bipolar Phototransistor," *IEEE Journal of Quantum Electronics*, vol. 54, no. 3, pp. 1–9, June 2018.
- [78] C. Viana, Z. G. Tegegne, M. Rosales, J. L. Polleux, C. Algani, V. Lecocq, C. Lyszyk, and S. Denet, "Hybrid photo-receiver based on SiGe heterojunction photo-transistor for low-cost 60 GHz intermediate-frequency radio-over-fibre applications," *Electronics Letters*, vol. 51, no. 8, pp. 640–642, 2015.
- [79] G. Liu, A. Trasser, and H. Schumacher, "33 - 43 GHz and 66 - 86 GHz VCO With High Output Power in an 80 GHz SiGe HBT Technology," *IEEE Microwave Wireless Components Letters*, vol. 20, no. 10, pp. 557–559, Oct 2010.

- [80] M. D. Rosales, J. Schiellein, C. Viana, J. L. Polleux, and C. Algani, "Full area emitter SiGe phototransistor for opto-microwave circuit applications," in *Proceedings of 9th International Conference Group IV Photonics (GFP)*, Aug 2012, pp. 294–296.
- [81] M. D. Rosales, "Study of SiGe HPT for radio-over-fiber applications," Ph.D. dissertation, Université Paris-Est, ESYCOM, ESIEE Paris, UPEM, Le Cnam,, June 2014.
- [82] R. Dandliker, A. Bertholds, and F. Maystre, "How modal noise in multimode fibers depends on source spectrum and fiber dispersion," *IEEE/OSA Journal of Lightwave Technology*, vol. 3, no. 1, pp. 7–12, Feb 1985.
- [83] K. Petermann, *Laser Diode Modulation and Noise*, T. Okoshi, Ed. Kluwer Academy Publishers, 1991.
- [84] C. Henry, "Theory of the linewidth of semiconductor lasers," *IEEE Journal of Quantum Electronics*, vol. 18, no. 2, pp. 259–264, February 1982.
- [85] T. L. Koch and J. E. Bowers, "Factors affecting wavelength chirping in directly modulated semiconductor lasers," in *Proceedings of OSA Conference on Lasers and Electro-Optics (CLEO)*. Optical Society of America, 1985, p. WB2.
- [86] A. Villafranca, J. Lasobras, and I. Garces, "Precise characterization of the frequency chirp in directly modulated DFB lasers," in *Proceedings of Spanish Conference on Electronic Devices*, Jan 2007, pp. 173–176.
- [87] C. Harder, K. Vahala, and A. Yariv, "Measurement of the linewidth enhancement factor alpha of semiconductor lasers," *Applied Physics Letters*, no. 4, pp. 328–330, 1983.
- [88] K. Kojucharow, M. Sauer, and C. Schaffer, "Millimeter-wave signal properties resulting from electrooptical upconversion," *IEEE Transactions on Microwave Theory and Techniques*, vol. 49, no. 10, pp. 1977–1985, Oct 2001.
- [89] B. Carlson, *Communication Systems*, 5th ed., M.-H. Education, Ed. McGraw-Hill Education, Feb 2009.
- [90] G. P. Agrawal and N. K. Dutta, *Semiconductor Lasers*, S. V. US, Ed. Springer US, 1993.
- [91] D. T. Wellinger, "Modal noise in singlemode and multimode fiber links," *White Paper*, 2012.
- [92] K. H. Hahn, M. R. Tan, Y. M. Houg, and S. Y. Wang, "Large area multitransverse-mode VCSELs for modal noise reduction in multimode fibre systems," *Electronics Letters*, vol. 29, no. 16, pp. 1482–1483, Aug 1993.
- [93] P. Coe, *An Investigation of Mode Partitioning in VCSELs*, HP Laboratories, Bristol, UK, 1996.

-
- [94] D. Visani, “Fiber-Optic Technologies for Wireline and Wireless In-building Networks,” Ph.D. dissertation, Università di Bologna, 2012.
- [95] P. Pepeljugoski, S. E. Golowich, A. J. Ritger, P. Kolesar, and A. Risteski, “Modeling and simulation of next-generation multimode fiber links,” *IEEE/OSA Journal of Lightwave Technology*, vol. 21, no. 5, pp. 1242–1255, May 2003.
- [96] M. Abramowitz, *Handbook of Mathematical Functions, With Formulas, Graphs, and Mathematical Tables*. New York, NY, USA: Dover Publications, Inc., 1974.
- [97] D. Visani, G. Tartarini, M. N. Petersen, L. Tarlazzi, and P. Faccin, “Link Design Rules for Cost-Effective Short-Range Radio Over Multimode Fiber Systems,” *IEEE Transactions on Microwave Theory and Techniques*, vol. 58, no. 11, pp. 3144–3153, Nov 2010.
- [98] A. Koonen, “Bit-Error-Rate Degradation in a Multimode Fiber Optic Transmission Link Due to Modal Noise,” *IEEE Journal of Selected Areas in Communications*, vol. 4, no. 9, pp. 1515–1522, Dec 1986.
- [99] I. Charles H. Cox, *Analog Optical Links: Theory and Practice*, 1st ed. Cambridge University Press, 2004.
- [100] NRAO, *Very Long Baseline Array Project Book*. VLBA Project Office, 1988.
- [101] T. Zhang, N. H. Zhu, B. H. Zhang, and X. Zhang, “Measurement of Chirp Parameter and Modulation Index of a Semiconductor Laser Based on Optical Spectrum Analysis,” *IEEE Photonics Technology Letters*, vol. 19, no. 4, pp. 227–229, Feb 2007.
- [102] H. Kogelnik and P. J. Winzer, “Modal birefringence in weakly guiding fibers,” *IEEE/OSA Journal of Lightwave Technology*, vol. 30, no. 14, pp. 2240–2245, July 2012.
- [103] U. Kruger and K. Kruger, “Simultaneous measurement of the linewidth, linewidth enhancement factor α , and FM and AM response of a semiconductor laser,” *IEEE/OSA Journal of Lightwave Technology*, vol. 13, no. 4, pp. 592–597, Apr 1995.
- [104] L. Olofsson and T. G. Brown, “Frequency dependence of the chirp factor in 1.55 μm distributed feedback semiconductor lasers,” *IEEE Photonics Technology Letters*, vol. 4, no. 7, pp. 688–691, July 1992.
- [105] J.-M. Savolainen, L. Grüner-Nielsen, P. Kristensen, and P. Balling, “Measurement of effective refractive-index differences in a few-mode fiber by axial fiber stretching,” *OSA Optics Express*, vol. 20, no. 17, pp. 18 646–18 651, Aug 2012.
- [106] L. Hoffmann, M. S. Müller, S. Krämer, M. Giebel, G. Schwotzer, and T. Wieduwilt, “Applications of fibre optic temperature measurement,” in *Proceedings of the Estonian Academy of Sciences: Engineering*, 2007, pp. 363–378.
- [107] W. Zhi-Yong, Q. Qi, and S. Shuang-Jin, “Temperature dependence of the refractive index of optical fibers,” *Chinese Physics B*, vol. 23, no. 3, p. 034201, 2014.

- [108] P. Krehlik, "Characterization of semiconductor laser frequency chirp based on signal distortion in dispersive optical fiber," *Opto-Electronics Review*, vol. 14, no. 2, pp. 119–124, June 2006.
- [109] C. D. Poole and T. E. Darcie, "Distortion related to polarization-mode dispersion in analog lightwave systems," *IEEE/OSA Journal of Lightwave Technology*, vol. 11, no. 11, pp. 1749–1759, Nov 1993.
- [110] C. S. Ih and W. Gu, "Fiber Induced Distortions in a Subcarrier Multiplexed Lightwave System," *IEEE Journal on Selected Areas in Communications*, vol. 8, pp. 1296–1303, 1990.
- [111] S. Betti, E. Bravi, and M. Giaconi, "Nonlinear distortions due to the "dispersive" transmission of SCM optical signals in the presence of chirping effect: an accurate analysis," *IEEE Photonics Technology Letters*, vol. 9, no. 12, pp. 1640–1642, Dec 1997.
- [112] M. Bousonville and J. Rausch, "Velocity of signal delay changes in fibre optic cable," in *Proceedings of European Workshop on Beam Diagnostics and Instrumentation for Particle Accelerators (DIPAC)*, Basel, Switzerland, May 2009, pp. 248–250.
- [113] I. Kaminow, "Polarization in optical fibers," *IEEE Journal of Quantum Electronics*, vol. 17, no. 1, pp. 15–22, Jan 1981.
- [114] K. Borzycki and M. Jaworski, "Temperature Dependence of PMD in Optical Fibres and Cables: Part II," in *Proceedings of International Conference on Transparent Optical Networks (ICTON)*, June 2006, pp. 209–212.
- [115] *LTE Evolved Universal Terrestrial Radio Access (E-UTRA)*, 3rd Generation Partnership Project (3GPP) Std., Rev. 13.
- [116] F. Pizzuti, "Sviluppo di un software per la caratterizzazione di un collegamento lte radio over fiber e realizzazione del relativo banco di misura," Master Thesis, Università di Bologna, 2016.
- [117] U. Rehfuess, "5G for people and things, 700 MHz band as key to success for wide area 5G services," NOKIA, Tech. Rep., 2017.
- [118] T. S. G. R. A. Network, *NR - Base Station (BS) radio transmission and reception*, 3rd Generation Partnership Project (3GPP) Std. 15.2, June 2018.
- [119] *LTE Evolved Universal Terrestrial Radio Access (E-UTRA); Base Station (BS) radio transmission and reception*, 3rd Generation Partnership Project (3GPP) Std., Rev. 11.
- [120] C. Viana, Z. G. Tegegne, J. Polleux, and C. Algani, "Flexible New Opto-Microwave Design Approach for Radio-Over-Fiber Applications: A Case Study of Low-Cost 60-GHz VCSEL-Based IF-RoF Link," *IEEE Transactions on Microwave Theory and Techniques*, vol. 66, no. 9, pp. 4293–4305, Sept 2018.

-
- [121] G. Niu, "Noise in SiGe HBT RF Technology: Physics, Modeling, and Circuit Implications," *Proceedings of the IEEE*, vol. 93, no. 9, pp. 1583–1597, Sept 2005.
- [122] J. K. Twynam and R. C. Woods, "Current crowding effects in GaAs/AlGaAs heterojunction phototransistors," *IEE Proceedings J - Optoelectronics*, vol. 135, no. 1, pp. 52–55, February 1988.
- [123] T. Tekin, "Review of Packaging of Optoelectronic, Photonic, and MEMS Components," *IEEE Journal of Selected Topics in Quantum Electronics*, vol. 17, no. 3, pp. 704–719, May 2011.
- [124] V. Bardinal, T. Camps, B. Reig, D. Barat, E. Daran, and J. B. Doucet, "Collective Micro-Optics Technologies for VCSEL Photonic Integration," *Advances in Optical Technologies*, vol. 2011, pp. 1–11, 2011.
- [125] A. Hashim, N. Bamiedakis, Y. Hao, R. V. Penty, and I. H. White, "Design of a low-cost 10 Gb/s chip-to-chip optical interconnect," in *Proceedings of International Conference On Photonics*, July 2010, pp. 1–4.
- [126] L. Brusberg, N. Schleppe, and H. Schröder, "Chip-to-chip communication by optical routing inside a thin glass substrate," in *Proceedings of IEEE 61st Electronic Components and Technology Conference (ECTC)*, May 2011, pp. 805–812.
- [127] I.-S. Chung, P. Debernardi, Y. T. Lee, and J. Mørk, "Transverse-mode-selectable microlens vertical-cavity surface-emitting laser," *OSA Optics Express*, vol. 18, no. 5, pp. 4138–4147, Mar 2010.
- [128] A. K. Nallani, T. Chen, D. J. Hayes, W.-S. Che, and J.-B. Lee, "A method for improved VCSEL packaging using MEMS and ink-jet technologies," *IEEE/OSA Journal of Lightwave Technology*, vol. 24, no. 3, pp. 1504–1512, March 2006.
- [129] B. Ciftcioglu, R. Berman, J. Zhang, Z. Darling, S. Wang, J. Hu, J. Xue, A. Garg, M. Jain, I. Savidis, D. Moore, M. Huang, E. G. Friedman, G. Wicks, and H. Wu, "A 3-D Integrated Intrachip Free-Space Optical Interconnect for Many-Core Chips," *IEEE Photonics Technology Letters*, vol. 23, no. 3, pp. 164–166, Feb 2011.
- [130] G. Li, Y. Hashimoto, S. Ebuchi, T. Maruyama, and K. Iiyama, "High-efficiency optical coupling to planar photodiode using metal reflector loaded Waveguide grating coupler," in *Proceedings of 12th International Conference on Numerical Simulation of Optoelectronic Devices (NUSOD)*, Aug 2012, pp. 15–16.
- [131] D. J. Hayes and T. Chen, "Next-generation optoelectronic components enabled by direct-write microprinting technology," in *Proceedings SPIE*, vol. 5435, 2004, pp. 1–8.
- [132] A. L. Glebov, D. Bhusari, P. Kohl, M. S. Bakir, J. D. Meindl, and M. G. Lee, "Flexible pillars for displacement compensation in optical chip assembly," *IEEE Photonics Technology Letters*, vol. 18, no. 8, pp. 974–976, April 2006.

- [133] M. S. Bakir, T. K. Gaylord, O. O. Ogunsola, E. N. Glytsis, and J. D. Meindl, “Optical transmission of polymer pillars for chip I/O optical interconnections,” *IEEE Photonics Technology Letters*, vol. 16, no. 1, pp. 117–119, Jan 2004.
- [134] J.-L. Polleux and C. Viana, “Structure de couplage optique collective passive de composants optiques et opto-électroniques,” French Patent no.1 000 226 986, 2014.
- [135] SU-8 2000 Permanent Epoxy Negative Photoresist. Microchem Corporation.

List of publications

Journal Papers

- P1. J. Nanni S. Rusticelli, F. Perini, J. L. Polleux, , C. Algani, G. Tartarini, “Chirp evaluation of 850 nm single mode VCSEL exploiting modal noise in standard single mode fiber,” *IEEE Journal of Quantum Electronics*, vol. 54, no. 4, pp. 1-11, Aug. 2018.
- P2. J. Nanni S. Rusticelli, F. Perini, J. L. Polleux, , C. Algani, G. Tartarini, “VCSEL-based Radio-over-G652 Fiber System for short/medium range MFH solutions,” *IEEE/OSA Journal of Lightwave Technology*, vol. 36, no. 19, pp. 4430-4437, Oct. 1, 2018.
- P3. J. Nanni, M. Barbiroli, F. Fuschini, D. Masotti, J. L. Polleux, C. Algani, and G. Tartarini, “Chirp evaluation of semiconductor DFB lasers through a simple Interferometry-Based (IB) technique,” *OSA Applied Optics*, vol. 55, no. 28, pp. 7788–7795, Oct. 2016.
- P4. J. Nanni, S. Rusticelli, C. Viana, J. L. Polleux, C. Algani, F. Perini and G. Tartarini, “Modal Noise Mitigation in 850-nm VCSEL-Based Transmission Systems Over Single-Mode Fiber,” *IEEE Transactions on Microwave Theory and Techniques*, vol. 64, no. 10, pp. 3342–3350, Oct. 2016.
- P5. C. Viana, Z. G. Tegegne, J. Nanni, G. Tartarini, C. Algani, F. Marty and N. Pavy and J. L. Polleux, “Vertical Optical Coupling Structure Based on Polymer for Small Size and High-Speed Photodetectors,” *IEEE Photonics Technology Letters*, vol. 30, no. 21, pp. 1886–1889, Nov. 2018.

International Conferences

- P6. J. Nanni, Z. Tegegne, G. Tartarini, C. Algani and J. L. Polleux, “Use of SiGe Photo-Transistor in RoF links based on VCSEL and standard single mode fiber for low cost LTE applications,” *IEEE International Topical Meeting on Microwave Photonics (MWP) 2018*, Toulouse, France, 22–25 Oct. 2018.
- P7. J. Nanni, F. Pizzuti, J. L. Polleux, C. Algani and G. Tartarini, “VCSEL-SSMF-based Radio-over-Fiber link for low cost and low consumption Wireless Dense Networks,” *IEEE*

International Topical Meeting on Microwave Photonics (MWP) 2017, Beijing, China, 23–26 Oct. 2017.

- P8. M. U. Hadi, J. Nanni, P. A. Traverso, G. Tartarini, O. Venard, G. Baudoin and J. L. Polleux, “Experimental evaluation of digital predistortion for VCSEL-SSMF-based Radio-over-Fiber link,” *IEEE International Topical Meeting on Microwave Photonics (MWP) 2018*, Toulouse, France, 22–25 Oct. 2018.
- P9. F. Fuochi, M. U. Hadi, J. Nanni, P. A. Traverso and G. Tartarini, “Digital predistortion technique for the compensation of nonlinear effects in radio over fiber links,” *IEEE 2nd International Forum on Research and Technologies for Society and Industry Leveraging a better tomorrow (RTSI) 2016*, Bologna, Italy, 7–9 Sep. 2016.

National Conferences

- P10. J. Nanni, G. Tartarini, S. Rusticelli, F. Perini, J. L. Polleux, C. Algani, “Modal noise in 850nm VCSEL-based radio over fiber systems for manifold applications,” *Fotonica AEIT Italian Conference on Photonics Technologies 2015*, Turin, Italy, 6–8 May. 2015.
- P11. F. Fuochi, M. U. Hadi, J. Nanni, P. A. Traverso and G. Tartarini, “Digital predistortion technique for the compensation of nonlinear effects in radio over fiber links,” *XXI RiNEm Riunione Nazionale di Elettromagnetismo 2016*, Bologna, Italy, 12–14 Sep. 2016.